Aspects of cosmological first order phase transitions : propagation of ultra-relativistic shells, heavy dark matter, and baryogenesis

Maximilian Dichtl

To cite this version:

Maximilian Dichtl. Aspects of cosmological first order phase transitions : propagation of ultra-relativistic shells, heavy dark matter, and baryogenesis. Astrophysics [astro-ph]. Sorbonne Université, 2024. English. NNT : 2024SORUS181 . tel-04755713

HAL Id: tel-04755713
https://theses.hal.science/tel-04755713v1
Submitted on 28 Oct 2024

THÈSE DE DOCTORAT
DE L'UNIVERSITÉ PIERRE ET MARIE CURIE

Spécialité : Physique
École doctorale n°564: Physique en Île-de-France

réalisée
au Laboratoire de Physique Théorique et Hautes Energies

sous la direction de

Supervisor: Dr. Filippo SALA
Co-Supervisor: Dr. Marco CIRELLI

présentée par Maximilian DICHTL

pour obtenir le grade de :
DOCTEUR DE L'UNIVERSITÉ PIERRE ET MARIE CURIE

Sujet de la thèse :

Aspects of cosmological first order phase transitions: propagation of ultra-relativistic shells, heavy dark matter, and baryogenesis

soutenue le 26 juin 2024

devant le jury composé de :

M$^{\text{me}}$	Sacha DAVIDSON	Présidente du jury
M.	Aleksandr AZATOV	Rapporteur
M$^{\text{me}}$	Djuna Lize CROON	Rapporteuse
M$^{\text{me}}$	Julia HARZ	Examinatrice
M.	Sébastien RENAUX-PETEL	Examinateur

Abstract

First order phase transitions (PT) in the early universe happen via the nucleation of bubbles whose walls can expand at ultra-relativistic velocities. Interactions of the thermal bath at the wall produce particles which accumulate in shells at the wall. The shells evolve until they collide with those from neighboring bubbles.

In this thesis we first study the evolution of these shells, including for the first time number changing interactions of the shell within itself and with the thermal bath. In particular, we calculate the rates of the dominant $3 \to 2$ scattering processes, and find they can be more important than all other processes considered in previous literature. We identify the regions of parameter space of the PT where the shells free stream, i.e. they have negligible interactions within themselves and with the bath.

We then use these results to predict the rate and energy with which particles of opposite bubbles collide. We find that these particle collisions can reach scattering energies much larger than the scale of the PT, which in turn can be used to produce highly energetic particles or particles much heavier than the scale of the PT, realising a cosmological 'bubbletron'. As an example, we show that one can produce heavy dark matter with masses above 10^3 TeV for scales of the PT of around 10 MeV, and with masses above the GUT scale for scales of the PT above about 10^9 GeV.

PTs with ultra-relativistic walls are also relevant for any other process relying on out-of-equilibrium particle production. If the interaction between particles in the shell also violates Baryon number, C, and CP, then all three Sakharov conditions are satisifed, and one can use these PTs to explain the baryon asymmetry of the universe. We do so by proposing a mechanism of baryogenesis from supercooled confining PTs.

We also compute the gravitational wave signature due to the PT in all the above scenarios. We find they could be seen by pulsar timing arrays and gravitational wave interferometers like LISA and the Einstein Telescope, realizing a new link between these telescopes and the possible origin of dark matter and of the baryon asymmetry of the universe.

Abstract long français

Le modèle standard (SM) de la physique des particules a été proposé il y a une cinquantaine d'années et a été testé avec une précision remarquable et toujours plus grande.

Bien qu'elle explique certaines parties de la nature avec une précision étonnante, elle n'est absolument pas complète. D'un point de vue expérimental, il lui manque une explication des masses des neutrinos, observées via les oscillations des neutrinos [1, 2]. Il n'est pas non plus en mesure d'expliquer les observations astrophysiques à de nombreuses échelles, des courbes de rotation des galaxies [3] au bullet cluster [4] en passant par le fond diffus cosmologique (CMB) [5], qui peut être expliqué de la manière la plus naturelle en étendant le modèle standard par un candidat à la matière noire (DM), voir p. ex. [6]. En outre, il ne fournit aucun mécanisme capable d'expliquer l'asymétrie observée dans l'abondance de la matière et de l'antimatière dans l'univers [7]. D'un point de vue théorique, il manque une complétion UV pour la gravité à l'échelle de Planck, $\sim 10^{19}$ GeV [8]. On peut également considérer comme insatisfaisant le fait que 19 constantes arbitraires et sans rapport soient nécessaires pour décrire le modèle standard. Une solution partielle à ce problème est apportée par les théories à grande unité (GUT), qui fournissent une description unifiée des interactions de jauge survenant autour de $\sim 10^{15}$ GeV [9].

Les deux mystères probablement les plus importants de la physique des (astro)particules et de la cosmologie, sur lesquels nous allons également nous concentrer dans cette thèse, sont la nature de la matière noire et l'origine de l'asymétrie des baryons de l'univers (BAU). Lorsque le problème de la matière noire a été établi, les physiciens ont proposé comme solution la plus naturelle les WIMP en tant que particules de matière noire. Cependant, les expériences de détection de direction n'ayant pas (encore) fait de découverte et le Grand collisionneur de hadrons n'ayant pas trouvé de nouvelle physique proche de l'échelle électrofaible (EW), il y a suffisamment de motivation pour s'éloigner des scénarios les plus simples de la matière noire. Il s'agit notamment de construire des mécanismes de production plus exotiques qui peuvent être testés par d'autres observables dans le cadre de nouvelles expériences, et de produire de la matière noire (DM) à différentes échelles. Nous sommes particulièrement intéressés par la production de matière noire plus lourde, potentiellement jusqu'à l'échelle du GUT, ce qui constitue une autre motivation théorique.

Les transitions de phase du premier ordre (FOPT) dans l'univers primitif sont prédites par de nombreuses théories au-delà du modèle standard, elles peuvent être utilisées pour générer de la DM et, étant donné qu'il s'agit d'un processus hors équilibre, elles peuvent servir de cadre aux mécanismes de baryogénèse. Ils ont suscité beaucoup d'intérêt ces dernières années car ils peuvent générer des ondes gravitationnelles (GWs) observables par les expériences prévues et, de manière optimiste, potentiellement déjà observées en juin 2023 par les réseaux de synchronisation de pulsars (PTAs) [10–12]. Dans cette thèse, nous avons construit de nouveaux modèles reliant les PTAs à la DM et à la BAU. Ces modèles permettent de tester expérimentalement ces mystères d'une nouvelle manière, et de les relier aux données récentes et prévues sur l'effet de serre.

Le mécanisme de production de DM lourd, que nous proposons dans cette thèse, repose sur des transitions de phase cosmologiques du premier ordre avec des parois de bulles ultra-relativistes, et a des applications potentielles au-delà du DM lourd. Un élément nécessaire au développement de ce mécanisme est le calcul de l'évolution des coquilles de particules aux parois de bulles rapides, qui est un autre contenu original présenté dans cette thèse, et dont l'intérêt va au-delà de ce mécanisme. Dans cette thèse, nous présentons la première étude systématique des interactions des coquilles de particules aux parois des FOPTs, déterminant les régions où elles flottent, et ouvrant la voie à de futures études de leur évolution qui auront des implications allant de la production de particules à la prédiction des GWs.

Enfin, les transitions de phase du premier ordre sont un ingrédient possible pour construire des modèles qui expliquent l'asymétrie matière/antimatière de l'univers. Dans ce contexte, la communauté s'est jusqu'à présent principalement concentrée sur la PT EW et sur le régime des parois lentes. Dans cette thèse, nous présentons de nouveaux résultats qui permettent de produire l'asymétrie des baryons dans les PT avec des parois de bulles ultra-relativistes, pour des échelles de PT qui peuvent être aussi basses que celle de l'EW.

Dans le chapitre I, nous donnons un aperçu général des transitions de phase du premier ordre (FOPT), dans le but d'établir le cadre et de fixer les notations. Nous commençons par étudier un modèle-jouet (dilaton) qui peut donner lieu à une PT. En effet, dans le modèle standard, la PT de l'EW n'est pas une transition de phase du premier ordre, mais un croisement [13], et donc un modèle inadapté à notre scénario souhaité. Nous généralisons ensuite à partir d'un modèle spécifique vers une description générale des FOPTs, et introduisons les paramètres pertinents pour une description phénoménologique. Cela inclut les ingrédients nécessaires à la description du signal GW associé aux FOPTs.

Nous avons décrit comment les bulles, des régions où l'univers a creusé un tunnel jusqu'au vide véritable, se forment. Le rayon de la bulle augmente alors sous l'effet de la pression, et le mur, la limite de la bulle, se dilate à des vitesses ultra-relativistes. L'expansion s'accélère avec l'augmentation de la taille de la bulle, mais peut être stoppée par la pression exercée par les particules interagissant au niveau de la paroi. Néanmoins, la vitesse terminale peut devenir très importante, comme le montre l'équation (I.26). Les particules du bain interagissant avec la paroi sont destinées à s'accumuler dans une région mince et dense à la paroi, la coquille. Nous avons considéré plusieurs modèles, qui donnent tous lieu à des coquilles, mais dont l'épaisseur, l'énergie moyenne et la multiplicité varient. Ils varient également selon que les particules s'accumulent devant la paroi (à l'extérieur de la bulle dans la phase symétrique) ou derrière la paroi (à l'intérieur de la bulle dans la phase brisée). Nous avons listé les propriétés des différents modèles dans le Tab. I.1. A la fin de ce chapitre, nous avons conclu avec le calcul du signal GW, détectable par les télescopes GW et les PTAs. Nous expliquons en détail comment une transition de phase du premier ordre donne lieu à une signature d'ondes gravitationnelles, qui devrait être observée par exemple au LISA, au télescope d'Einstein et dans les réseaux de synchronisation des pulsars.

Dans le chapitre II, basé sur [14], nous avons entrepris la première catégorisation générale de toutes les interactions auxquelles nous avons pensé et qui pourraient éventuellement modifier l'évolution de ces particules depuis leur point d'interaction avec la paroi jusqu'à la collision avec les particules des bulles voisines. Ces effets comprennent à la fois les particules de la coquille et celles du bain qui peuvent changer de momentum lors de la collision avec la paroi ultra-relativiste, les effets de dissipation des particules de la coquille, le renforcement de Bose ou les effets de la rupture de la perturbativité conduisant à de grandes fonctions de distribution de l'espace de phase, et les interactions de changement de nombre des particules de la coquille avec elles-mêmes et avec le bain thermique. Nous avons calculé leur taille et avons ainsi pu déterminer la région de l'espace des paramètres, dépendant du modèle, pour laquelle on peut négliger ces effets en toute sécurité et où les coques de particules s'écoulent librement.

Notons que pour calculer ces effets, nous avons effectué le premier calcul connu d'amplitudes de diffusion intégrées pour les processus $3 \to 2$, dont nous avons présenté les résultats dans des tableaux II.2,II.3,II.4,II.5. Nous montrons les régions d'écoulement libre dans les figures II.2,II.3,II.4,II.5,II.6. Nous constatons que tous ces effets deviennent importants pour des valeurs plus petites de l'échelle du PT, à moins que l'on ne passe à des valeurs plus petites du couplage de jauge g. Nous constatons également que les théories non-abéliennes donnent lieu à des interactions effectives dans de plus grandes régions de l'espace des paramètres, manifestement en raison de la possibilité d'une auto-interaction supplémentaire entre les bosons de jauge.

L'étude quantitative de tous ces effets nous permet d'identifier les régions de l'espace des paramètres, de n'importe quelle théorie, où les enveloppes de particules sont ou ne sont pas libres.

Dans le chapitre III, basé sur [15], nous avons proposé un nouveau mécanisme pour réaliser des collisions de particules à ultra-haute énergie dans l'univers primitif, qui repose sur la collision de coquilles créées au cours d'un FOPT cosmologique. Comme ces bulles se dilatent avec des parois ultra-relativistes, les collisions entre différentes bulles se produisent avec de grandes énergies de diffusion qui peuvent être utilisées non seulement pour générer de la matière noire mais aussi n'importe quel nouvel état lourd. Nous avons baptisé ce nouveau mécanisme le bubbletron. Pour ce faire, nous pourrions utiliser notre nouvelle capacité à retracer l'évolution des particules jusqu'à la collision afin de prédire correctement tout processus dû à la diffusion de particules entre particules voisines. Nous y parvenons en évitant en toute sécurité toute région de l'espace des paramètres où les effets du free-streaming peuvent devenir importants.

Nous avons étudié plusieurs scénarios et calculé les paramètres clés pour calculer le rendement et l'énergie des particules produites par le mécanisme du bubbletron. La formule générale pour le rendement d'un bubbletron est donnée dans l'Eq. (III.8). Nous avons ensuite donné une réalisation pratique d'un bubbletron en identifiant l'état lourd avec un candidat DM et en calculant la masse maximale possible du DM. Nous montrons nos résultats dans la Fig. III.4, où nous avons considéré des coques produites par des bosons de jauge U(1). Nous avons utilisé une théorie abélienne parce qu'elle nous permet de supposer le free-streaming pour un espace de paramètres plus grand, et donc d'étendre la région autorisée à des valeurs plus faibles de l'échelle de la PT. Nous constatons que l'on peut produire du DM lourd avec des masses supérieures à 10^3 TeV pour des échelles du PT d'environ 10 MeV, et avec des masses supérieures à l'échelle du GUT pour des échelles du PT supérieures à environ 10^9 GeV. Ce mécanisme de création de matière noire lourde au-dessus de l'échelle TeV est particulièrement motivé parce qu'il échappe à la limite d'unitarité sur la matière noire produite thermiquement [16].

Comme on peut le voir sur la Fig. III.5, les FOPTs de ces échelles se situent dans le domaine d'observation des futurs télescopes à effet de serre comme LISA et ET. De manière intrigante, ceci pourrait relier le signal GW récemment observé aux PTAs avec le DM jusqu'à l'échelle du PeV.

Plus généralement, notre étude établit un nouveau lien entre les signaux GW primordiaux et la physique à des échelles d'énergie autrement inaccessibles, non seulement en laboratoire mais aussi, jusqu'à présent, dans l'univers primitif. Dans l'exemple du DM lourd, ces GW pourraient être accompagnés de rayons cosmiques de haute énergie provenant de la désintégration du DM, s'il est instable.

Dans le chapitre IV, basé sur [17], nous avons utilisé un PT de confinement surfondu pour créer les scalaires lourds d'un secteur de confinement, qui, en raison de leurs interactions violant C, CP et B, peuvent être utilisés pour réaliser la baryogénèse. Cela est possible parce que la PT permet la production hors équilibre de particules. Nous avons constaté que, par rapport aux scénarios analogues examinés dans la littérature précédente, la nature confinante de la PT ouvre l'espace des paramètres autorisés jusqu'aux échelles EW. Cet espace est de plusieurs ordres de grandeur plus petit que dans les modèles analogues précédents qui s'appuyaient plutôt sur des PT faiblement couplés. On pourrait donc essayer de relier notre modèle de baryogénèse à la brisure de symétrie EW. Cela ouvre de nouvelles voies intéressantes pour tester notre modèle avec des expériences à l'échelle de l'EW, conduisant à des contraintes non-astrophiques, ainsi qu'à des signaux GW à LISA. Nous avons évalué les limites de plusieurs observables, y compris les recherches dans les collisionneurs, le moment dipolaire électrique du neutron et les processus de violation de saveur. Nous montrons la région permettant la baryogénèse dans la Fig. IV.2. Encore une fois, comme on peut le voir sur la Fig. IV.3, nous constatons qu'en raison de la faible valeur de l'échelle du PT, ce signal pourrait être observé par LISA et le télescope d'Einstein à l'avenir.

Nous en venons enfin aux orientations futures possibles. Dans cette thèse, nous avons jeté les bases de la catégorisation et du calcul des effets d'écoulement libre affectant l'évolution des particules depuis leur point d'interaction avec la paroi jusqu'à la collision avec des particules provenant d'autres bulles. Ceci n'est pas seulement intéressant et pertinent pour le bubbletron décrit, mais aussi pour le calcul correct du signal GW, puisque l'amplitude des GW pourrait aussi être affectée par des coquilles en interaction. En particulier, pour les interactions changeantes en nombre, nous pourrions et devrions améliorer notre calcul en calculant entièrement la moyenne thermique, sans l'hypothèse de factorisation des intégrales thermiques. Cela nous permettrait d'écrire et de résoudre les équations de Boltzmann, même si ce n'est que numériquement, pour l'évolution des densités de nombre et des énergies moyennes. Nous pourrions alors utiliser ces résultats pour étendre tous les calculs que nous avons effectués dans ce document à la région de l'espace des paramètres que nous avons jusqu'à présent exclue en raison de notre ignorance de ce qui se passe au-delà de l'écoulement libre. Ce que nous avons calculé dans cette thèse sera important pour cette entreprise car il nous guidera vers le processus de free-streaming particulier qui est dominant et que nous devrions nous efforcer de calculer avec une plus grande précision.

En ce qui concerne plus spécifiquement les bubbletrons, les futures voies d'exploration comprennent des bubbletrons autres que ceux induits par des particules réfléchies rayonnées, ou dans la région où les coquilles ne s'écoulent pas librement, et d'autres applications pour la baryogénèse et d'éventuelles diffusions transplanckiennes dans l'univers primitif.

Enfin, en ce qui concerne la baryogénèse à partir de PT du premier ordre, après avoir démontré que le confinement permet d'étendre l'espace des paramètres jusqu'à l'échelle EW, il pourrait être intéressant d'étudier un modèle avec des neutrinos composites stériles, afin de déterminer si ce mécanisme permet de tester la leptogénèse dans les futurs collisionneurs.

Contents

Invitation

The Standard Model (SM) of particle physics was proposed around 50 years ago, and has been tested to remarkable and ever-increasing level of accuracy.

While explaining some parts of nature with astonishing precision, it is definitely not complete. From an experimental point of view it lacks an explanation of neutrino masses, observed via neutrino oscillations [1, 2]. It is also not able to explain astrophysical observations ranging over many scales, from galaxy rotation curves [3] over the bullet cluster [4] to the Cosmic Microwave Background (CMB) [5], which can be explained in the most natural way by extending the Standard Model by a dark matter (DM) candidate, see e.g. [6]. It further provides no mechanism capable of explaining the observed asymmetry in the observed abundance of matter and antimatter in the universe [7]. From a theoretical point of view it lacks a UV completion for gravity at the Planck scale, $\sim 10^{19}$ GeV [8]. One might also consider it unsatisfying that 19 unrelated and arbitrary constants are needed to describe the Standard Model. A partial solution to this is given by grand unified theories (GUTs), which provides a unified description of gauge interactions arising around $\sim 10^{15}$ GeV [9].

In this thesis we focus mostly on the open question of dark matter and matter/antimatter asymmetry. When the dark matter problem was established, physicists proposed WIMP as DM particles as the most natural solution. However, with direction detection experiments not having made a discovery (yet) and the Large Hadron Collider not finding New Physics close to the electroweak (EW) scale, there is sufficient motivation to steer away from the simplest DM scenarios. This includes building more exotic production mechanisms which can be tested through other observables by new experiments, and producing dark matter (DM) at different scales. We are particularly interested in heavier DM, potentially up to the GUT scale, providing another theoretical motivation. The mechanism to produce such heavy DM, which we propose in this thesis, relies on cosmological first order phase transitions with ultra-relativistic bubble walls, and has potential applications beyond heavy DM. A necessary input for the development of this mechanism is the computation of the evolution of particle shells at fast bubble walls, which is another original content presented in this thesis, and whose interest goes beyond this mechanism. Finally, first order phase transitions are a possible ingredient to build models which explain the matter/antimatter asymmetry of the universe, in this context the community has so far mostly focused on the EW PT and on the regime of slow walls. In this thesis we present novel results that allow to produce the baryon asymmetry in PTs with ultra-relativistic bubble walls, for scales of the PT that can be as low as the EW one.

This thesis is organized as follows. In Chapter I we give a general overview over first order phase transitions (FOPT), with the purpose to set up the framework and to fix notations. We first investigate a toy model (dilaton) that can give rise to a PT. This is because in the Standard Model the EW PT is not a first order phase transition, but a crossover [13], and therefore an unsuitable model for our desired scenario. We then generalize away from a specific model to a general description of FOPTs, and introduce the relevant parameters for a phenomenological description. We describe the dynamics of the nucleation process, in particular the creation and expansion of bubbles until their collision with other bubbles, and the influence of particle driven pressure on the speed of the bubble expansion. Particles interacting with the wall, the boundary of the bubble, will accumulate in thin, possibly ultra-relativistic shells. We categorize the thickness, density, and typical energy of particles in these shell for various models. Last, we provide details how a first order phase transition gives rise to a gravitational wave signature, expected to be observed at for example LISA and Einstein Telescope and pulsar timing arrays.

In Chapter II, based on [14], we investigate the effects that modify the evolution of shells, from the point of creation until the point of collision with neighboring shells. They change the number densities and the average energies of the particles in the shell, and can therefore be necessary to correctly compute any subsequent interactions of the shells. In particular, we investigate Compton and Moller scattering which could potentially reverse the direction of particles. The heart of the chapter deals with the computation of number changing interactions. Further we estimate the size of the phase space distribution function, essentially allowing us to understand when effects from high occupation numbers can be neglected. The quantitative study of all these effects allow us to identify the regions of parameter space, of any PT, where particle shells do and do not free stream.

In Chapter III, based on [15], we use our ability to trace the evolution of the particles until collision in order to correctly predict any processes happening due to scattering of particles between neighboring particles. We achieve this by safely avoiding any region in parameter space where free-streaming effects may become large. The large scattering energies can be used to produce heavy particles, realizing a 'bubbletron'. After having motivated why dark matter could be heavy, we apply the bubbletron to generate heavy dark matter. Most importantly, we calculate the largest dark matter mass that is achievable, depending on the energy scale of the PT.

In Chapter IV, based on [17], we investigate the possibility of using the mechanism of out-of-equilibrium particle production to explain baryogenesis. We investigate one model using confining phase transitions. The bubbletron mechanism allows this model to generate a baryon asymmetry for scales of the PT down to the EW one, orders of magnitude smaller than in previous analogous models that instead relied on weakly-coupled PTs. This opens up new interesting ways of testing this baryogenesis model, for example at colliders, and to connect it with EW symmetry breaking.

We conclude by summarizing the new results we have found during this thesis. We also give an outlook on what can be improved in our calculation and on the applications, beyond the ones investigated in this thesis, for which our results are not only interesting, but also relevant and important.

I – First Order Phase Transitions

Along with the electroweak (EW) and QCD transitions, known to be crossovers in the Standard Model (SM) [13, 18], one or more first order phase transitions (FOPTs) may have taken place as the universe expands in the first second after inflation. They are indeed commonly predicted in several motivated extensions of the SM, such as extra-dimensional [19], confining [20, 21], or supersymmetric models [22], and solutions to the strong CP [23, 24], flavour [25], or neutrino mass problems [26]. Independently of where they come from, such early universe phase transitions may have far reaching consequences through the possible cosmological relics they can leave behind, e.g. primordial black holes [27–37], topological defects [38–42], magnetic fields [43–49], dark matter (DM) [50–59], the baryon asymmetry of the universe (BAU) [60–72], together with a background of gravitational waves (GW) [73–82], to cite just a few.

As the universe expands, sitting in its lowest free energy vacuum, another vacuum may develop at a lower energy due to the fall in temperature, eventually triggering a PT. If a PT is first order then it proceeds via the nucleation of bubbles of broken phase into the early universe bath (see e.g. [83, 84] for reviews), analogously to the PT of water to vapor.

In this chapter we give an introduction to FOPTs and to collect relevant formulae for use in later chapters. We begin by investigating the dilaton as a toy model in Sec. I.1 in order to gain a hands-on understanding of FOPTs. Abandoning this example we move on and define all the parameters necessary to describe a general FOPT in Sec. I.2. We explain how bubbles nucleate and expand with possibly ultra-relativistic wall velocities in Sec. I.4. Finally, we conclude by describing the GW signal in Sec. I.5. The production of gravitational waves is arising solely due to the FOPT, so we describe it here and reference any appearance in later chapters to this section.

I.1 Example: dilaton

Here we investigate the dilaton as a toy model to show an example of how a first order phase transition can arise.

The dilaton is the pseudo-Goldstone boson of conformal symmetry. It can be parameterized by [85]

$$\chi(x) = v_\phi \exp\left\{\frac{\sigma(x)}{v_\phi}\right\}, \tag{I.1}$$

where v_ϕ is the scale of the phase transition and $\sigma(x)$ transforms non-linearly as $\sigma(x)/v_\phi \to \sigma(e^\lambda x)/v_\phi + \lambda$.

To induce the spontaneous symmetry breaking we have to introduce an explicit breaking, parameterized as [86]

$$V_\chi^{T=0} = c_\chi g_\chi^2 \chi^4 \left[1 - \frac{1}{1+\gamma_\epsilon/4}\left(\frac{\chi}{v_\phi}\right)^{\gamma_\epsilon}\right], \tag{I.2}$$

where

$$\gamma_\epsilon \simeq -\frac{1}{4}\frac{m_\chi^2}{c_\chi g_\chi^2 v_\phi^2} < 1\,. \tag{I.3}$$

Here $m_\chi = \mathcal{O}(\chi)$ is the dilaton mass, we fix $c_\chi = 1$, and, for concreteness thinking of the dilaton as a composite state from a confining sector which is nearly conformal in the UV, we choose the coupling constant to reproduce glueball normalization, $g_\chi \simeq 4\pi/N$, with N the rank of the confining gauge group.

The CFT bosons charged under the confining gauge group contribute towards the leading order finite temperature corrections to the potential [76, 86],

$$V^T(\chi, T) = \sum_i \frac{nT^2}{2\pi^2}\, J_B\left(\frac{m_i^2}{T^2}\right), \tag{I.4}$$

with $m_i \simeq g_\chi \chi$ and $\sum_i n = 45N^2/4 = g_\phi$, fixed to this value in order to reproduce the free energy of $\mathcal{N} = 4\mathrm{SU}(N)$ large N super-YM dual to an AdS-Schwarzschild spacetime [19]. The function J_B accounts for the plasma density of the bosons,

$$J_B(x) = \int_0^\infty \mathrm{d}k\; k^2 \ln\left(1 - e^{-\sqrt{k^2+x}}\right), \tag{I.5}$$

implying that for simplicity we neglect contributions from any fermions. Assuming further that the dilaton still exists in the deconfined phase with all its degrees of freedom, we have for the total potential

$$V_{\mathrm{tot}}(\chi, T) = V_\chi^{T=0}(\chi) + V^T(\chi, T)\,. \tag{I.6}$$

We show the behavior of Eq. (I.6) in Fig. I.1, for suitable chosen values of the other parameters, and an anticipated value of the so-called nucleation temperature T_{n}. To understand this, consider a universe composed of radiation and vacuum energy (the dilaton), with energy densities given by

$$\rho_{\mathrm{r}} = g_{\mathrm{Ri}}\,\frac{\pi^2}{30}T^4\,, \qquad\qquad \rho_{\mathrm{vac}} = c_{vac} v_\phi^4\,, \tag{I.7}$$

where $g_{\mathrm{Ri}} = g_{\mathrm{SM}} + g_\phi$ are the inital effective degrees of freedom. For the dilaton, $c_{\mathrm{vac}} = m_\chi^2/(16 v_\phi^2)$. In the early thermal history of the universe, the temperature is large, and radiation dominates over the vacuum energy density. They become equal at a temperature T_{eq}, given by

$$T_{\mathrm{eq}} = \left(\frac{30 c_{\mathrm{vac}}}{g_{\mathrm{Ri}}\pi^2}\right)^{1/4} v_\phi\,. \tag{I.8}$$

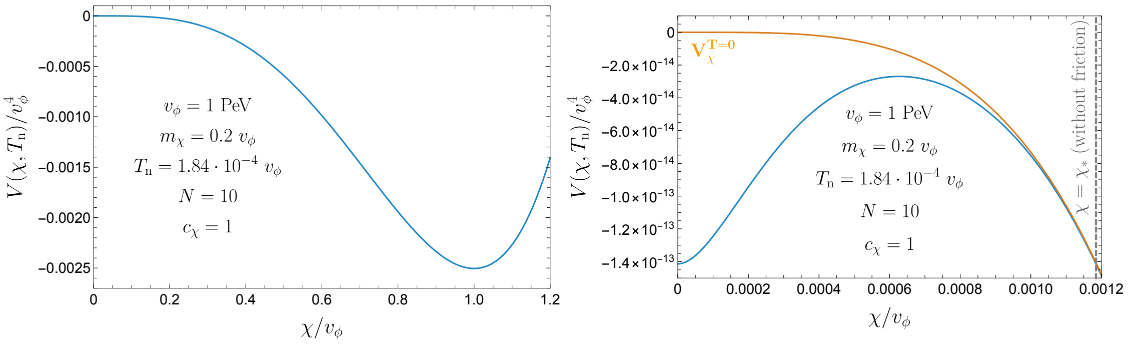

Figure I.1: **Left**: light-dilaton potential with first-order temperature corrections. **Right**: zoom in onto the thermal barrier, with zeroth-order vaccum potential in orange, and tunneling point χ_* for neglected friction.

At this point the contribution from the vacuum energy becomes relevant, and the shape of the potential begins to matter. The dilaton still resting at the false vacuum at $\langle\chi\rangle = 0$ has a non-zero probability to tunnel through the thermal barrier depicted in the right-hand side of Fig. I.1, and reach its true vacuum state at $\langle\chi\rangle = v_\phi$, seen on the left-hand side of Fig. I.1.

We compute the temperature of the tunneling by solving

$$\Gamma(T_\mathrm{n}) \simeq H(T_\mathrm{n})^4\,, \tag{I.9}$$

where [87, 88]

$$\Gamma(T) = R_0^{-4}\left(\frac{S_4}{2\pi}\right)^2 \exp\left\{S_4\right\} \tag{I.10}$$

is the tunneling rate per volume. Here $R_0 \simeq 1/T_\mathrm{n}$ is the tunneling radius at nucleation and

$$S_4 = 2\pi^2 \int \mathrm{d}r\ r^3 \left[\frac{1}{2}\phi'(r)^2 + V(\phi(r))\right] \tag{I.11}$$

is the $O(4)$ bounce action with solution

$$\phi''(s) + \frac{3}{s}\phi'(s) \pm \frac{\mathrm{d}V(\phi)}{\mathrm{d}\phi} = 0\,, \tag{I.12}$$

with boundary conditions

$$\phi'(0) = 0\,, \qquad \lim_{s\to\infty}\phi(s) = 0\,. \tag{I.13}$$

Note that the ± in the equation of motion corresponds to the light-like (+) light-cone coordinate $s = \sqrt{t^2 - \vec{r}^2}$ and to the space-like (−) light-cone coordinate $s = \sqrt{\vec{r}^2 - t^2}$. From the shape of the differential equation in Eq. (I.12) we expect the light-like (+)

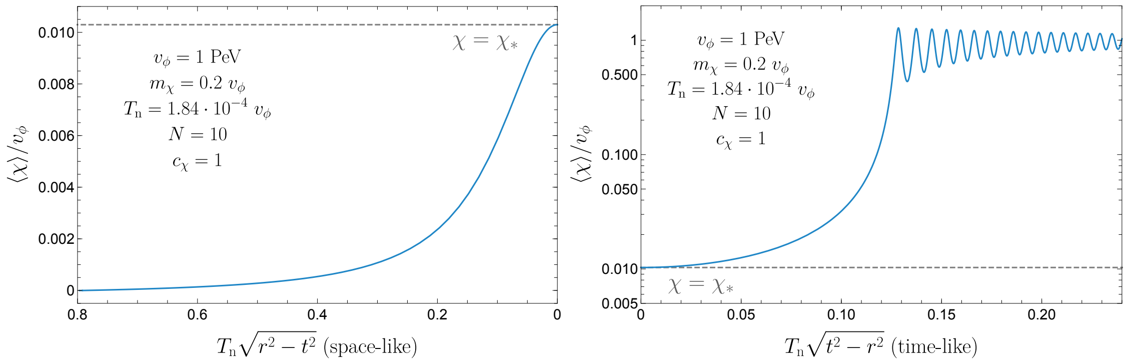

Figure I.2: ***Left**: dilaton profile before nucleation. A transition is taking place from the false, meta-stable vacuum at $\langle\chi\rangle = 0$ towards the nucleation point χ_*. **Right**: evolution after tunneling. The field rolls down the potential and then oscillates in the valley around the true vacuum at $\langle\chi\rangle = v_\phi$. The oscillations with period $\sim v_\phi^{-1}$ get damped with damping time $\sim T_\mathrm{n}^{-1} \gg v_\phi^{-1}$ via friction [55].*

solution to be oscillating and the and space-like $(-)$ solution to be exponentially decaying, both behaviors damped by the friction term $\phi'(s)$.

We show the solution to the equations of motion in Fig. I.1. One solves the space-like solution by guessing an initial value χ_* for $\chi(0)$ using the over-shoot/under-shoot method. The solution is plugged back into the bounce action, integrated, and then solved for the nucleation temperature T_n using Eq. (I.9). Since the T_n is required as an input for the potential and therefore the solution to the equations of motion, this definition is circular. Solving in this case means trying different values for T_n until Eq. (I.9) is satisfied.

We estimate the tunneling point χ_* using energy conservation by neglecting the friction term in equation (I.12). It follows

$$V_\mathrm{tot}(\chi_*, T) \simeq V_\mathrm{tot}(0, T) \qquad \Rightarrow \qquad \frac{\chi_*}{v_\phi} \simeq \frac{1}{\sqrt{2}\ln(v_\phi/\chi_*)^{1/4}}\frac{T}{T_c}\,, \tag{I.14}$$

where

$$T_\mathrm{c} = \left(\frac{2|\gamma_\epsilon| c_\chi g_\chi^2}{\pi^2 N^2}\right)^{1/4} v_\phi\,. \tag{I.15}$$

Solving this for $T = T_\mathrm{n}$ and for the same values of the other parameters as in Fig. I.1, we find $T_\mathrm{c} = 0.0012 v_\phi$, as indicated with the gray dashed line in Fig. I.1. Numerically we find $T_\mathrm{n} = 0.010 v_\phi$. The big difference is due to having neglected the friction term in Eq. (I.12).

The computed values depend on the shape of the potential, and therefore on the model of the phase transition. The general principle however stays the same. Since the dilaton is not the focus of this thesis, we now abandon it in favor of defining the PT by general parameters in the next section.

I.2 Useful definitions

In this section we define a FOPT via a few key parameters, which can be computed for specific models, and will serve as input parameters during the following chapters.

The vacuum energy before the PT is defined via

$$\Delta V \equiv \Lambda^4 = c_{\mathrm{vac}} v_\phi^4 \,, \tag{I.16}$$

where c_{vac} ranges from $\mathcal{O}(1)$ to $\mathcal{O}(10^{-3})$ for typical models. We call v_ϕ the (energy) scale of the PT, which can be thaught as the zero-temperature vacuum expectation value of an order parameter ϕ, which in the example of the previous section is the dilaton.

The radiation density is given by

$$\rho_{\mathrm{rad}} = \frac{g_R \pi^2}{30} T^4 \,. \tag{I.17}$$

The temperature at which the nucleation of bubbles start is the so-called nucleation temperature, T_{n}.

We assume that the phase transition takes place during the vacuum dominated phase of the universe, which starts for temperatures smaller than $T)$eq,

$$T_{\mathrm{eq}} = \left(\frac{30 c_{vac}}{g_{\mathrm{Ri}} \pi^2}\right)^{1/4} f \,. \tag{I.18}$$

After the PT is completed, the universe is reheated to

$$T_{\mathrm{RH}} = \left(\frac{g_{\mathrm{Ri}}}{g_{\mathrm{Rf}}}\right)^{1/4} T_{\mathrm{eq}} \,, \tag{I.19}$$

unless the width of ϕ is much smaller than the Hubble scale at the time of the PT, a case in which we won't be interested in the rest of this thesis.

The initial (i) and final (f) degrees of freedom are given by

$$g_{\mathrm{Ri}} = g_{\mathrm{SM}} + g_{\mathrm{BSM}} \,, \tag{I.20}$$

$$g_{\mathrm{Rf}} = g_{\mathrm{SM}} \,, \tag{I.21}$$

with $g_{\mathrm{SM}} = 106.75$ the effective degrees of freedom due to SM particles at temperatures larger than the EW scale and g_{BSM} the contribution from new particles.

In case $T_{\mathrm{n}} \ll v_\phi$, the PT is supercooled.

It further proves useful to define two quantities, α and β, which are needed to compute the GW signal. They are defined as

$$\alpha \equiv \frac{\Delta V}{\rho_{\mathrm{rad}}(T_{\mathrm{n}})} = \left(\frac{T_{\mathrm{eq}}}{T_{\mathrm{n}}}\right)^4 , \tag{I.22}$$

the ratio of latent heat over radiation energy density, and

$$\beta \equiv \frac{1}{\Gamma} \frac{\mathrm{d}\Gamma}{\mathrm{d}t} \,, \tag{I.23}$$

where Γ is the tunneling rate per volume [87, 88]. The latter therefore measures the change of the tunneling rate, which implies that β^{-1} serves as an estimate of the typical distance between nucleation centers of different bubbles and of the duration of the PT. Typically the distance is shorter than a Hubble length H^{-1}.

I.3 Bubble wall velocities

The bubble walls are defined as the spherically symmetric regions of space where the background field ϕ rapidly varies, from the high-temperature value outside the bubble, to v_ϕ inside it. The pressure density inside is larger than outside, driving the expansion of the bubbles. If friction pressure on the walls is negligible, then they run away with a Lorentz boost $\gamma(R) = 2R/(3R_\mathrm{n})$ [89], where R is the bubble radius and $R_\mathrm{n} \approx T_n^{-1}$ is the average distance between nucleation centers, see e.g. [55]. If the walls run away until colliding, they reach

$$\gamma_\mathrm{run} = \frac{2R_\mathrm{c}}{3\,R_\mathrm{n}} \simeq 2.7 \cdot 10^{14} \cdot \frac{T_\mathrm{n}}{T_\mathrm{eq}} \frac{\mathrm{TeV}}{v_\phi} \frac{1}{(c_\mathrm{vac} g_\mathrm{Ri})^{1/4}} \frac{20}{\beta/H} \tag{I.24}$$

where $R_\mathrm{c} \simeq (\pi)^{\frac{1}{3}} \beta^{-1}$ is their radius at collision [90], and we have assumed $T_n \leq T_\mathrm{eq}$ so that $H \simeq \sqrt{c_\mathrm{vac}/3}\; v_\phi^2/M_\mathrm{Pl}$.

A number of effects can exert pressure on walls and slow them down. Collisional plasma effects are expected to exert a negligible pressure for $T_n \lesssim T_\mathrm{eq}$ (see e.g. [91–94]), which is the case we will be interested in. One then enters the so-called ballistic regime, where particle interactions can be neglected. Then, one has pressure from single particles getting a mass across the wall, $\mathcal{P}_\mathrm{LO} = g_* \Delta m^2\, T_\mathrm{n}^2/24$ [95], with g_* the number of degrees of freedom getting an average mass squared $\Delta m^2 \propto v_\phi^2$ at the PT. Another pressure that could be relevant in some models, $\mathcal{P}_\mathrm{heav}$, is that from degrees of freedom heavier than v_ϕ that couple to the particles that feel the PT [96]. $\mathcal{P}_\mathrm{LO}$ and $\mathcal{P}_\mathrm{heav}$ are both smaller than ΔV for $T_n^2 < v_\phi^2$, up to order-one model-dependent coefficients. In this case the velocity of the bubble walls becomes ultra-relativistic, which is the case we are interested in in this thesis.

Ultrarelativistic bubble walls can either run away until they collide with those of other bubbles, or reach a terminal velocity beforehand, set by yet another source of pressure given by the particle emitted by the bath and that get a mass m at wall crossing. If this transition radiation is soft-enhanced, as for emitted gauge bosons, then their pressure grows with γ [97]. Its size is enhanced by large logarithms, that have been resummed in [89], which gives the pressure

$$\mathcal{P}_\mathrm{LL} \simeq \frac{\zeta(3)}{\pi^4} g^2 g_\mathrm{eff}\, \gamma\, m_V\, T_n^3 \log(m_V/\mu)\,, \tag{I.25}$$

where g is the gauge coupling, g_eff a weighted sum of the radiating degrees of freedom times their charges, m_V is the gauge boson mass and μ a physical IR cut-off.[1] If $\mathcal{P}_\mathrm{LL}(\gamma)$ reaches $\Delta V = c_\mathrm{vac} v_\phi^4$ before collision, then walls reach a terminal velocity

$$\gamma_\mathrm{LL} \simeq 3.5 \cdot 10^4 \cdot \left(\frac{T_\mathrm{eq}}{T_\mathrm{n}}\right)^3 \left(\frac{0.1}{g}\right)^3 \left(\frac{c_\mathrm{vac} g_\mathrm{Ri}^3}{10^4}\right)^{1/4} \frac{10}{g_\mathrm{eff} \log \frac{m_V}{\mu}}\,, \tag{I.26}$$

where we have chosen $m_V = g v_\phi$ for definiteness. The typical boost of bubble walls at collision then is

$$\gamma_\mathrm{coll} \simeq \mathrm{Min}\big[\gamma_\mathrm{LL},\, \gamma_\mathrm{run}\big]. \tag{I.27}$$

---

[1] The only two other sources of pressure, which we are aware of, are those from string fragmentation in confining PTs [55] and that from vectors that get from the wall only a small component of their mass [98]. Neither of them applies to the considered scenarios in this thesis.

In Fig. I.3 we show the boost factor at collision $\gamma_{\rm coll}$ in Eq. (I.27), showing that it becomes large for small values of the scale of the PT v_ϕ.

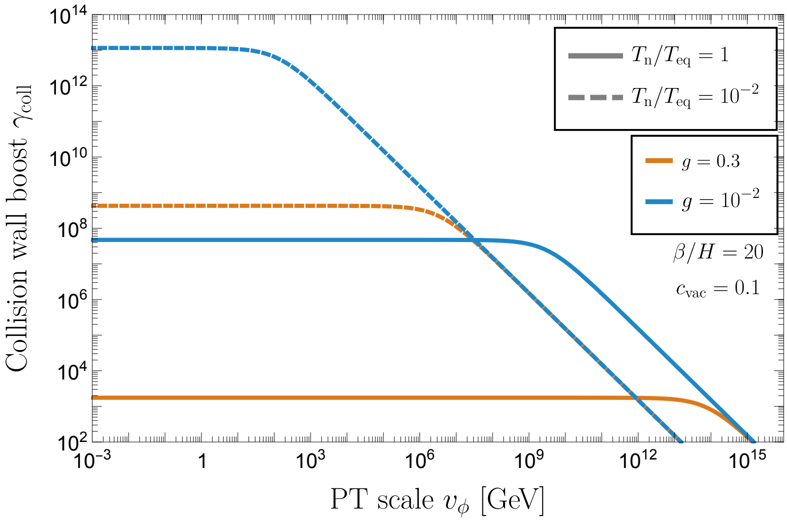

Figure I.3: Boost factor at collision $\gamma_{\rm coll}$ for a gauge boson radiated and reflected at the wall of a bubble, with terminal velocity determined by Eq. (I.25).

Large boosts at collision are realised for small gauge coupling g, or for large v_ϕ/T_n, or in global (rather than gauged) PTs because there $\mathcal{P}_{\rm LL}$ does not grow with γ.

I.4 Shells of particles at the wall

Due to interactions with the bubble wall, particles will accumulate in thin, dense regions at the wall. We call this region the shell of the bubble wall. The thickness of the shell depends on the types of particles considered. Here we exemplarily compute the thickness of such shells for a massless particle accumulating in front of the wall, such that our discussion applies for example to radiated gauge bosons (the same ones that are responsible for $\mathcal{P}_{\rm LL}$ of Eq. (I.25)) which are reflected at the wall.

We define the distance x of a shell particle from the wall via

$$\int_0^x {\rm d}r = \int_{t_{ej}}^{t_{\rm c}} {\rm d}t\,(v_{\rm p} - v_{\rm w}(t)) = \int_{r_{\rm ej}}^{R_{\rm c}} \frac{{\rm d}r}{v_{\rm w}}(1 - v_{\rm w})\,, \tag{I.28}$$

$$x = \int_{r_{\rm ej}}^{R_{\rm c}} {\rm d}r \left(\frac{1}{v_{\rm w}} - 1\right). \tag{I.29}$$

where $r_{\rm ej}$ is the radius where the particle has been ejected. The size of the shells is set by the particles which have been ejected the earliest, for which $r_{\rm ej} \simeq 1/T_{\rm n}$.

I.4.1 Runaway regime

Here we use we use that the bubble wall velocity γ scales linearly with the radius r in the runaway regime, $\gamma_{\rm w}(r) \simeq T_{\rm n} r$.. The exact solution is given by

$$r_{\rm ej}(x) = \frac{1}{2}\Big(R_{\rm c} - \sqrt{R_{\rm c}^2 - \tfrac{1}{T_{\rm n}^2}} + x\Big) + \frac{1}{2T_{\rm n}^2\Big(R_{\rm c} - \sqrt{R_{\rm c}^2 - \tfrac{1}{T_{\rm n}^2}} + x\Big)} \tag{I.30}$$

I.4.2 Terminal velocity regime

For the terminal velocity regime we split the integral into two parts. In the first part we still have runway behavior $\gamma_{\rm w}(r) \sim r$, in the second part the velocity is constant. The radius of equality is fixed by $T_{\rm n} r_{\rm eq} = \gamma_{\rm max}$. Then we have to split the integral into two parts, and we have

$$x = \left[\sqrt{r^2 - \frac{1}{T_{\rm n}^2}} - r\right]_{r_{\rm ej}}^{r_{\rm eq}} + \left(\frac{1}{\sqrt{1 - 1/\gamma_{\rm max}^2}} - 1\right)(R_{\rm c} - r_{\rm eq}) \tag{I.31}$$

The exact solution is

$$r_{\rm ej}(x) = \frac{B(x)}{2} + \frac{1}{2T_{\rm n}^2 B(x)}\,, \tag{I.32}$$

$$B(x) \equiv x + r_{\rm eq} - \sqrt{r_{\rm eq}^2 - \tfrac{1}{T_{\rm n}^2}} - \left(\frac{1}{\sqrt{1 - 1/\gamma_{\rm max}^2}} - 1\right)(R_{\rm c} - r_{\rm eq})\,. \tag{I.33}$$

The thickness of the shell is then given by the maximal value of x. For this particular example we find that

$$L_{\rm p} \simeq \frac{1}{\gamma_{\rm coll} T_{\rm n}} \tag{I.34}$$

is a good approximation in the runaway regime and in the terminal velocity regime, and $\gamma_{\rm coll}$ is the wall velocity reached at collision.

We derive now the general expression, applicable to all models. We start similarly as in Eq. (I.28)

$$x = \int_{t_p}^{t_c} {\rm d}t\, [v_{\rm p}(t_p) - v_{\rm w}(t)] = \int_{t_{\rm p}}^{t_c} {\rm d}t \left(\frac{1}{2\gamma_{\rm w}^2(t)} - \frac{1}{2\gamma_{\rm p}^2(t_p)}\right) = \left(\frac{1}{2T_{\rm n}^2 t_p} - \frac{t_c - t_p}{2\gamma_q^2(t_p)}\right)\,, \tag{I.35}$$

but now we have expanded before integrating instead of expanding after integrating. Here v_p and t_p are the velocity and ejection time of the particle in the shell.

For massless particles moving faster than the wall, $\gamma_q \to +\infty$, we get

$$L_p \simeq \frac{1}{\gamma_{\rm w} T_{\rm n}} \qquad \Longrightarrow \qquad L_w \simeq \frac{1}{T_{\rm n}}\,, \tag{I.36}$$

in the plasma and wall frame, respectively.

In the opposite case, for massive particles moving slower than the wall we get

$$L_p \simeq \frac{R_c}{\gamma_q^2} \qquad \Longrightarrow \qquad L_w \simeq \frac{\gamma_w}{\gamma_q}\frac{R_c}{\gamma_q}\,, \tag{I.37}$$

with $R_c \simeq t_c - t_p \simeq \beta^{-1}$ the bubble radius at collision.

If $\gamma_q \simeq \gamma_w$, then we have $L_p \simeq 1/\gamma T_n$, reproducing the result in Eq. (I.34). At the end the precise value of shell thickness L_p does not matter since the abundance in Eq. (III.8) is independent of L_p.

We note that we have derived the general expression for the thickness of the wall in the runaway regime. However, we find that they are also a good approximation, at most an overestimate, in the terminal velocity regime.

We note that the particles are not distributed with equal density in the shell, in fact the most dense region contains the particles which have been ejected the latest. One can therefore define an effective thickness L_{eff} such that $\langle n\rangle \cdot L_{\text{eff}} 4\pi R^2$ equals the number of particles in the shell. Usually the effective thickness is of the same scaling, see e.g. $L_{\text{eff}} \sim 1/(2T_n^2 R_c)$ in [55].

I.4.3 Summary of different models producing shells

We have shown the explicit calculation of the thickness of a shell for a specific scenario. However, there exist further mechanisms causing particles to accumulate into shells due to the same origin of the pressures slowing down the expansion of the wall. We list them below.

1. Particles acquiring their mass [72, 95];
2. Particles radiated and transmitted in the wall [89];
3. Heavier particles if produced by lighter ones that feel the PT [72, 96, 99];
4. In confining PTs, hadrons from string fragmentation [55];
5. Vectors acquiring a small part of their mass [98];
6. Particles produced by oscillations of the wall ϕ [100];
7. In confining PTs, ejecta from string fragmentation [55];
8. Particles radiated and reflected by the wall [89].

Shells 1 to 6 follow the bubble walls, shells 7 and 8 precede them. When bubbles collide, also these shells do. If their constituent particles still have an energy much larger than v_ϕ by that time, then they realise what we define a bubbletron. We present key parameters in Tab. I.1.

Channel	Multiplicity $\mathcal{N}$ per incoming particle	Momentum p_X	Shell thickness L_p
Leading-order interaction: particles acquiring a mass [95, 101]	1	$\frac{\Delta m}{T_\mathrm{n}}\ \Delta m$	$R_c\left(\frac{T_\mathrm{n}}{\Delta m}\right)^2$
Gauge interaction $g \ll 4\pi$: bremsstrahlung radiation [89, 96–98]	$\frac{g^2}{4\pi}\ \ln^2\#$	$\gamma\, g v_\phi$	$\frac{1}{\gamma T_\mathrm{n}}$
Gauge interaction $g \simeq 4\pi$: hadronization [55, 57]	$\frac{g^2}{4\pi}\ \ln\frac{\gamma T_\mathrm{n}}{v_\phi}$	γv_ϕ	$\frac{1}{\gamma T_\mathrm{n}}$
Non-adiabatic production of heavier particles [56, 72, 99, 102]	$\gamma^2 v_\phi^2/M_\mathrm{X}^2$ $\Theta(\gamma - M_\mathrm{X}^2/(T_\mathrm{n} v_\phi))$	$\frac{M_\mathrm{X}}{T_\mathrm{n}}\ M_\mathrm{X}$	$R_c\left(\frac{T_\mathrm{n}}{M_\mathrm{X}}\right)^2$

Table I.1: *Primary particle production mechanism generated by the motion of the wall. All quantities are expressed in the plasma frame and do not include effects from interactions between particles. R_c is the bubble radius at collision. Gauge interactions give rise to particles being reflected and particles being transmitted at the wall. Both their quantities have the same scaling but different $\mathcal{O}(1)$ factors.*

I.5 Gravitational wave signal

We finally compute the GW spectrum generated by the PT for ultra-relativistic bubble walls. According to whether their Lorentz factor γ_coll is set by γ_run or γ_LL in Eq. (I.27), the latent heat fraction α (see Eq. (I.22)) of the PT is either kept in the bubble wall kinetic energy or is transferred to the plasma in the form of ultra-relativistic shocks. In the former case, the GW spectrum is given by the bulk flow model [79], which has been calculated analytically [79] and numerically [80, 82, 103, 104]. It extends the envelop approximation [75, 77] by accounting for the propagation of bubble wall remnants long after the collision. In the latter case, ultra-relativistic shocks can be described by extremely thin and long-lived shells of the stress-energy tensor [105]. From a gravitational point of view, they should be indistinguishable from stress-energy profile stored in the scalar field. Hence, the bulk flow model should offer a good description of the GW spectrum (see also [103]). First results in the moderately-relativistic regime $\gamma_\mathrm{coll} \lesssim 10$ support this choice [101].

We take the GW spectrum $\Omega_\mathrm{GW}h^2$ in the bulk flow model from [80],

$$\Omega_{GW}(\nu) = \overline{\Omega}_{GW} S_\phi(\nu)\,, \tag{I.38}$$

where $\overline{\nu}$ is the peak frequency given by

$$\tilde{\nu} = 33\,\mu\mathrm{Hz}\left(\frac{g_*(T_{RH})}{100}\right)^{1/6}\frac{\beta}{H}\left(\frac{T_\mathrm{RH}}{10^3\ \mathrm{GeV}}\right). \tag{I.39}$$

and $\overline{\Omega}_{GW}$ is the amplitude of the energy spectrum. The shape of the spectrum is governed by the spectral function

$$S_\phi(\nu) = \frac{(a+b)\tilde{\nu}^b\nu^a}{b\,\tilde{\nu}^{(a+b)} + a\,\nu^{(a+b)}}\,, \tag{I.40}$$

where we adopt the central values for the bubbles in the setup with the thickest walls from [104], namely $a = 0.742$ and $b = 2.16$.

Using the numerical results from [104], the GW energy density power spectrum as measured today, for initially thick walled, runaway bubbles scales as

$$h^2\Omega_{GW}(\nu) \equiv h^2 \frac{\mathrm{d}\Omega_{GW}}{\mathrm{d}\ln(\nu)} = 4.4 \times 10^{-7} \left(\frac{100}{g_*(T_{RH})}\right)^{1/3} \left(\frac{\alpha}{1+\alpha}\right)^2 \frac{S_\phi(\nu)}{(\beta/H)^2} \,. \tag{I.41}$$

Finally we impose that $\Omega_{GW} \propto \nu^3$ due to causality for super-horizon modes at GW production [106–109]. We therefore apply a cut in the spectrum at the redshifted frequency today of

$$\nu^*(t_0) = \frac{a(T_{\mathrm{RH}})}{a_0} \frac{H(T_{\mathrm{RH}})}{2\pi} \,, \tag{I.42}$$

below which we enforce the correct IR scaling by hand and where $a(T_{RH})/a_0$ is the ratio of the scale factors between the PT and today.

We will show the GW spectra in Fig. III.5 and Fig. IV.3.

Gravity waves from PTs can be probed by several current or upcoming GW interferometers, like Pulsar Timing Arrays, LISA and the Einstein Telescope. The sensitivity of a detector to a GW signal is given by

$$\Omega_{\mathrm{sens}}(\nu) = \frac{4\pi^2}{3H_0^2} \nu^3 S_n(\nu) \,, \tag{I.43}$$

where H_0 =100 h km/s/Mpc is the present day Hubble parameter and S_n is the noise spectral density, which depends on the respective experiment. The signal to noise ratio SNR to a GW background is given in terms of the above quantities as

$$\mathrm{SNR} = \sqrt{T \int_{\nu_{\min}}^{\nu_{\max}} d\nu \left(\frac{\Omega_{GW}(\nu)}{\Omega_{\mathrm{sens}}(\nu)}\right)^2} \,, \tag{I.44}$$

where $\nu_{\min}$ and $\nu_{\max}$ are the minimal and maximal frequencies accessible at the detector and T is the fiducial observation time. Using this expression, the so called power-law-integrated (PLI) sensitivity curves are computed [110], and our calculations for the ET [111] and LISA [112] PLI sensitivity curves are shown in Fig. IV.2, for a fiducial choice of SNR=5. There are several astrophysical stochastic GW foregrounds in the ET and LISA frequency range which could mimic the GW signal coming from the PT. In order to take this limitation into account we also define a foreground-limited signal to noise ratio,

$$\mathrm{SNR}_{\mathrm{FGL}} = \sqrt{T \int_{\nu_{\min}}^{\nu_{\max}} d\nu \left(\frac{\mathrm{Max}[\Omega_{\mathrm{GW}}(\nu) - \Omega_{FG}(\nu), 0]}{\Omega_{\mathrm{sens}}(\nu)}\right)^2} \,. \tag{I.45}$$

With the above conservative definition we impose that our signal is not detectable if buried under $\Omega_{\mathrm{FG}}(\nu)$.

II – Free-streaming of shell particles

While the particles travel from their creation at the bubble wall to the point of (head-on) collision with particles from other shells, they interact with each other and with the particles in the thermal bath of the universe. Computing the effect on the particles' energy, number density, etc. has proven to be a too optimistic wish for now. We will therefore leave this for future work, and focus on listing all the possible effects which can prevent shell particles from free-streaming, and on determining the parameter space for which we can neglect these effects, i.e. where the particles stream freely. These completely novel computations, which have only been partially approached in [55, 89, 99], constitute a necessary input for standard predictions of PTs, like gravitational waves and particle production (the latter being another novel subject of this thesis), and a first step to study the evolution and implications of interacting shells.

In Sec. II.1 we compute the momentum loss a particle in the shell experiences due to moving through a, from its point of view highly boosted, plasma. In Sec. II.2 we estimate whether due to the same effect, but viewed from a particle from the bath, the particle in the bath experiences a boost large enough to reverse its momentum, and therefore reduce the incoming flux of particles at the wall. In Sec. II.3 we estimate the region where we can neglect Boes-Einstein and Fermi-Dirac phase space distribution functions. In Sec. II.4 we compute the rate of number-changing interactions of particles from the shell with themselves and with the bath, which would lead to reaching some form of equilibrium. In Sec. II.5 we present the results of our computations in the form of colored regions in the parameter space of the PT. In these regions traditional results, e.g. for GWs produced by PTs, may need to be re-evaluated.

II.1 Shell momentum loss

Consider a shell produced on either side of the wall and propagating outwards from the nucleation site in the same direction of the wall. Particles in the shell will see an incoming flux of particles from the thermal bath. Interactions with these bath particles may change the momentum of the shell particles and therefore modify the overall properties or propagation of the shell. Also the bath particles may be affected by the shell and perhaps the flux of particles reaching the wall be suppressed or otherwise modified. We identify the following possibilities:

- Reversal of the shell: consider a shell traveling in front of the wall. In the plasma frame, both wall and shell travel at close to the speed of light, but the shell is slightly faster than the wall. Interactions with the bath particles may lead to a change in momentum of the shell particles, insufficient for dissipation, but sufficient to slow the shell particles so that the latter are caught by the wall. The picture in the wall frame is the following: Shell particles travel outward with momentum $p_{\mathrm{X,w}}$. Typically, one has $p_{\mathrm{X,w}} \sim v_\phi$ in the wall frame. Incoming bath particles have momentum $\sim \gamma T$. These interact with the shell particles and if the change of momentum of the latter in the wall frame is $\Delta p_X \sim p_X$ before the shells collide, then the shell particles are typically caught by the wall. More concretely, the condition to avoid the shell reversal is given by

$$\left.\frac{d\log(p_{\mathrm{x,w}})}{dt}\right|_{\mathrm{wall}} < \frac{\gamma}{R_c}, \tag{II.1}$$

where the γ factor takes into account the shorter propagation distance before wall collision in the wall frame. Note in the wall frame the density of bath particles is also Lorentz boosted $\sim \gamma T^3$.

- Shell dissipation: In the extreme case the shell may be completely dissipated. Consider particles traveling outward with momentum p_{X} in the plasma frame. Depending on the nature of the shell, we can have $p_{\mathrm{X}} \simeq \gamma v_\phi$ where γ is the Lorentz factor of the wall, or $p_{\mathrm{X}} \approx m_{\mathrm{X}}^2/T$. Then if interactions with the bath particles leads to changes in the shell particle momentum $\Delta p_{\mathrm{X}} \sim p_{\mathrm{X}}$ before the shells collide, then the shell will become dissipated back into the plasma. Two conditions can be met for this to be prevented. Either the momentum exchange is small over the distance of propagation, here taken to be the bubble size at collision,

  $$\left.\frac{d\log(p_{\mathrm{X}})}{dt}\right|_{\mathrm{plasma}} < \frac{1}{R_c}. \tag{II.2}$$

  Or, alternatively, if the total energy in the shell particles is larger than the total energy in the bath particles, $E_X > E_{\mathrm{bath}}$, the latter cannot dissipate the former. Depending on the underlying interactions, a shell traveling in front of the wall can be reversed without being dissipated, or the reversal and dissipation lengths can coincide, as we shall see below.

- Reversal of the bath: If a relativistic shell is traveling in front of the wall, its interactions with the bath may reverse the bath particles, and prevent them from reaching the wall. This in turn cuts off the shell production sourced from the bath particles interacting with the wall, and therefore alters the dynamics of shell production and propagation. In the wall frame the bath particles carry momentum $p_a \simeq \gamma T_n$. To prevent reversal, we require the change in momentum to be smaller than the initial one, $\Delta p_a \sim p_a$. More precisely, the condition reads

  $$\left.\frac{d\log(p_{\mathrm{a}})}{dt}\right|_{\mathrm{wall}} < \frac{1}{L_w}, \tag{II.3}$$

  where L_w is the shell thickness in the wall frame. The detailed rate of course depends on the density of the shell particles.

In the following subsections, we go on to evaluate the dissipation/reversal conditions for the shell for different choices of underlying interactions in greater detail. In section II.2 the bath reversal is worked out in detail.

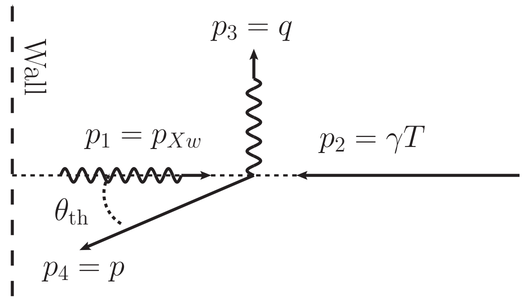

Figure II.1: The scattering — as seen in the wall frame — leading to the threshold at which point the reflected particle will head back to the wall.

II.1.1 Shell reversal

a) Basic picture

We first consider the gauge bosons created at the wall which are reflected back into the unbroken phase. Gauge bosons are of particular interest here because they obtain an enhanced production rate compared to fermions and scalars. The gauge bosons have a typical momentum in the wall frame $p_{\rm X,w} \approx m_{\rm broken} \sim g v_\phi$ and zero vacuum mass (accordingly, their momentum in the plasma frame is $p_{\rm X} = \gamma p_{\rm X} \sim \gamma g v_\phi$). We now derive the conditions for these to be sent back to the wall via interactions with the bath particles. The case of the shell particles interacting via t-channel gauge boson exchange has been worked out in [89], the results of which we confirm here using an alternative method to take into account the accumulated effect of many soft scatterings. We also consider Compton scattering, which is of relevance when U(1) gauge bosons interact with charged fermions or scalars in the bath, and which gives a longer path length. The limits from Compton scattering are therefore the relevant ones in the absence of $t-$channel gauge boson exchange processes.

b) Simple estimates

We work in the wall frame. The basic picture is illustrated in Fig. II.1. The gauge boson momentum before and after scattering is denoted p_1 and p_3 respectively. The bath particle momentum is denoted p_2 or p_4. The four momenta are

$$p_1 = (p_{\rm X,w}, \quad 0, \quad 0, \quad p_{\rm X,w})\,, \tag{II.4a}$$
$$p_2 = (\gamma T, \quad 0, \quad 0, \quad -\gamma T)\,, \tag{II.4b}$$
$$p_3 = (q, \quad 0, \quad q, \quad 0)\,, \tag{II.4c}$$
$$p_4 = (p, \quad 0, \quad -p\sin\theta_{\rm th}, \quad -p\cos\theta_{\rm th})\,. \tag{II.4d}$$

Here we are ignoring particle masses and γ is the Lorentz factor of the wall in the plasma frame. There are three unknowns, $q, p, \theta_{\rm th}$ and three equations from energy and momentum conservation

$$\begin{aligned}\gamma T + p_{\mathrm{X,w}} &= q + p\,, && \text{(II.5a)}\\ \gamma T - p_{\mathrm{X,w}} &= p\cos\theta_{\mathrm{th}}\,, && \text{(II.5b)}\\ q &= p\sin\theta_{\mathrm{th}}\,. && \text{(II.5c)}\end{aligned}$$

The solution to these equations is

$$\begin{aligned}q &= \frac{2p_{\mathrm{X,w}}\gamma T}{p_{\mathrm{X,w}}+\gamma T} \simeq 2p_{\mathrm{X,w}}\,, && \text{(II.6a)}\\ p &= \frac{p_{\mathrm{X,w}}^2+(\gamma T)^2}{p_{\mathrm{X,w}}+\gamma T} \simeq \gamma T\,, && \text{(II.6b)}\\ \sin\theta_{\mathrm{th}} &= \frac{2p_{\mathrm{X,w}}\gamma T}{p_{\mathrm{X,w}}^2+(\gamma T)^2} \simeq \frac{2p_{\mathrm{X,w}}}{\gamma T}\,, && \text{(II.6c)}\end{aligned}$$

where we have also given the approximate solution in the limit $\gamma T \gg p_{\mathrm{X,w}}$. Clearly then a small deflection of the incoming bath particle is sufficient to reverse the reflected particle. The momentum transfer squared is then

$$-\,\hat{t} = -(p_1 - p_3)^2 = 2\,p_1\cdot p_3 = 4p_{\mathrm{X,w}}^2\,. \tag{II.7}$$

Note that this is far below the center-of-mass energy squared $\hat{s} = 2p_1\cdot p_2 = 4\gamma T p_{\mathrm{X,w}}$. The momentum in the center-of-mass frame is likewise found in the massless limit $p_{\mathrm{com}}^2 = \hat{s}/4$.

Møller scattering.

We assume a matrix element inspired by $t-$channel gauge boson exchange, as in Møller scattering in regular QED, and consider the leading contribution in the $\hat{t}\to 0$ limit

$$|\mathcal{M}|^2 \approx 4g^4\frac{\hat{s}^2}{\hat{t}^2}\,. \tag{II.8}$$

This gives us

$$\frac{d\sigma}{d\hat{t}} = \frac{|\mathcal{M}|^2}{64\pi p_{\mathrm{com}}^2\hat{s}} \approx \frac{g^4}{4\pi\ \hat{t}^2}\,. \tag{II.9}$$

If we instead consider Bhaba scattering, we find the same, and for gluon scattering in an SU(3), a factor of 9/8 enhancement — so for practical purposes the same.[1] Other choices would not give an IR enhancement, so the eventual path length before reversal is minimized by an assumption of $t-$channel gauge boson exchange. The effective cross section to have one scattering impart the necessary momentum exchange is then

$$\sigma_{\mathrm{eff}} = \int_{-4p_{\mathrm{com}}^2}^{-4p_{\mathrm{X,w}}^2} d\hat{t}\frac{d\sigma}{d\hat{t}} \simeq \frac{g^4}{16\pi\ p_{\mathrm{X,w}}^2}\,. \tag{II.10}$$

---

[1] For the Møller and gluon scattering, there is also a singularity at $\hat{u}\to 0$, which one could include by multiplying the overall effective cross section by two, but we have not done this here. The inclusion of such a factor would not make a major difference in our results.

We use this to find the rate of such scatterings in the wall frame,

$$\Gamma_{\text{wall}} = n_{\text{bath,w}} \sigma_{\text{eff}} v_{\text{rel}} \simeq \frac{\gamma g^4 g_* \zeta(3) T^3}{8\pi^3 p_{\text{X,w}}^2} \, , \tag{II.11}$$

where we have used the bath particle density in the wall frame

$$n_{\text{bath,w}} \approx \frac{\gamma g_* \zeta(3) T^3}{\pi^2} \, , \tag{II.12}$$

and $v_{\text{rel}} \simeq 2$. This result leads to an effective path length before reversal

$$l_{\text{wall}} \approx \frac{8\pi^3 p_{\text{X,w}}^2}{\gamma g^4 g_* \zeta(3) T^3} \, . \tag{II.13}$$

The path length in the plasma frame is larger by a factor of γ

$$l_{\text{plasma}} \approx \frac{8\pi^3 p_{\text{X,w}}^2}{g^4 g_* \zeta(3) T^3} \, . \tag{II.14}$$

We will eventually also study the effects of multiple soft scatters not taken into account in the above. But we first consider some other possibilities for the matrix element.

Compton scattering in fermion QED.

In the massless limit we have

$$|\mathcal{M}|^2 = -2g^4 \left(\frac{\hat{s}}{\hat{u}} + \frac{\hat{u}}{\hat{s}} \right) \, . \tag{II.15}$$

Note the divergence in the limit $\hat{u} = (p_1 - p_4)^2 \to 0$. In terms of the scattering angle, this divergence occurs when the gauge boson scatters back directly toward the wall. The divergence is cut-off by the finite fermion mass (we assume the thermal mass of the fermion is more important than any thermal mass of the U(1) gauge boson). Using $\hat{u} = 2m_f^2 - \hat{s} - \hat{t}$, we write the effective cross section as

$$\sigma_{\text{eff}} \approx \frac{1}{16\pi \hat{s}^2} \int_{-\hat{s}}^{-m_f^2} d\hat{u} |\mathcal{M}|^2 \approx \frac{g^4}{8\pi \, \hat{s}} \log \left(\frac{\hat{s}}{m_f^2} \right) \approx \frac{g^4}{32\pi^2 \gamma T p_{\text{X,w}}} \log \left(\frac{4\gamma p_{\text{X,w}}}{\frac{g^2/4\pi}{T}} \right) \, , \tag{II.16}$$

where we have assumed $m_f^2 \approx \frac{g^2}{4\pi} T^2$ and used $\hat{s} = 4\gamma T p_{\text{X,w}}$. Note the suppression compared with Eq. (II.10). The effective path length in the wall frame is then

$$l_{\text{wall}} \approx \frac{16\pi^3 p_{\text{X,w}}}{g^4 g_* \zeta(3) T^2 \log \left(\frac{4\gamma p_{\text{X,w}}}{\frac{g^2/4\pi}{T}} \right)} \, . \tag{II.17}$$

The path length in the plasma frame is therefore

$$l_{\text{plasma}} \approx \frac{\gamma 16\pi^3 p_{\text{X,w}}}{g^4 g_* \zeta(3) T^2 \log \left(\frac{4\gamma p_{\text{X,w}}}{\frac{g^2/4\pi}{T}} \right)} \, . \tag{II.18}$$

which is larger by a factor $\sim \gamma T / p_{\text{X,w}}$ than the equivalent estimate for Møller scattering.

Compton scattering in scalar QED.

In the massless limit we have

$$|\mathcal{M}|^2 = 4g^4\,, \tag{II.19}$$

and therefore

$$\sigma_{\text{eff}} \approx \frac{g^4}{4\pi\ \hat{s}}\,. \tag{II.20}$$

The effective path length in the wall frame is then

$$l_{\text{wall}} \approx \frac{8\pi^3 p_{\text{X,w}}}{g^4 g_* \zeta(3) T^2}\,. \tag{II.21}$$

The path length in the plasma frame is therefore

$$l_{\text{plasma}} \approx \frac{8\gamma\pi^3 p_{\text{X,w}}}{g^4 g_* \zeta(3) T^2}\,. \tag{II.22}$$

c) Integral method

We again begin by working in the wall frame. From the above discussion, for reversal, we need to change the initial momentum (and energy) p_1 by an $\mathcal{O}(1)$ factor in the wall frame. Using energy conservation, the change in the gauge boson momentum magnitude is

$$\delta p_{\text{X,w}} = \delta E_X = -(E_2 - E_4)\,. \tag{II.23}$$

Our first task is to find $\delta p_{\text{X,w}}$ as a function of $\hat{t}$. In the center-of-mass frame the momenta are

$$\begin{aligned}
p_1' &= (p_{\text{com}},\quad 0,\quad 0,\quad p_{\text{com}})\,, && \text{(II.24a)}\\
p_2' &= (p_{\text{com}},\quad 0,\quad 0,\quad -p_{\text{com}})\,, && \text{(II.24b)}\\
p_3' &= (p_{\text{com}},\quad 0,\quad p_{\text{com}}\sin\theta_{\text{com}},\quad p_{\text{com}}\cos\theta_{\text{com}})\,, && \text{(II.24c)}\\
p_4' &= (p_{\text{com}},\quad 0,\quad -p_{\text{com}}\sin\theta_{\text{com}},\quad -p_{\text{com}}\cos\theta_{\text{com}})\,. && \text{(II.24d)}
\end{aligned}$$

Here $\hat{s} = 4p_{\text{com}}^2 = 4\gamma T p_{\text{X,w}}$. To go from the wall frame to the center-of-mass frame requires a relativistic boost, $v_{\text{boost}} \simeq 1$, in the direction of the wall with Lorentz factor

$$\gamma_{\text{boost}} = \frac{p_{\text{com}}}{2E_1} = \frac{E_2}{2p_{\text{com}}} = \frac{1}{2}\sqrt{\frac{\gamma T}{p_{\text{X,w}}}}\,. \tag{II.25}$$

Note we have the relation between the scattering angle in the center-of-mass frame and the momentum exchange

$$\cos\theta_{\text{com}} = 1 + \frac{\hat{t}}{2p_{\text{com}}^2}\,. \tag{II.26}$$

Boosting from the center-of-mass frame back into the wall frame we have

$$E_2 = \gamma_{\text{boost}}(E_2' - v_{\text{boost}} p_{2z}') = 2\gamma_{\text{boost}} p_{\text{com}}\,, \tag{II.27a}$$

$$E_4 = \gamma_{\text{boost}}(E_4' - v_{\text{boost}} p_{4z}') = \gamma_{\text{boost}} p_{\text{com}}(1 + \cos\theta_{\text{com}}) = 2\gamma_{\text{boost}} p_{\text{com}} \left(1 + \frac{\hat{t}}{4p_{\text{com}}^2}\right)\,. \tag{II.27b}$$

Using these we find

$$\delta p_{\mathrm{X,w}} \simeq -\frac{\hat{t}}{4 p_{\mathrm{X,w}}}\,. \tag{II.28}$$

We have to be careful with the above formula, as it captures the change in the magnitude of the momentum, but we can only reverse a particle once. Thus we should cut-off the weighting for $-\hat{t} \gtrsim 4p_{\mathrm{X,w}}^2$, by making the replacement

$$\delta p_{\mathrm{X,w}} \to \mathrm{Min}\left[-\frac{\hat{t}}{4 p_{\mathrm{X,w}}},\quad p_{\mathrm{X,w}}\right], \tag{II.29}$$

in regions of phase space where such hard scatterings occur. Then the rate to lose an $\mathcal{O}(1)$ fraction of momentum in the wall frame is given by

$$\frac{1}{p_{\mathrm{X,w}}}\frac{dp_{\mathrm{X,w}}}{dt} \simeq \frac{n_{\mathrm{bath,w}} v_{\mathrm{rel}}}{p_{\mathrm{X,w}}}\int_{-4p_{\mathrm{com}}^2}^{-\mu_{\mathrm{IR}}^2} d\hat{t}\,\frac{d\sigma}{d\hat{t}}\,\delta p_{\mathrm{X,w}}\,. \tag{II.30}$$

Møller scattering.

We apply this formula to our Møller scattering cross section to find

$$\frac{1}{p_{\mathrm{X,w}}}\frac{dp_{\mathrm{X,w}}}{dt} \simeq \frac{n_{\mathrm{bath,w}} v_{\mathrm{rel}}}{p_{\mathrm{X,w}}^2}\int_{-4p_{\mathrm{com}}^2}^{-\mu_{\mathrm{IR}}^2} d\hat{t}\,\frac{g^4}{-16\pi\hat{t}} \simeq \frac{\gamma g^4 \zeta(3) g_* T^3}{8\pi^3 p_{\mathrm{X,w}}^2}\log\left(\frac{4\gamma T p_{\mathrm{X,w}}}{\mu_{\mathrm{IR}}^2}\right). \tag{II.31}$$

Assuming a thermal mass cut-off, $\mu_{\mathrm{IR}}^2 = \frac{g^2/4\pi}{T}^2$, the streaming length before reversal in the wall frame is therefore

$$l_{\mathrm{wall}} \approx \frac{8\pi^3 p_{\mathrm{X,w}}^2}{\gamma g^4 g_* \zeta(3) T^3 \log\left(\frac{4\gamma p_{\mathrm{X,w}}}{\frac{g^2/4\pi}{T}}\right)}\,. \tag{II.32}$$

This finally leads us to the streaming length in the plasma frame

$$l_{\mathrm{plasma}} \approx \frac{8\pi^3 p_{\mathrm{X,w}}^2}{g^4 g_* \zeta(3) T^3 \log\left(\frac{4\gamma p_{\mathrm{X,w}}}{\frac{g^2/4\pi}{T}}\right)}\,. \tag{II.33}$$

Note up to the logarithmic suppression factor, this is the same estimate as using the simple σ_{eff} method.

Compton scattering in fermion and scalar QED.

Here the scatterings are dominantly hard, so the use of the integral method will not change the estimates of reversal path length compared to the effective cross section approach.

d) Summary of reversal path lengths

For Møller type scattering, *i.e.* $t-$channel gauge boson exchange, we can use the path length for reversal in the plasma frame

$$\boxed{l_{\text{plasma}} \approx \frac{8\pi 3 p_{\text{X,w}}^2}{g^4 g_* \zeta(3) T^3 \log\left(\frac{\frac{4\gamma p_{\text{X,w}}}{g^2/4\pi}}{T}\right)} = \frac{8\pi^3 p_{\text{X}}^2}{\gamma^2 g^4 g_* \zeta(3) T^3 \log\left(\frac{\frac{4p_{\text{X}}}{g^2/4\pi}}{T}\right)}\,.} \tag{II.34}$$

For Compton scattering involving fermions

$$\boxed{l_{\text{plasma}} \approx \frac{16\gamma\pi^3 p_{\text{X,w}}}{g^4 g_* \zeta(3) T^2 \log\left(\frac{\frac{4\gamma p_{\text{X,w}}}{g^2/4\pi}}{T}\right)} = \frac{16\pi^3 p_{\text{X}}}{g^4 g_* \zeta(3) T^2 \log\left(\frac{\frac{4p_{\text{X}}}{g^2/4\pi}}{T}\right)}\,.} \tag{II.35}$$

And for Compton scattering involving scalars

$$\boxed{l_{\text{plasma}} \approx \frac{8\gamma\pi^3 p_{\text{X,w}}}{g^4 g_* \zeta(3) T^2} = \frac{8\pi^3 p_{\text{X}}}{g^4 g_* \zeta(3) T^2}\,.} \tag{II.36}$$

In the above, T will be later identified with the nucleation temperature T_{n}, $p_{\text{X,w}}$ is the initial gauge boson momentum in the wall frame, and we reintroduce the momentum in the plasma frame, $p_{\text{X}} = \gamma p_{\text{X,w}}$. Finally in order, say, to check whether the shells meet before particle reversal, one simply compares the above path lengths to the required propagation distances, typically $\sim R_c$ in the plasma frame.

We show the region where shell reversal effects are relevant in Fig. II.2.

II.1.2 Shell dissipation

a) Basic picture

We now consider shell dissipation. By this we mean any process which changes the momentum of shell particles by an $\mathcal{O}(1)$ factor. Note this could still leave an expanding shell with significant, albeit altered, mean momenta and particle types and number densities. In the extreme case, of course, the shell may completely dissipate leaving only a thermal bath. We shall make additional comments, in the context of specicific examples, clarifying the two possibilities when relevant below. (Similar calculations to those below, in the case of non-gauged PTs, have been used in [99].) In our calculation of the shell reversal, we were interested whether a shell propagating in front of the bubble wall would remain there, or be sent back into the bubble. Thus the primary interest was for shells of the radiated and reflected bosons of transition radiation. The shell dissipation, however, is relevant not only for the shells considered in the reversal, but also for shells formed behind the bubble wall.

b) Simple method

We work in the plasma frame and consider $2 \to 2$ scattering between a shell and bath particle. We assume the shell particles are relativistic in the plasma frame so that $E_1 \equiv$

$E_X \simeq p_x$. The initial momenta are approximately

$$p_1 = (p_{\rm X}, \quad 0, \quad 0, \quad p_{\rm X})\,, \tag{II.37a}$$

$$p_2 = (T, \quad 0, \quad 0, \quad -T)\,. \tag{II.37b}$$

The center-of-mass energy squared is $\hat{s} \simeq m_{\rm X}^2 + 4p_{\rm X}T$ and the center-of-mass momentum squared is $p_{\rm com}^2 \simeq 4p_{\rm X}^2T^2/\hat{s}$. To bring the bath particle energy from the plasma to the center-of-mass frame requires a relativistic boost in the positive $z-$direction with $v_{\rm boost} \simeq 1$ and Lorentz factor $\gamma_{\rm boost} \simeq p_{\rm com}/2T \gg 1$. Consider now a scattering between the two particles in the center-of-mass frame with a scattering angle $\theta_{\rm com}$, corresponding to Mandelstam variable $\hat{t} = -2p_{\rm com}^2(1-\cos\theta_{\rm com})$. In the center-of-mass frame the four-momenta are

$$p_1' = (p_{\rm com}, \quad 0, \quad 0, \quad p_{\rm com})\,, \tag{II.38}$$

$$p_2' = (p_{\rm com}, \quad 0, \quad 0, \quad -p_{\rm com})\,, \tag{II.39}$$

$$p_3' = (p_{\rm com}, \quad 0, \quad p_{\rm com}s_{\theta_{\rm com}}, \quad p_{\rm com}c_{\theta_{\rm com}})\,, \tag{II.40}$$

$$p_4' = (p_{\rm com}, \quad 0, \quad -p_{\rm com}s_{\theta_{\rm com}}, \quad -p_{\rm com}c_{\theta_{\rm com}})\,. \tag{II.41}$$

The change in momentum for the shell particle can be found by boosting back into the plasma frame, and is given by

$$\delta p_{\rm X} = E_3 - E_1 = -\gamma_{\rm boost}v_{\rm boost}p_{\rm com}(1-\cos\theta_{\rm com}) = \frac{\hat{t}}{4T}\,. \tag{II.42}$$

Thus to achieve $\delta p_X \approx p_X$ requires rather hard scattering $\hat{t} \approx -4Tp_{\rm X}$.

Møller scattering.

For $t-$channel gauge boson exchange processes, such as Møller scattering, we have as in our discussion for shell reversal,

$$|\mathcal{M}|^2 \approx 4g^4\frac{\hat{s}^2}{\hat{t}^2}\,. \tag{II.43}$$

and thus

$$\frac{d\sigma}{d\hat{t}} \approx \frac{g^4}{4\pi\;\hat{t}^2}\,. \tag{II.44}$$

For the hard scattering processes we are interested in for shell dissipation, we use $\hat{t} \approx -4Tp_{\rm X}$, so we take an effective cross section

$$\sigma_{\rm eff} \approx \frac{g^4}{16\pi p_{\rm X}T}\,. \tag{II.45}$$

Note the above ignores a suppression factor because the required momentum exchange is close to $\hat{s}$, nevertheless, it should give a suitable estimate up to $\mathcal{O}(1)$ factors. Remembering that we are working in the plasma frame, so that the bath number density is

$$n_{\rm bath} \approx \frac{g_*\zeta(3)T^3}{\pi^2}\,, \tag{II.46}$$

we find the scattering rate

$$\Gamma = n_{\mathrm{bath}} \sigma_{\mathrm{eff}} v_{\mathrm{rel}} = \frac{g^4 g_* \zeta(3) T^2}{8\pi^3 p_{\mathrm{X}}} \,. \tag{II.47}$$

Hence, the dissipation length in the plasma frame is

$$l_{\mathrm{plasma}} = \frac{8\pi^3 p_{\mathrm{X}}}{g^4 g_* \zeta(3) T^2} \,. \tag{II.48}$$

It is instructive to compare this to the equivalent calculation for the shell reversal path length, Eq. (II.14), in the case of radiatiated and reflected gauge bosons. Noting $p_{\mathrm{X}} = \gamma p_{\mathrm{X,w}} \approx \sqrt{g^2 2/4\pi}\gamma v_\phi$, we find the path length for dissipation is a factor $\gamma T/(\sqrt{g^2/4\pi} v_\phi)$ longer than for reversal. Note kinematics requires $\gamma > \sqrt{g^2/4\pi} v_\phi / T$ for the gauge bosons to be produced. As the large momentum change required for dissipation exceeds that momentum change required for reversal, the former would necessarily imply also the latter, so it is only self consistent to have a dissipation path length longer than or approximately coinciding with reversal.

Compton scattering in fermion QED.

The matrix element is given by

$$|\mathcal{M}|^2 = -2g^4 \left(\frac{\hat{s}}{\hat{u}} + \frac{\hat{u}}{\hat{s}} \right) \,. \tag{II.49}$$

Thus we have an effective cross

$$\sigma_{\mathrm{eff}} \approx \frac{1}{64\pi \hat{s} p_{\mathrm{com}}^2} \int_{-4p_{\mathrm{com}}^2}^{-m_f^2} d\hat{u} |\mathcal{M}|^2 \approx \frac{g^4}{32\pi p_{\mathrm{com}}^2} \log\left(\frac{4p_{\mathrm{com}}^2}{m_f^2}\right) \approx \frac{g^4 \hat{s}}{128\pi p_{\mathrm{X}}^2 T^2} \log\left(\frac{16 p_{\mathrm{X}}^2}{\frac{g^2}{4\pi}\hat{s}}\right) \,, \tag{II.50}$$

where we have assumed an IR cutoff from the fermion thermal mass $m_f^2 \approx \frac{g^2}{4\pi} T^2$, and used $p_{\mathrm{com}}^2 \simeq 4p_{\mathrm{X}}^2 T^2/\hat{s}$. Note scattering precisely at the $u-$channel singularity would correspond to replacing a shell particle of one type (say a gauge boson) with a shell particle of another type (say a fermion). This changes the nature of the shell but one may hesitate to label it as dissipation. Nevertheless, at somewhat more moderate $\hat{t}$, the size of the final state momenta are also significantly altered, so this remains a valid estimate up to logarithmic factors. The above leads to a dissipation length in the plasma frame of

$$l_{\mathrm{plasma}} = \frac{64\pi^3 p_{\mathrm{X}}^2}{g^4 g_* \zeta(3) \hat{s} T \log\left(\frac{16 p_{\mathrm{X}}^2}{\frac{g^2}{4\pi}\hat{s}}\right)} \,. \tag{II.51}$$

Again we compare with the reversal path length in the case of radiated and reflected gauge bosons, Eq. (II.18), and now find it coincides with the dissipation path length. This is due to the u-channel singularity, which means hard scatterings dominate up to teh IR cutoff in the effective particle mass. Physically this makes sense provided we treat the derived lengths as approximate up to $\mathcal{O}(1)$ factors.

Compton scattering in scalar QED.

As before, for compton scattering in massless scalar QED we have

$$|\mathcal{M}|^2 = 4g^4 \,, \tag{II.52}$$

and therefore

$$\sigma_{\text{eff}} \approx \frac{g^4}{4\pi \ \hat{s}} \,. \tag{II.53}$$

As in the fermion QED case, the scatterings of interest are dominantly hard, but there is now no $\hat{u} \to 0$ singularity which makes interpretation easier. Accordingly the dissipation path length in the plasma frame is

$$l_{\text{plasma}} = \frac{8\pi^3 p_{\text{X}}}{g^4 g_* \zeta(3) T^2} \,. \tag{II.54}$$

Making the comparison to the reversal path length in the case of radiated and reflected gauge bosons, Eq. (II.22), we find the path lengths coincide. Thus the scatterings which reverse the shell in the wall frame, also change its constituent particle momenta by $\mathcal{O}(1)$ factors in the scalar QED case.

c) Integral method

For our $2 \to 2$ scattering, we see from Eq. (II.42) that the momentum change of the shell particle in the plasma frame is given by $\delta p_{\text{X}} = -\hat{t}/4T$. To take into account the possibility of a large number of soft scatterings adding up to give a momentum change of order p_{X}, we can obtain an estimate of the path length by using an integrating, as in Eq. II.30. The only difference is that here we are working in the plasma frame. Accordingly, the momentum loss rate is given by

$$\frac{1}{p_{\text{X}}}\frac{dp_{\text{X}}}{dt} \approx \frac{n_{\text{bath}} v_{\text{rel}}}{p_{\text{X}}} \int_{-4p_{\text{com}}^2}^{-\mu_{\text{IR}}^2} d\hat{t} \frac{d\sigma}{d\hat{t}} \delta p_{\text{X}} \approx -\frac{n_{\text{bath}} v_{\text{rel}}}{4p_{\text{X}} T} \int_{-4p_{\text{com}}^2}^{-\mu_{\text{IR}}^2} d\hat{t} \frac{d\sigma}{d\hat{t}} \hat{t} \,. \tag{II.55}$$

Møller scattering.

We apply the above to $t-$channel gauge boson exchange, using , and obtain

$$\frac{d \log p_{\text{X}}}{dt} \approx \frac{g^4 \zeta(3) g_* T^2}{8\pi^3 p_{\text{X}}} \log \left(\frac{16 p_{\text{X}}^2}{\frac{g^2}{4\pi} \hat{s}} \right) \,. \tag{II.56}$$

where we have taken a thermal mass cut-off, $\mu_{\text{IR}}^2 = \frac{g^2}{4\pi} T^2$, as before. Thus the dissipation path length in the plasma frame is given by

$$l_{\text{plasma}} = \frac{8\pi^3 p_{\text{X}}}{g^4 \zeta(3) g_* T^2 \log \left(\frac{16 p_{\text{X}}^2}{\frac{g^2}{4\pi} \hat{s}} \right)} \,, \tag{II.57}$$

which is logarithmically suppressed compared to the simple estimate, Eq. II.33, and replaces it as our preferred approximation. In the case of radiated and reflected gauge boson shells, the ratio of dissipation to reversal path lengths remains the same when using the simple of integrated estimates. That is, the dissipation path length is a factor of $\gamma T/(\sqrt{g^2/4\pi}v_\phi)$ longer than the reversal path length.

Compton scattering in scalar and fermion QED.

As for the shell reversal, these dissipation path lengths are determined by hard scatterings, so the simple estimates are unchanged by use of the integral method.

d) Summary of dissipation lengths

We now summarize the dissipation path lengths due to $2 \to 2$ interactions between shell and bath particles. When the shell interacts with the bath via $t-$channel gauge boson exchange the dissipation path length in the plasma frame is approximately

$$\boxed{l_{\text{plasma}} = \frac{8\pi^3 p_{\text{X}}}{g^4\zeta(3)g_* T^2 \log\left(\frac{16p_{\text{X}}^2}{\frac{g^2}{4\pi}\hat{s}}\right)}\,,} \tag{II.58}$$

For Compton scattering with fermions

$$\boxed{l_{\text{plasma}} = \frac{64\pi^3 p_{\text{X}}^2}{g^4 g_*\zeta(3)\hat{s}T \log\left(\frac{16p_{\text{X}}^2}{\frac{g^2}{4\pi}\hat{s}}\right)}\,.} \tag{II.59}$$

And for Compton scattering with scalars

$$\boxed{l_{\text{plasma}} = \frac{8\pi^3 p_{\text{X}}}{g^4 g_*\zeta(3)T^2}\,.} \tag{II.60}$$

We remind the reader that in these expressions, p_{X} is the shell particle momentum as measured in the plasma frame, $\hat{s} \simeq 4p_{\text{X}}T$, and T is the temperature of the bath, in our scenario the nucleation temperature T_{n}.

We show the region where dissipation effects are relevant in Fig. II.3.

II.2 Fate of the bath particles

II.2.1 Basic picture

Above we checked whether the shell particles are reversed back to the wall due to their interactions with the bath. We can also ask whether bath particles reach the wall, or if they are diverted, i.e. their momentum changes by significant amounts before they reach the wall. The picture is essentially that which we considered for shell reversal. The main difference is that bath particle reversal depends on the number density of particles in the shell together with the shell thickness. The shell is created by bath particles and the volume of the shell $\propto L_p/R_c$ in the plasma frame. Thus, we have the following relation

$$n_{\text{shell}} = \frac{n_{\text{bath}}\mathcal{P}_{\text{prod}}R_c}{L_p}\,, \tag{II.61}$$

where $\mathcal{P}_{\text{prod}}$ is the probability of producing a shell particle from a bath particle. In the wall frame the shell density is reduced by a wall Lorentz factor,

$$n_{\text{shell,w}} = \frac{n_{\text{bath}}\mathcal{P}_{\text{prod}}R_c}{\gamma L_p} = \frac{n_{\text{bath}}\mathcal{P}_{\text{prod}}R_c}{L_w}\,, \tag{II.62}$$

where L_w is the shell thickness in the wall frame.

II.2.2 Simple estimates

We work in the wall frame. Consider an incoming bath particle with energy $E_a \simeq p_a \approx \gamma T$ traveling in the negative $z-$direction. This interacts with a shell particle with momentum $p_{\text{X,w}}$. The center-of-mass energy squared is $\hat{s} = 4p_{\text{X,w}}p_a = 4p_{\text{com}}^2$. Simply following the arguments which led to Eq. (II.28), we find that after a scattering the change in the bath particle energy is simply

$$\delta E_a = \frac{\hat{t}}{p_{\text{X,w}}}\,. \tag{II.63}$$

Therefore, to change the energy by $\sim E_a$, we need a single scattering to have $\hat{t} \approx -\gamma T p_{\text{X,w}}$.

Møller scattering.

Applying the above to Møller scattering type interactions, we find an effective cross section

$$\sigma_{\text{eff}} = \int_{-4p_{\text{com}}^2}^{-\gamma T p_{\text{X}}} d\hat{t}\frac{d\sigma}{d\hat{t}} \approx \frac{g^4}{16\pi\gamma T p_{\text{X,w}}}\,. \tag{II.64}$$

The effective path length of a bath particle in the wall frame is therefore

$$l_{\text{wall}} \approx \frac{8\pi p_a p_{\text{X,w}}}{g^4 n_{\text{shell,w}}}\,. \tag{II.65}$$

For the bath particles to reach the wall unimpeded we require, $l_{\text{wall}} > L_w$, *i.e.* a path length longer than the shell thickness in the wall frame. Later we will compare this to the shell reversal and dissipation conditions, but we first move on to the other interaction types.

Compton scattering with fermions.

For Compton scattering in fermion QED we have an effective cross section

$$\sigma_{\text{eff}} = \frac{1}{16\pi\hat{s}^2}\int_{-4p_{\text{com}}^2}^{-\mu_{\text{IR}}^2} d\hat{u}|\mathcal{M}|^2 \approx \frac{g^4}{32\pi p_a p_{\text{X,w}}}\log\left(\frac{4p_a p_{\text{X,w}}}{\mu_{\text{IR}}^2}\right)\,, \tag{II.66}$$

where $\mu_{\rm IR}^2$ is an IR cutoff, at least of order the fermionic thermal mass $\frac{g^2}{4\pi}T^2$. Hence we find an effective path length for a bath particle in the wall frame

$$l_{\rm wall} \approx \frac{16\pi p_a p_{\rm X,w}}{g^4 n_{\rm shell,w} \log\left(\frac{4p_a p_{\rm X,w}}{\mu_{\rm IR}^2}\right)} . \tag{II.67}$$

Compton scattering with scalars.

For Compton scattering in scalar QED we have

$$\sigma_{\rm eff} \approx \frac{g^4}{16\pi p_a p_{\rm X,w}} . \tag{II.68}$$

This gives an effective path length for the bath particle in the wall frame

$$l_{\rm wall} \approx \frac{8\pi p_a p_{\rm X,w}}{g^4 n_{\rm shell,w}} . \tag{II.69}$$

II.2.3 Integral method

Møller scattering.

Remembering the change in momentum is $\delta p_a = \hat{t}/4p_{\rm X,w}$, we can take into account multiple soft gauge boson exchanges, to find the momentum loss rate

$$\frac{d\log p_a}{dt} \approx \frac{n_{\rm shell,w} v_{\rm rel}}{p_a} \int_{-4p_{\rm com}^2}^{-\mu_{\rm IR}^2} d\hat{t} \frac{d\sigma}{d\hat{t}} \delta p_a \approx \frac{g^4 n_{\rm shell,w}}{8\pi p_a p_{\rm X,w}} \log\left(\frac{4p_a p_{\rm X,w}}{\mu_{\rm IR}^2}\right) . \tag{II.70}$$

This results in a logarithmically suppressed path length for the bath particle in the wall frame

$$l_{\rm wall} \approx \frac{8\pi p_a p_{\rm X,w}}{g^4 n_{\rm shell,w} \log\left(\frac{4p_a p_{\rm X,w}}{\mu_{\rm IR}^2}\right)} . \tag{II.71}$$

Compton scattering with scalars or fermions.

Again these are determined by hard scattering, so there is no change in our estimates using the integral method.

II.2.4 Summary

Taking the above estimates, transforming to the plasma frame to aid comparison, substituting in $\mu_{\rm IR}^2 \approx \frac{g^2}{4\pi}T^2$ and $p_a \approx \gamma T$, we find the following path lengths: For Møller scattering,

$$\boxed{l_{\rm plasma} = \frac{8\pi p_{\rm X} T}{g^4 n_{\rm shell} \log\left(\frac{4p_{\rm X}}{\frac{g^2}{4\pi}T}\right)} .} \tag{II.72}$$

For Compton scattering with fermions,

$$\boxed{l_{\text{plasma}} = \frac{16\pi p_{\text{X}} T}{g^4 n_{\text{shell}} \log\left(\frac{4p_{\text{X}}}{\frac{g^2}{4\pi}T}\right)}\,.} \tag{II.73}$$

And for Compton scattering with scalars

$$\boxed{l_{\text{plasma}} = \frac{8\pi p_{\text{X}} T}{g^4 n_{\text{shell}}}\,.} \tag{II.74}$$

The number density, $n_{\text{shell}} \propto \mathcal{P}_{\text{prod}}/L_p$. To check whether the bath enters the wall or is deflected — which would effectively shut off shell production at some earlier stage — the above path lengths should be compared with L_p. Due to the scaling of n_{shell}, however, the condition of bath deflection finally becomes independent of L_p.

We show the region where bath reversal effects are relevant in Fig. II.4.

II.2.5 Comparison to shell reversal and dissipation path lengths

We now return to our example of the radiated and reflected gauge bosons and consider the conditions for shell reversal, shell dissipation, bath reversal, and collate the results in one place. Substituting in numbers for the case of Møller scattering, avoidance of shell reversal requires

$$\frac{8\pi^3 \, \frac{g^2}{4\pi} v_\phi^2}{g^4 \zeta(3) g_* T^3 \log\left(\frac{4p_{\text{X}}}{\frac{g^2}{4\pi}T}\right)} > R_c\,. \tag{II.75}$$

Avoiding shell dissipation requires

$$\frac{8\pi^3 \gamma \sqrt{g^2/4\pi} v_\phi}{g^4 \zeta(3) g_* T^2 \log\left(\frac{4p_{\text{X}}}{\frac{g^2}{4\pi}T}\right)} > R_c\,. \tag{II.76}$$

And avoiding bath reversal requires

$$\frac{8\pi^3 \gamma \sqrt{g^2/4\pi} v_\phi}{\mathcal{P}_{\text{prod}} g^4 \zeta(3) g_* T^2 \log\left(\frac{4p_{\text{X}}}{\frac{g^2}{4\pi}T}\right)} > R_c\,. \tag{II.77}$$

Thus, as we found previously, remembering that kinematics requires $\gamma > \sqrt{g^2/4\pi} v_\phi / T$, the shell will be reversed before it is dissipated. And if we ignored the reversal back into the wall, the shell would anyway be dissipated before the bath would fail to enter the bubble. Similar conclusions hold for Compton scattering. Therein the shell reversal and dissipation are determined by hard scatterings and approximately coincide. Moreover, due to $\mathcal{P}_{\text{prod}} < 1$, the hard scatterings which reverse or dissipate the shell do not lead to bath reversal, as there are simply more bath particles than shell particles.

II.3 Phase space saturation

The particles in the shell form a dense medium. While we have never explicitly computed the phase space distribution function $f(p,T)$, we expect it to become possible larger than one at least in some parameter regions, since also the number density is larger than its equilibrium value. Having control over the phase space distribution is important as possible physical effects include Bose-Einstein condensation or processes being straight-up excluded by the Fermi exclusion principle. Additionally it is simply a necessary ingredient in the Boltzmann equation. To safely ignore these effects we investigate in this section the region where $f(p,T) < 1$.

II.3.1 Bose enhancement

The interaction Hamiltonian for the splitting process can be expressed as

$$H_{\text{int}} = \mathcal{M}_0 a_c^\dagger a_b^\dagger a_a + \text{h.c.}, \tag{II.78}$$

where a_x are the creation operators in Fock space. Then the transition amplitudes for emission and absorption read, respectively

$$\mathcal{M}_{a\to bc} = \langle f_a - 1, f_b + 1, f_c + 1 | H_{\text{int}} | f_a, f_b, f_c \rangle = \mathcal{M}_0 \sqrt{f_a}\sqrt{1 \pm f_b}\sqrt{1 + f_c}\,, \tag{II.79}$$

$$\mathcal{M}_{bc\to a} = \langle f_a + 1, f_b - 1, f_c - 1 | H_{\text{int}} | f_a, f_b, f_c \rangle = \mathcal{M}_0 \sqrt{1 \pm f_a}\sqrt{f_b}\sqrt{f_c}\,, \tag{II.80}$$

where $+/-$ refers to boson/fermion statistic. We deduce the interaction rate accounting for both emission and absorption,

$$|\mathcal{M}_{a\to bc}|^2 - |\mathcal{M}_{bc\to a}|^2 = |\mathcal{M}_0|^2 \left[f_a(1 \pm f_b) + f_c(f_a - f_b) \right] . \tag{II.81}$$

We can see that Bose-enhancement can be neglected as long as $(f_a - f_b) f_c \ll f_a$, in which case we get

$$|\mathcal{M}_{a\to bc}|^2 - |\mathcal{M}_{bc\to a}|^2 \simeq |\mathcal{M}_0|^2 f_a\,. \tag{II.82}$$

We now estimate the Bose-enhancement piece,

$$f_c(p_c)(f_a(p_a) - f_b(p_b)) = f_c(p_c)(p_a - p_b)\frac{\partial f_a}{\partial p_a}\,. \tag{II.83}$$

We now add a subscript 'p' to indicate quantities evaluated in the plasma frame. In the absence of 'p', quantities are evaluated per default in the wall frame. Assuming a Maxwell-Boltzmann momentum distribution in the plasma frame, $f_a(p_{a,p}) \propto \exp(-p_{a,p}/T_n)$, we can write

$$\frac{\partial f_a}{\partial p_a} = \frac{\partial p_{a,p}}{\partial p_a}\frac{\partial f_a}{\partial p_{a,p}} = -\frac{f_a(p_a)}{\gamma T_n}\,, \tag{II.84}$$

where we used that $p_{a,p} = \gamma p_a - \beta\gamma\sqrt{m_a^2 + p_a^2} \simeq p_a/\gamma$. Plugging equation (II.84) into equation (II.83) leads to

$$f_c(p_c)(f_a(p_a) - f_b(p_b)) = f_c(p_c) f_a(p_a) \frac{\Delta m_a^2}{2 p_a \gamma T_n}\,. \tag{II.85}$$

We exemplarily evaluate this expression for radiated reflected vector bosons. Replacing $p_a \simeq 3\gamma T_n$ and $f_a(p_a) \simeq 1$, we find

$$f_c(p_c)(f_a(p_a) - f_b(p_b)) = f_c(p_c) g^4 \frac{\log^2 (m_{c,h}/m_{c,s})}{g_*^2} \left(\frac{T_n}{T_{\rm eq}}\right)^4 \left(\frac{m_{\rm c,h}}{T_{\rm eq}}\right)^2 \left(\frac{\Delta m_a}{T_{\rm eq}}\right)^2 \left(\frac{\gamma_{\rm LL}}{\gamma}\right)^2 . \tag{II.86}$$

For strong phase transition $T_n \ll T_{\rm eq}$, we find the condition for neglecting Bose-enhancement enhancement $f_c(p_c)(f_a(p_a) - f_b(p_b)) \ll 1$ less stringent than the condition for non-perturbativity $g^2 f_c(p_c) \ll 1$ or $g^4 f_c(p_c) \ll (4\pi)^2$ discussed in the next section.

II.3.2 Perturbativity break-down

The occupation number $f_c(p_c)$ of vector bosons is related to the vector boson wave function A_μ by

$$(\partial A)^2 \sim p^2 A^2 \sim \int_{p_c} d^3p \, p \, f_c(p) \sim p_c^4 \, f_c(p_c) \, . \tag{II.87}$$

For non-abelian theory, the hierarchy between the Lagrangian terms

$$\mathcal{L} \supset \partial A \partial A + g A A \partial A + g^2 AAAA \, , \tag{II.88}$$

which is essential for perturbation theory to apply, breaks down as soon as

$$g^2 f_c(p_c) > 1 \qquad\qquad \text{(non-abelian)} \, . \tag{II.89}$$

Instead, for abelian theory, gauge bosons self-interaction terms are loop-suppressed so that perturbativity breaks down for

$$\frac{g^4}{(4\pi)^2} f_c(p_c) > 1 \qquad\qquad \text{(abelian)} \, . \tag{II.90}$$

We now proceed in calculating the phase space occupation number of radiated particles in the shells. The c particles get accumulated within a thin shell with thickness L_p. The associated number density of particles in the plasma frame is

$$n_{c,p} \;\simeq\; \mathcal{N} \, \frac{\zeta(3)}{\pi^2} g_* T_{\rm n}^3 \frac{R_c}{L_p}, \tag{II.91}$$

We deduce the occupation number f_c (number of particles per de Broglie unit)

$$f_c \;\simeq\; \frac{n_{c,p}}{k_\perp^2 p_{c,p}} \;\simeq\; \frac{\zeta(3)}{\pi^2} g_* \mathcal{N} \frac{R_c T_{\rm n}^3}{k_\perp^2 p_{c,p} L_p} \, . \tag{II.92}$$

Replacing the quantities $L_p \simeq 1/\gamma T_n$, $\mathcal{N} \simeq (\frac{g^2}{4\pi}/\pi) \log^2\left(\frac{m_{c,h}}{m_{c,s}}\right)$, $p_{c,p} \simeq 1.6\gamma m_{c,h}/\log^{1/2}\left(\frac{m_{c,h}}{m_{c,s}}\right)$ and $k_\perp \simeq 0.7 m_{c,h}/\log\left(\frac{m_{c,h}}{m_{c,s}}\right)$ for NLO reflected and $p_{c,p} \simeq 0.4\gamma m_{c,h}/\log^{1/2}\left(\frac{E_a}{m_{c,h}}\right)$ and $k_\perp \simeq 0.7 m_{c,h}/\log^{1/2}\left(\frac{m_{c,h}}{m_{c,s}}\right)$ for NLO transmitted, the occupation number of particles 'c' reads

$$f_c(p_c) = 5.3 \, \mathcal{F} \left(\frac{g_*}{100}\right)^{1/2} \left(\frac{g^2/4\pi}{0.01}\right) \left(\frac{T_{\rm eq}}{m_{c,h}}\right)^3 \left(\frac{\rm PeV}{T_{\rm eq}}\right) \left(\frac{10^2 T_n}{T_{\rm eq}}\right)^4 \left(\frac{10}{\beta/H}\right) , \tag{II.93}$$

with

$$\mathcal{F} \simeq \begin{cases} \log^{9/2}(m_{c,h}/m_{c,s}) & \text{(NLO reflected)}\,, \\ 8\log^{2}(m_{c,h}/m_{c,s})\log^{3/2}(E_a/m_{c,h}) & \text{(NLO transmitted)}\,. \end{cases} \tag{II.94}$$

Using $L_p \simeq R_c(T_n/m_{c,h})^2$, $\mathcal{N} = 1$, $p_{c,p} \simeq m_{c,h}^2/T_n$ and $k_\perp \simeq T_n$ shown in Tab. I.1, we have

$$f_c(p_c) = \zeta(3)g_s/\pi^2, \qquad \text{(LO)}. \tag{II.95}$$

We show the region where phase-space saturation effects are relevant in Fig. II.5.

II.4 Number changing interactions

While the thermal bath on its own is a system in thermal equilibrium, the particles in the shell are strongly boosted and strongly compressed. Interactions between the thermal bath and the shell, as well as interactions within the shell itself, give rise to out-of-equilibrium processes, which - if happening sufficiently fast - lead to a new state of equilibrium, different to the one from before. In this section we consider those processes that involve number changing-interactions.

In the following we will argue why 3 → 2 processes are the dominant number changing processes, we describe how to compute them, and finally state the results of our computations for a few selected processes relevant to the next chapter of this thesis. In section II.4.4 we also give a quick and easy method how to achieve a conservative estimate for any other process not explicitly computed. This also helped us to verify and understand the processes we computed explicitly.

II.4.1 Boltzmann equation

The evolution of the number density under number changing interactions is described by the integrated Boltzmann equation

$$\frac{\mathrm{d}n_1}{\mathrm{d}t} = \int \mathrm{d}\Pi_1\,\mathrm{d}\Pi_2\,\mathrm{d}\Pi_3\,\mathrm{d}\Pi_4\,\mathrm{d}\Pi_5\,(2\pi)^4\delta^{(4)}(p_1+p_2+p_5-p_3-p_4)|\mathcal{M}|^2 \tag{II.96}$$

$$\times\Big\{f_3f_4(1\pm f_1)(1\pm f_2)(1\pm f_5) - f_1f_2f_5(1\pm f_3)(1\pm f_4)\Big\}\,, \tag{II.97}$$

where

$$\mathrm{d}\Pi_i = \frac{\mathrm{d}^3p_i}{(2\pi)^3 2E_i}\,. \tag{II.98}$$

We have assumed that 3 → 2 processes give the most dominant contribution to number changing interactions, for example because others are suppressed by small couplings.

If we can neglect quantum effects, i.e. $(1\pm f_i)\simeq 1$, and the phase space integrals factorize, we can write

$$\frac{\mathrm{d}n_1}{\mathrm{d}t} \simeq \sigma_{2\to 3}\;n_3n_4 - \sigma_{3\to 2}\;n_1n_2n_5\,. \tag{II.99}$$

We are describing a coupled system of a bath in thermal equilibrium with a shell which contains particles in higher density and with more average energy. Because of the conservation of the total energy we expect the average energy per particle to go up but the number density to decrease. Therefore, we consider only the second term in Eq. (II.99), i.e. we ignore 2 → 3 processes. This can be further justified by their final phase-space suppression. As long as we stay far away from thermal equilibrium, this is a good approximation.

Considering only the annihilation term, we have

$$\frac{\mathrm{d}n_1}{\mathrm{d}t} \simeq \int \mathrm{d}\Pi_1\,\mathrm{d}\Pi_2\,\mathrm{d}\Pi_3\,\mathrm{d}\Pi_4\,\mathrm{d}\Pi_5\,(2\pi)^4\delta^{(4)}(p_1+p_2+p_5-p_3-p_4)|\mathcal{M}|^2\Big\{-f_1f_2f_5\Big\} \tag{II.100}$$

$$\simeq -\Big(\int \mathrm{d}\Pi_i\,f_i\Big)^3\int \mathrm{d}\Pi_3\,\mathrm{d}\Pi_4\,(2\pi)^4\delta^{(4)}(p_1+p_2+p_5-p_3-p_4)|\mathcal{M}|^2 \tag{II.101}$$

$$= -\left(\frac{1}{2E_i}g_i\int\frac{\mathrm{d}^3p_i}{(2\pi)^3}f_i\right)^3\times\frac{1}{32\pi^2}\int \mathrm{d}\Omega\,|\mathcal{M}|^2 \tag{II.102}$$

$$= -\frac{1}{2E_12E_22E_5}\cdot n_1n_2n_5\times\frac{1}{32\pi^2}\int \mathrm{d}\Omega\,|\mathcal{M}|^2\,, \tag{II.103}$$

where from the first to the second line we assumed that the phase space integrals factorize, and from the second to the third line we went to the center-of-mass frame, and we assumed in the simplification of the final phase space integral that all particles are massless.

Therefore the rate is given by

$$\boxed{\Gamma_{3\to2}\simeq\frac{1}{256\pi^2}\frac{n_2n_5}{E_1E_2E_5}\times\int \mathrm{d}\Omega\,|\mathcal{M}|^2\,,} \tag{II.104}$$

and one can describe number changing interactions via $\frac{\mathrm{d}n_1}{\mathrm{d}t}\simeq\Gamma_{3\to2}n_1$. Here we use the labeling of particles and momenta $p_1+p_2+p_5\to p_3+p_4$, and $\int \mathrm{d}\Omega|\mathcal{M}|^2$ is the standard expression of the final phase space integration over the spin-averaged squared matrix element in the center-of-mass frame, similar to the one of 2 → 2 scattering.

The total probability of a particle undergoing a 3 → 2 interaction before walls collide is

$$\mathcal{P}_{3\to2}\simeq\Gamma_{3\to2}\times L_{\mathrm{eff}}\,, \tag{II.105}$$

where $\Gamma_{3\to2}$ is the interaction rate and L_{eff} is the effective distance (or equivalently time, because particles are ultra-relativistic) it takes the shell particle to travel until collision with a neighbouring bubble. Note that bath particles are affected by these interactions only for the short times that they are transversed by the shells.

II.4.2 Thermal field theory

Integrating over the final phase space confronts us with the problem that the amplitudes are collinear divergent. This is unphysical however, since interactions with the thermal plasma screen the long-range forces. The collinear divergence is going to be regulated by the Debye mass, given in Eq. (II.115). In the following we recap the proper procedure on correctly implementing the Debye mass in the mathematical expression for the amplitudes. We continue with presenting the results of the computation of number changing interactions in Sec. II.4.3.

a) Vacuum gauge theories

In $R\xi$-gauges the free gluon propagator is given by

$$D_{\mu\nu}(K)=\frac{1}{K^2}\left[-g_{\mu\nu}+(1-\xi)\frac{K_\mu K_\nu}{K^2}\right]. \tag{II.106}$$

The propagator $D_{\mu\nu}$ is constructed out of Lorentz-covariant objects, here the metric and the momentum 4-vector.

The spin-polarization sum is given by

$$\sum_{\lambda=\pm1} \epsilon_\mu(k,\lambda)\epsilon_\nu^*(k,\lambda) = -g_{\mu\nu} + \frac{k_\mu n_\nu + k_\nu n_\mu}{k\cdot n} - \frac{n_\mu n_\nu}{(k\cdot n)^2}\,, \tag{II.107}$$

where n_μ is a linearly independent reference vector with norm $n^2 = 1$.

The interpretation of this equation is that the four 4-vectors ϵ_μ^+, ϵ_μ^-, k_μ, and n_μ form a basis, and above equation is the completeness relation. For massive spin-1 particles there exists a third longitudinal polarization vector ϵ_μ^L, therefore n_μ in that case is not needed to have a complete basis.

The Ward identity $\mathcal{M}_\mu k^\mu = 0$ implies that for QED only the first term $-g_{\mu\nu}$ survives. However, even for QCD we know that the amplitude must be independent of n_μ, since n_μ is a reference vector and does not transform under Lorentz transformations.

b) Thermal gauge theories

In thermal field theory we have another 4-vector given by the 4-velocity of the plasma frame u_μ ($u^2 = 1$). The implications have been derived in [113]. We will recapitulate the importing points here.

Consider the general decomposition of the non-Abelian self energy

$$\Pi_{\mu\nu} = \Pi_T A_{\mu\nu} + \Pi_L B_{\mu\nu} + \Pi_C C_{\mu\nu} + \Pi_D D_{\mu\nu}\,, \tag{II.108}$$

where $A_{\mu\nu}$, etc. are basis tensors constructed out of k_μ and u_μ, see [113]. The coefficients Π_i have to be computed and can be in general momentum and gauge-dependent. This gives the full propagator

$$D'_{\mu\nu} = -\frac{A_{\mu\nu}}{k^2-\Pi_T} + \frac{\tilde{k}_\mu\tilde{k}_\nu}{k^2(k^2-\Pi_L)} - \xi\frac{H_\mu H_\nu}{(k^2)^2(k^2-\Pi_L)}\,, \tag{II.109}$$

where

$$\tilde{k}_\mu = \frac{k\cdot u\; k_\mu - k^2 u_\mu}{\sqrt{(k\cdot u)^2 - k^2}}\,, \tag{II.110}$$

$$H_\mu = \sqrt{k^2-\Pi_L}\; k_\mu + \sigma\sqrt{\Pi_D}\;\tilde{k}_\mu\,, \quad \sigma = \pm1\,. \tag{II.111}$$

The $\sigma = \pm1$ arises due to solving the self-consistency condition

$$(\Pi_C)^2 = \Big(k^2 - \Pi_L\Big)\Pi_D\,. \tag{II.112}$$

Since it has been computed that $\Pi_C = \mathcal{O}(g^2)$, this immediately implies that we have at least $\Pi_D = \mathcal{O}(g^4)$. We can therefore neglect it in any tree-level computation as a higher-order effect.

The surviving pieces in $H_\mu H_\nu$ are proportional to $k_\mu k_\nu$ and cancel due to the structure of non-Abelian gauge theories. Therefore, the resulting amplitude does not depend on the gauge fixing parameter ξ.

The only relevant coefficients of the self energy are therefore the transverse part Π_T and the longitudinal part Π_L. They have been computed in the literature [114, 115], and are given at leading order by

$$\Pi_T(k) = \frac{\mu^2}{2}\left[\frac{(k^0)^2}{|\vec{k}|^2} + \frac{k^0}{2|\vec{k}|}\left(1 - \frac{(k^0)^2}{|\vec{k}|^2}\right)\ln\frac{k^0 + |\vec{k}| + i\eta}{k^0 - |\vec{k}| + i\eta}\right], \tag{II.113}$$

$$\Pi_L(k) = \mu^2\left(1 - \frac{(k^0)^2}{|\vec{k}|^2}\right)\left[1 - \frac{k^0}{2|\vec{k}|}\ln\frac{k^0 + |\vec{k}| + i\eta}{k^0 - |\vec{k}| + i\eta}\right], \tag{II.114}$$

where the Debye mass μ is given by

$$\mu^2 = 2g_{\text{eff}}g^2\int\frac{\mathrm{d}^3p}{(2\pi)^3}\,\frac{f(p,T)}{p^0}\,. \tag{II.115}$$

In case of an equilibrium thermal distribution $f(p,T)$ this reproduces the well-known result $\mu^2 \simeq g^2T^2(N_c/3 + N_f/6)$, see e.g. [114]. In case the shell's particles feel the interaction, e.g. as in the case of shells formed by non-abelian gauge bosons, then Eq.(II.115) implies an additional contribution to μ^2 coming from shell particles, which can dominate the standard one.

We are only interested in the behavior of the self energies around the collinear singularity, i.e. for $|\vec{k}| \to k^0$. Away from this region the scalar products will become larger, and the effect of the Debye mass will become subdominant. Around the singularity we can approximate the self-energies by a constant,

$$\Pi_T \equiv \lim_{|\vec{k}|\to k^0}\Pi_T(k) = \frac{\mu^2}{2}\,, \tag{II.116}$$

$$\Pi_L \equiv \lim_{|\vec{k}|\to k^0}\Pi_L(k) = 0\,. \tag{II.117}$$

We find that the longitudinal part of the self-energy vanishes in this limit, and in fact we find that it is not needed in order to regulate the collinear divergence. For this purpose, the transverse part Π_T is sufficient.

The spin-polarization sum can be constructed in the same way as it is usually done in vacuum QFT, i.e. by making in ansatz with all possible Lorentz structures and fixing the coefficients by requiring transversality with respect to momentum and plasma 4-velocity. We find

$$\sum_{\lambda=\pm1}\epsilon_\mu(k,\lambda)\epsilon^*_\nu(k,\lambda) = -g_{\mu\nu} - \frac{k_\mu k_\nu}{(k\cdot u)^2 - k^2} + \frac{k\cdot u}{(k\cdot u)^2 - k^2}(k_\mu u_\nu + u_\mu k_\nu) - \frac{k^2\,u_\mu u_\nu}{(k\cdot u)^2 - k^2}\,. \tag{II.118}$$

Note that we only have two polarizations and $k^2 = m^2_{\text{vac}}$, since the quantum state is defined at infinity where it doesn't feel any effect of traveling trough a thermal plasma. Therefore, Eq. (II.118) is in fact equal to the spin-polarization sum of vacuum QFT in E. II.107, which can be seen by shifting $u_\mu = \alpha k_\mu + \beta n_\mu$.

However, the interpretation of the two vectors, n_μ and u_μ, is different. In vacuum the vector n_ν is a reference vector which does not transform under Lorentz transformations, and we could therefore argue that the whole amplitude must be independent of it. In thermal field theory the vector u_μ describes the rest frame of the plasma, i.e. it is a real physical effect, and therefore in general the amplitude is going to be dependent on the plasma velocity u_μ. However, the leading order, that is keeping only thermal masses in the denominators and not in the numerator, must have a smooth limit to the vacuum amplitude. This implies that the leading order will not depend on the plasma velocity.

In vacuum QED one is allowed to drop all terms except $-g_{\mu\nu}$ because of the Ward identity. In thermal field theory, this is in general not allowed, except for example in the hard thermal loop (HTL) approximation [116], where the Ward-identity is recovered.

For example, the spin-averaged squared matrix element for $gg \to gg$ scattering (for simplicity we only take a $2 \to 2$ process) is given by

$$|\mathcal{M}|^2 \propto \frac{\left(s^2+st+t^2\right)^3}{\left(s+\Pi_T\right)^2\left(t-\Pi_T\right)^2\left(u-\Pi_T\right)^2}\,, \tag{II.119}$$

where s, t, u are the Mandelstam variables. We find that for $\Pi_T \to 0$ we recover the vaccum QFT result. Computing this result, which has been done with the help of FeynRules [117], FeynArts [118], and FeynCalc [119–121], there were terms in the numerator proportional to Π_T and u_μ. However, these are $\mathcal{O}(g^2)$, and if we would want to include them, we would have also to compute the 1-loop correction to the amplitude. The small coupling expansion of the Π_T in the denominator can only be done after performing the final phase space integration, as Π_T is needed to regulate the integral.

Note the following limits. If we take the regulator to zero, we recover the collinear singularity; if we take the regulator to infinity, the amplitude vanishes. Physically, this happens because the Debye mass function as a regulator scales with the phase space distribution function of the medium. For an infinitely dense medium all interactions with other particles are completely screened by the medium and therefore the probability of an interaction becomes zero. The limit of vanishing Debye mass corresponds to no medium, and therefore we have the same singularity as in vacuum QFT. Since it is reasonable to assume that the dependence of the amplitude on the Debye mass is well-behaved, in particular monotonic, between the two extremes, we find that smaller masses give larger probabilities. Therefore, since the thermal mass is at least $\mu \gtrsim gT$, we can compute an upper limit on the probability, valid for all processes, independent of what medium they are interacting with.

II.4.3 Results for the $3 \to 2$ interactions

We present here the results obtained after integrating over the final phase space as described in appendix A. We compute $\int d\Omega|\mathcal{M}|^2$ for all possible $3 \to 2$ processes involving in the initial state at least one gauge boson V and one fermion and/or one scalar charged under the gauge group, where for completeness in the scalar case we included the self-coupling $\mathcal{L} \supset \lambda|\phi|^4$ in addition to the scalar gauge coupling to V. We perform these computations for the cases of both an Abelian and a non-Abelian gauge symmetry, which for concreteness we take as U(1) and SU(N), because the self-interactions of the vectors eventually lead to important differences between the two.

We now report our results for $\int d\Omega|\mathcal{M}|^2$, in terms of scalar products of the 4-momenta in the center-of-mass frame $p_1 + p_2 + p_5 = p_3 + p_4$, including for simplicity only the terms that are leading order in $p_i \cdot p_j/\mu^2$. In case at least one initial particle belongs to the bath, we anticipate that one has the hierarchy $\mu^2 \ll p_1 \cdot p_2 \ll p_1 \cdot p_5 \simeq p_2 \cdot p_5$, leading to the expansions reported in tables II.2 (case of one fermion charged under the gauge group), II.3 (case of one scalar charged under the gauge group), II.4 (case of both a fermion and a scalar charged under the gauge group). In case all initial particles belong to the shell, then all scalar products are of the same order, leading to the leading-order results in Table II.5.

Depending on the identity of the initial-state scatterers, the scalar products have a different dependence on the parameters of the PT and of the theory, implying different results for the probability that the associated $3 \to 2$ interaction happens before collision, which is the question of our interest. We therefore now turn to derive expression for the scalar products in terms of the parameters of the theory. The presented results require as input parameters the scalar products specific to the model, which we present in Tab. II.1 and whose derivation we explain next. We show the region where number changing interactions are relevant in Fig. II.6.

Channel	Abelian U(1)	non-Abelian SU(3)
Leading-order interaction	$\mu^2 \sim g^2 T_\mathrm{n}^2$	$\mu^2 \sim g^2 T_\mathrm{n}^2 + g^2 n_V / \langle E_\mathrm{LO} \rangle$
particles acquiring	$p_1 \cdot p_2 \sim p_i p_j \sim T_\mathrm{n}^2$	
a mass[95, 101]	$p_1 \cdot p_5 \cdot \gamma T_\mathrm{n} E_\mathrm{LO}$	
Gauge interaction $g \ll 4\pi$:	$\mu^2 \sim g^2 T_\mathrm{n}^2$	$\mu^2 \sim g^2 T_\mathrm{n}^2 + g^2 n_V / \langle E_\mathrm{R,T} \rangle$
bremsstrahlung radiation	$p_1 \cdot p_2\big\vert_\mathrm{bss} \sim p_i p_j \sim T_\mathrm{n}^2 + m_{c,h}^2$	
reflected (R), transmitted (T)	$p_1 \cdot p_2\big\vert_\mathrm{bbs} \sim T_\mathrm{n}^2$	
[89, 96–98]	$p_1 \cdot p_5 \cdot \gamma T_\mathrm{n} E_\mathrm{R,T}$	

Table II.1: Expressions for scalar products and infrared cutoff μ as explained in Sec. a) and Sec. b). The indices 'bss' and 'bbs' stand for bath-shell-shell and bath-bath-shell. The scalar products for these two cases can be different because two particles from the shell do not have to be as collimated as two particles from the bath, depending on whether the production mechanism at the wall conserves orientation.

a) Bath-shell-shell and bath-bath-shell

For the interactions between shell and bath particles we use the results from tables II.2, II.3, II.4. These expression are valid in case there is a hierarchy $\mu^2 \ll p_1 \cdot p_2 \ll p_1 \cdot p_5 \simeq p_2 \cdot p_5$, which we now justify. Here p_1 and p_2 are nearly parallel, i.e. they either both belong to the bath or both belong to the shell. In particular for bath-shell-shell interactions we have p_1 and p_2 for the shell particles and p_5 for the bath particle; for bath-bath-shell interactions we have p_1 and p_2 for the bath particle and p_5 for the shell particle. Since p_1 and p_2 are nearly parallel, their scalar product does not feel the large energies that they can have in some frame. On the other hand, since p_5 tracks a different population than p_1 and p_2, the scalar products $p_1 \cdot p_5$ and $p_2 \cdot p_5$ will be of the same order and much larger than $p_1 \cdot p_2$.

For L_{eff} in Eq. (II.105) one chooses the appropriate expression: a particle from the bath scattering with shell particles only finds other shell particles while it passes through the shell, therefore L_{eff} is the effective thickness of the shell; a particle from the shell can scatter with the bath and other shell particles during its whole travel time, therefore L_{eff} is the radius of the bubble.

Note that by a careful investigation (see Sec. B) of just the scattering kinematics it is straightforward to show that the two final state particles are of one type shell and one type bath, i.e. one particle has the typical energy (up to $\mathcal{O}(1)$-factors) of a bath particle and is traveling inside the bubble, and the other particle has the typical energy of an ejected particle and is traveling along with other shell particles.

b) Shell-shell-shell

For the interactions between shell and bath particles we use the results from table II.5. These expression are valid in case there is a hierarchy $\mu^2 \ll p_i \cdot p_j \simeq p_1 \cdot p_2 \simeq p_1 \cdot p_5 \simeq p_2 \cdot p_5$. The expectation value of the scalar product is the typical spread of the particles in the shell, i.e. a measure how perpendicular to the wall they are ejected.

The effective length L_{eff} is given by the radius of the bubble, since shell particles can find each other all the time until collision.

We now present all amplitudes of emitted vectors interacting with fermions and scalars, where the vectors are either gauge under abelian U(1) or non-Abelian SU(N), in the tables II.2, II.3, II.4, II.5.

$a(p_1)\ b(p_2)\ c(p_5)$ $\to XY$	$\int \mathrm{d}\Omega \lvert\mathcal{M}\rvert^2$: $\mathcal{G}_V = \mathrm{U}(1)$ $\int \mathrm{d}\Omega \lvert\mathcal{M}\rvert^2$: $\mathcal{G}_V = \mathrm{SU}(N)$
$VVV \to f\bar{f}$	$g^6\ \frac{48\pi\left(2\ln\left(\frac{p_1\cdot p_2}{\mu^2}\right)+5\ln 2\right)}{p_1\cdot p_2}$ $g^6\ \frac{\pi}{N^2(N^2-1)^2}\frac{1}{p_1\cdot p_2}\left[9N^2(N^2-1)\ln\left(\frac{p_1\cdot p_5}{\mu^2}\right)+2(N^4-7N^2+6)\ln\left(\frac{p_1\cdot p_2}{\mu^2}\right) +N^4(21\ln 2-15)+N^2(9-51\ln 2)+30\ln 2\right]$
$VVf \to Vf$ $VV\bar{f} \to V\bar{f}$	$g^6\ \frac{24\pi\left(2\ln\left(\frac{p_1\cdot p_2}{\mu^2}\right)+5\ln 2\right)}{p_1\cdot p_2}$ $g^6\ \frac{N^2}{N^2-1}\frac{36\pi\ p_1\cdot p_5\left(5\ln\left(\frac{p_1\cdot p_2}{\mu^2}\right)+6\ln 2\right)}{\left(p_1\cdot p_2\right)^2}$
$f\bar{f}V \to VV$	$g^6\ \frac{32\pi\left(\ln\left(\frac{p_1\cdot p_2}{\mu^2}\right)+3\ln 2\right)}{p_1\cdot p_5}$ $g^6\ \frac{8\pi\ p_1\cdot p_5\left((2N^2-3)\ln\left(\frac{p_1\cdot p_2}{\mu^2}\right)+3(N^2-1)\ln 2\right)}{\left(p_1\cdot p_2\right)^2}$
$f\bar{f}V \to f\bar{f}$	$g^6\ \frac{4\pi\left(\ln\left(\frac{p_1\cdot p_5}{\mu^2}\right)+18\ln\left(\frac{p_1\cdot p_2}{\mu^2}\right)-1+29\ln 2\right)}{p_1\cdot p_2}$ $g^6\ \frac{\pi}{6N^2}\frac{1}{p_1\cdot p_2}\left[3N(N^2-1)\ln\left(\frac{p_1\cdot p_5}{\mu^2}\right)+6(10N^3+N^2-10N-1)\ln\left(\frac{p_1\cdot p_2}{\mu^2}\right) +N^3(99\ln 2-5)+12N^2\ln 2+N(3-99\ln 2)-12\ln 2\right]$
$ffV \to ff$ $\bar{f}\bar{f}V \to \bar{f}\bar{f}$	$g^6\ \frac{16\pi\left(14\ln\left(\frac{p_1\cdot p_2}{\mu^2}\right)+15\ln 2\right)}{p_1\cdot p_2}$ $g^6\ \frac{N^2-1}{N^2}\frac{\pi\left(4(5N-2)\ln\left(\frac{p_1\cdot p_2}{\mu^2}\right)+30N\ln 2\right)}{p_1\cdot p_2}$
$VfV \to Vf$ $V\bar{f}V \to V\bar{f}$	$g^6\ \frac{\pi\left(10\ln\left(\frac{p_1\cdot p_5}{\mu^2}\right)+4\ln\left(\frac{p_1\cdot p_2}{\mu^2}\right)+5+34\ln 2\right)}{p_1\cdot p_2}$ $g^6\ \frac{1}{N^2-1}\frac{10\pi\ p_1\cdot p_5\left(2(4N^2-1)\ln\left(\frac{p_1\cdot p_2}{\mu^2}\right)+3(3N^2-1)\ln 2\right)}{\left(p_1\cdot p_2\right)^2}$

Table II.2: Results of our computations for scatterings involving vectors and fermions. For a more detailed explanation, see Sec. II.4.3.

$a(p_1)\ b(p_2)\ c(p_5)$ $\to XY$	$\int \mathrm{d}\Omega \lvert\mathcal{M}\rvert^2$: $\mathcal{G}_V = \mathrm{U}(1)$ $\int \mathrm{d}\Omega \lvert\mathcal{M}\rvert^2$: $\mathcal{G}_V = \mathrm{SU}(N)$
$VVV \to \phi\bar{\phi}$	$g^6\ \frac{8\pi\left(9\ln\left(\frac{p_1\cdot p_5}{\mu^2}\right)+11\ln 2\right)}{p_1\cdot p_5}$ $g^6\ \frac{2N^2-3}{2(N^2-1)^2}\frac{3\pi}{p_1\cdot p_2}$
$VV\phi \to V\phi$ $VV\bar{\phi} \to V\bar{\phi}$	$g^6\ \frac{4\pi\left(9\ln\left(\frac{p_1\cdot p_5}{\mu^2}\right)-9+11\ln 2\right)}{p_1\cdot p_5}$ $g^6\ \frac{\pi\ p_1\cdot p_5}{N^2-1}\frac{8(4N^2-1)\ln\left(\frac{p_1\cdot p_2}{\mu^2}\right)+12(3N^2-1)\ln 2}{\left(p_1\cdot p_2\right)^2}$
$\phi\bar{\phi}V \to VV$	$g^6\ \frac{16\pi\left(\ln\left(\frac{p_1\cdot p_2}{\mu^2}\right)+3\ln 2\right)}{p_1\cdot p_5}$ $g^6\ \pi\ p_1\cdot p_5\ \frac{4(2N^2-3)\ln\left(\frac{p_1\cdot p_2}{\mu^2}\right)+12(N^2-1)\ln 2}{\left(p_1\cdot p_2\right)^2}$
$\phi\bar{\phi}V \to \phi\bar{\phi}$	$g^6\ \frac{\pi}{p_1\cdot p_2}$ $g^6\ \frac{2N^2-3}{24N}\frac{\pi}{p_1\cdot p_2}$
$\phi\phi V \to \phi\phi$ $\bar{\phi}\bar{\phi}V \to \bar{\phi}\bar{\phi}$	$g^6\ \frac{96\pi\left(\ln\left(\frac{p_1\cdot p_2}{\mu^2}\right)+\ln 2\right)}{p_1\cdot p_5}$ $\frac{\pi}{4N^2}\frac{1}{p_1\cdot p_5}\left[\begin{array}{c}(N+1)(4\lambda g^4N+g^6(N-1))\ln\left(\frac{p_1\cdot p_5}{\mu^2}\right)\\ -8(N^2-1)(4\lambda g^4N-g^6(3N^2-1))\ln\left(\frac{p_1\cdot p_2}{\mu^2}\right)\\ +16\lambda^2g^2\left(N^3(3\ln 2-1)+N^2(3\ln 2-2)\right)\\ -8\lambda g^4\left(N^3(5\ln 2+1)+N^2-N(5\ln 2+2)\right)\\ +g^6\left(N^3(35\ln 2-1)+13N^2\ln 2-N(35\ln 2-3)-13\ln 2-2\right)\end{array}\right]$
$V\phi V \to V\phi$ $V\bar{\phi}V \to V\bar{\phi}$	$g^6\ \frac{8\pi}{p_1\cdot p_2}$ $g^6\ \frac{\pi\ p_1\cdot p_5}{N^2-1}\frac{8(4N^2-1)\ln\left(\frac{p_1\cdot p_2}{\mu^2}\right)+12(3N^2-1)\ln 2}{\left(p_1\cdot p_2\right)^2}$

Table II.3: Results of our computations for scatterings involving vectors and scalars. For a more detailed explanation, see Sec. II.4.3.

$a(p_1)\ b(p_2)\ c(p_5)$ $\to XY$	$\int \mathrm{d}\Omega \lvert\mathcal{M}\rvert^2$: $\mathcal{G}_V = \mathrm{U}(1)$ $\int \mathrm{d}\Omega \lvert\mathcal{M}\rvert^2$: $\mathcal{G}_V = \mathrm{SU}(N)$
$\phi\bar{\phi}V \to f\bar{f}$	$g^6\ \frac{2\pi\left(\ln\left(\frac{p_1\cdot p_5}{\mu^2}\right)+3\ln 2-1\right)}{p_1\cdot p_2}$ $g^6\ \frac{\pi}{12N}\frac{3(N^2-1)\ln\left(\frac{p_1\cdot p_5}{\mu^2}\right)+9(N^2-1)\ln 2-5N^2+3}{p_1\cdot p_2}$
$f\bar{f}V \to \phi\bar{\phi}$	$g^6\ \frac{2\pi}{p_1\cdot p_2}$ $g^6\ \frac{2N^2-3}{12N}\frac{\pi}{p_1\cdot p_2}$
$\phi f V \to \phi f$ $\bar{\phi}\bar{f}V \to \bar{\phi}\bar{f}$	$g^6\ \frac{8\pi\left(2\ln\left(\frac{p_1\cdot p_2}{\mu^2}\right)+3\ln 2\right)}{p_1\cdot p_2}$ $g^6\ \frac{N^2-1}{N}\frac{\pi\left(2\ln\left(\frac{p_1\cdot p_2}{\mu^2}\right)+3\ln 2\right)}{p_1\cdot p_2}$
$\phi\bar{f}V \to \phi\bar{f}$ $\bar{\phi}fV \to \bar{\phi}f$	$g^6\ \frac{8\pi\left(2\ln\left(\frac{p_1\cdot p_2}{\mu^2}\right)+3\ln 2\right)}{p_1\cdot p_2}$ $g^6\ \frac{N^2-1}{N}\frac{\pi\left(2\ln\left(\frac{p_1\cdot p_2}{\mu^2}\right)+3\ln 2\right)}{p_1\cdot p_2}$
$VVV \to VV$	0 $g^6\ \frac{N^3}{(N^2-1)^2}\frac{144\pi\ p_1\cdot p_5\left(5\ln\left(\frac{p_1\cdot p_2}{\mu^2}\right)+6\ln 2\right)}{\left(p_1\cdot p_2\right)^2}$

Table II.4: Results of our computations for scatterings involving vectors, fermions, and scalars. For a more detailed explanation, see Sec. II.4.3.

$a(p_i)\ b(p_j)\ c(p_k)$ $\to XY$	$\int \mathrm{d}\Omega\lvert\mathcal{M}\rvert^2$: $\mathcal{G}_V = \mathrm{U}(1)$ $\int \mathrm{d}\Omega\lvert\mathcal{M}\rvert^2$: $\mathcal{G}_V = \mathrm{SU}(N)$
$VVV \to f\bar{f}$	$g^6\ \frac{24\pi\left(5\ln\left(\frac{p_i\cdot p_j}{\mu^2}\right)+5\ln 3-\ln 2\right)}{p_i\cdot p_j}$ $g^6\ \frac{\pi}{2N^2(N^2-1)^2}\frac{1}{p_i\cdot p_j}\left[\begin{array}{c} 15(N^4-3N^2+2)\ln\left(\frac{p_i\cdot p_j}{\mu^2}\right) \\ +N^4(29\ln 2-3)+N^2(-9+105\ln 2-90\ln 3)+24\ln 3-6\ln 2\end{array}\right]$
$VVV \to \phi\bar{\phi}$	$g^6\ \frac{36\pi\left(\ln\left(\frac{p_i\cdot p_j}{\mu^2}\right)+3\ln 2-\ln 3\right)}{p_i\cdot p_j}$ $g^6\ \frac{\pi}{4N^2(N^2-1)^2}\frac{1}{p_i\cdot p_j}\left[\begin{array}{c} 9(N^4-3N^2+2)\ln\left(\frac{p_i\cdot p_j}{\mu^2}\right) \\ +N^4(3+11\ln 2)+N^2(9-129\ln 2+54\ln 3)-18\ln 3+54\ln 2\end{array}\right]$
$VVV \to VV$	0 $g^6\ \frac{N^3}{(N^2-1)^2}\frac{2\pi\left(1323\ln\left(\frac{p_i\cdot p_j}{\mu^2}\right)-3-396\ln 3+1987\ln 2\right)}{p_i\cdot p_j}$

Table II.5: Results of our computations for self-thermalization within the shell. For a more detailed explanation, see Sec. II.4.3.

II.4.4 An estimate on number changing interactions

In this section we give useful formulae to estimate an upper limit on the integrated spin-averaged squared matrix element, without actually having to compute the amplitude and performing the final phase space integration. In general, these estimates are very conservative and one gains a lot of free parameter space by actually computing the amplitude. This estimate can then serve as a guidance on the computation of new amplitudes.

a) Equilibration between bath and shell

Assume that we have a sizeable spread of particles, i.e. $p_1 \cdot p_2 \gtrsim \mu^2$.

We take the following basis

$$p_{1,com} = \begin{pmatrix} p_I \\ 0 \\ 0 \\ p_I \end{pmatrix} \,,\ p_{2,com} = \begin{pmatrix} p_J \\ p_J\sin(\theta_{12}) \\ 0 \\ p_J\cos(\theta_{12}) \end{pmatrix} \,,\ p_{3,com} = \begin{pmatrix} \sqrt{p_I^2 + 2p_I p_J\cos(\theta_{12}) + p_J^2} \\ -p_J\sin(\theta_{1,2}) \\ 0 \\ -p_I - p_J\cos(\theta_{12}) \end{pmatrix} \,, \tag{II.120}$$

$$p_{4,com} = \begin{pmatrix} p_F \\ p_F\sin(\theta_{13})\cos(\varphi_{13}) \\ p_F\sin(\theta_{13})\sin(\varphi_{13}) \\ p_F\cos(\theta_{13}) \end{pmatrix} \,,\ p_{5,com} = \begin{pmatrix} p_F \\ -p_F\sin(\theta_{13})\cos(\varphi_{13}) \\ -p_F\sin(\theta_{13})\sin(\varphi_{13}) \\ -p_F\cos(\theta_{13})\,, \end{pmatrix} \tag{II.121}$$

which is the one from appendix A, with all particles massless. It is helpful to define

$$p_{IJ} = \sqrt{p_I^2 + 2p_I p_J\cos(\theta_{12}) + p_J^2} \geq 0\,, \tag{II.122}$$

sucht that energy conservation implies

$$2p_F = p_I + p_J + p_{IJ} \,. \tag{II.123}$$

We find these scalar products,

$$p_1 \cdot p_5 = \frac{1}{2}\Big[(p_I + p_{IJ})^2 - p_J^2\Big] \tag{II.124}$$

$$p_2 \cdot p_5 = \frac{1}{2}\Big[(p_J + p_{IJ})^2 - p_I^2\Big] \tag{II.125}$$

$$p_1 \cdot p_2 = \frac{1}{2}\Big[(p_I + p_J)^2 - p_{IJ}^2\Big] \tag{II.126}$$

Note, that two scalar products are the same if the two associated energies are the same, i.e. $p_1 \cdot p_5 = p_2 \cdot p_5$ if $p_I = p_J$.

We do not look at interference terms, since they cannot be more divergent than a single diagram squared. We have the principal form of the spin-averaged squared amplitude,

$$|\mathcal{M}|^2 = g^6 \sum \frac{\prod s_{mn}}{(s_{ij} - \mu)^a (s_{kl} - \mu)^b} \,. \tag{II.127}$$

One case is given by

$$|\mathcal{M}|^2 \supset \frac{1}{(s_{13} - \mu^2)^a (s_{45} - \mu^2)^b} \,, \tag{II.128}$$

where if $p_1 \parallel p_2$, then also $p_1 \parallel p_5$, and both denominators become divergent at the same time. Since they are thermally distributed, this is not exactly the case, so they diverge at different integration regions. Therefore we find the suppression by the regulator (thermal mass) to be at maximum

$$\left(\mu^2\right)^{-2+1} \,. \tag{II.129}$$

We also have

$$|\mathcal{M}|^2 \supset \frac{1}{(s_{12} - \mu^2)^a (s_{45} - \mu^2)^b} \,, \tag{II.130}$$

which after integrating scales at worst like

$$\frac{1}{(p_1 \cdot p_2)^2} \left(\mu^2\right)^{-2+1} \,. \tag{II.131}$$

Therefore we find

$$\int \mathrm{d}\Omega \, |\mathcal{M}|^2 \simeq g^6 \frac{1}{p_1 \cdot p_5} \left(\frac{p_1 \cdot p_5}{p_1 \cdot p_2}\right)^k \left(\frac{p_1 \cdot p_5}{\mu^2}\right)^l \,, \qquad k \leq 2 \,,\; l \leq 1 \,. \tag{II.132}$$

Here we inserted the only leftover scale $p_1 \cdot p_5$ to fix the correct mass dimension, which is conservative from the point of view of finding an upper limit on the amplitude squared. We also neglected any appearances of logarithms of scalar products, since they are not much larger than $\mathcal{O}(1)$ factors.

Comparing Eq. (II.132) to the calculated processes in tables II.2, II.3, II.4, we find that we do not always have maximal divergence with $k = 2$, $l = 1$. This is due to cancellations at amplitude level depending on the specific physical process.

b) Equilibration within the shell

For equilibration within the shell itself consider the following momentum basis,

$$p_{1,com} \simeq p_{2,com} \simeq p_{5,com} \simeq \begin{pmatrix} \mu \\ 0 \\ 0 \\ 0 \end{pmatrix}, \tag{II.133}$$

$$p_{3,com} = \begin{pmatrix} p_f \\ p_f \sin(\theta_{13}) \\ 0 \\ p_f \cos(\theta_{13}) \end{pmatrix}, \quad p_{4,com} = \begin{pmatrix} p_f \\ -p_f \sin(\theta_{13}) \\ 0 \\ -p_f \cos(\theta_{13}) \end{pmatrix}, \tag{II.134}$$

sucht that $p_f = \frac{3}{2}\mu$. This holds under the assumption that the spread is small, which implies that in the center-of-mass frame each initial particle is approximately at rest with sub-leading momentum component.

Then we find

$$p_1 \cdot p_2 \simeq p_1 \cdot p_5 \simeq p_2 \cdot p_5 \simeq m_{c,h}^2 \tag{II.135}$$

$$p_{1,2,5} \cdot p_3 \simeq \frac{3}{2}\mu^2(1 - z_{13}) \tag{II.136}$$

$$p_{1,2,5} \cdot p_4 \simeq \frac{3}{2}\mu^2(1 + z_{13}) \tag{II.137}$$

$$p_3 \cdot p_4 \simeq 2p_f^2 = \frac{9}{2}\mu^2 \tag{II.138}$$

An important observation is that $m_{c,h} \gg \mu$, i.e. having spread gives us a fictitious suppression, compared to the maximal possible upper limit. The maximal amplitude is therefore given diagrams scaling like

$$|\mathcal{M}|^2 \propto \frac{1}{(p_1 \cdot p_3)^2} \frac{1}{(p_2 \cdot p_4)^2} \tag{II.139}$$

which, since they only contain one energy scale, gives us immediately the scaling

$$\int \mathrm{d}\Omega \, |\mathcal{M}|^2 \sim \frac{1}{\mu^2} . \tag{II.140}$$

Comparing Eq. (II.140) to the caculated processes in table II.5, we find that we not always have maximal divergence. As before, this is due to cancellations at amplitude level depending on the specific physical process.

While the estimates in Eq. (II.132) and Eq. (II.140) serve as a good guideline and a valuable sanity check for the full computation, we find that they are in most cases too conservative. Due to less divergent pole structures of specific amplitudes one expects to find a result which is smaller by orders of magnitudes by performing a full computation of the specific process. We refer again to the results for a few selected processes in tables II.2, II.3, II.4, II.5, for which we have performed the full calculation.

II.5 Results

We present here the regions in parameter space where the effects discussed in the sections before become relevant. We keep $\beta/H = 20$ and $c_{\text{vac}} = 0.1$ fixed, as well as $T_{\text{n}}/T_{\text{eq}} = 1$ or $T_{\text{n}}/T_{\text{eq}} = 10^{-2}$, and show the region when the probability of an interaction of the respective kind becomes larger than one for values of the scale of the PT v_ϕ and the gauge coupling g. We distinguish between an abelian U(1) and a non-abelian SU(3). Although results are shown for $g \leq 1$, results for $g = \mathcal{O}(1)$ must be interpreted with care, consindering that this calculation is only the leading order of a perturbative computation. We also distinguish between shell particles produced from LO interaction, or Bremsstrahlung radiation, either reflected or transmitted particles, see Tab. I.1.

In Fig. II.2 we show the region where shell reversal becomes relevant. Here strongly boosted shell particles may reverse their momentum due to collision with a, from their point of view, wall of boosted particles in the bath. More details can be found in Sec. II.1.1.

In Fig. II.3 we show the region where shell dissipation becomes relevant. Here shell particles may change their momentum by an $O(1)$ factor, due to the same type of scattering as for the momentum reversal of shells. More details can be found in Sec. II.1.2.

In Fig. II.4 we show the region where bath reversal becomes relevant. Here the bath particles collide with a strongly boosted wall of shell particles, due to which they may reverse their momentum. More details can be found in Sec. II.2.

As can be seen in the figures, the last three effects become larger in the non-abelian case. This is because of an additional allowed interaction, namely Møller scattering, which dominates in most of the parameter space.

In Fig. II.5 we show the region where phase space effects become relevant. This includes physical effects as Bose-Einstein condensation or Fermi exclusion, as well computational problems due to a breakdown of perturbativity. More details can be found in Sec. II.3.

We find that in the non-Abelian case a larger region of the parameter space is not allowed to free-stream. This is because the condition for the breakdown of perturbativity scales with g^4 for non-abelian gauge bosons, compared to g^2 for abelian gauge bosons, see Eq. (II.90) and Eq. (II.89).

In Fig. II.6 we show the region where number changing interactions become relevant. Number changing interactions modify the number density and average energy of particles in the shell and in the bath due to interactions of both with each other and with themselves. More details can be found in Sec. II.4.

Number changing interactions behave roughly the same for abelian and non-abelian theories. The main difference is due to the additional number density of the shell particles contributing to the thermal mass. For all our processes however the thermal mass only enters logarithmically.

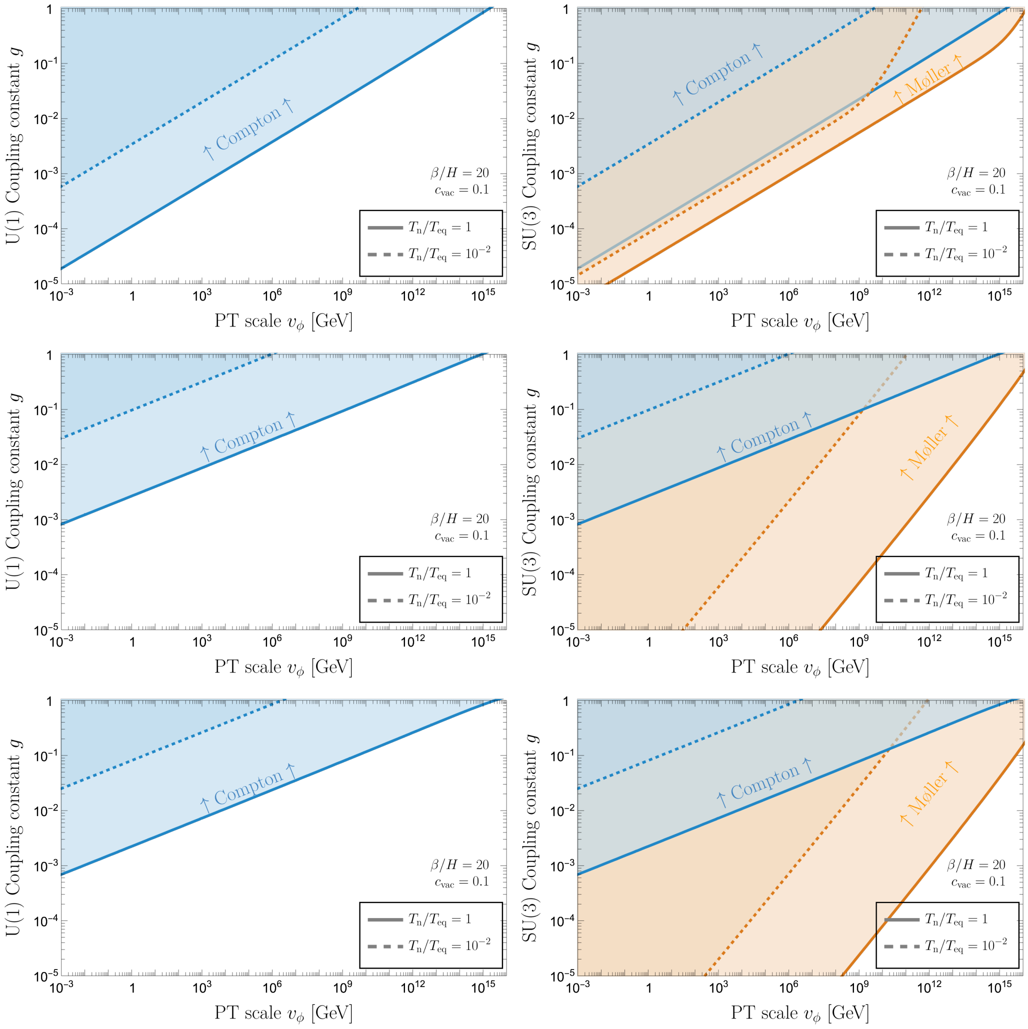

Figure II.2: *Region of shell reversal, see sec. II.1.1, for shell particles produced from LO interaction (**top**), Bremsstrahlung radiation, either reflected (**middle**) or transmitted (**bottom**), assuming abelian (**left**) or non-abelian (**right**) gauge interaction. The shell particles of interest do not free-stream in the colored regions.*

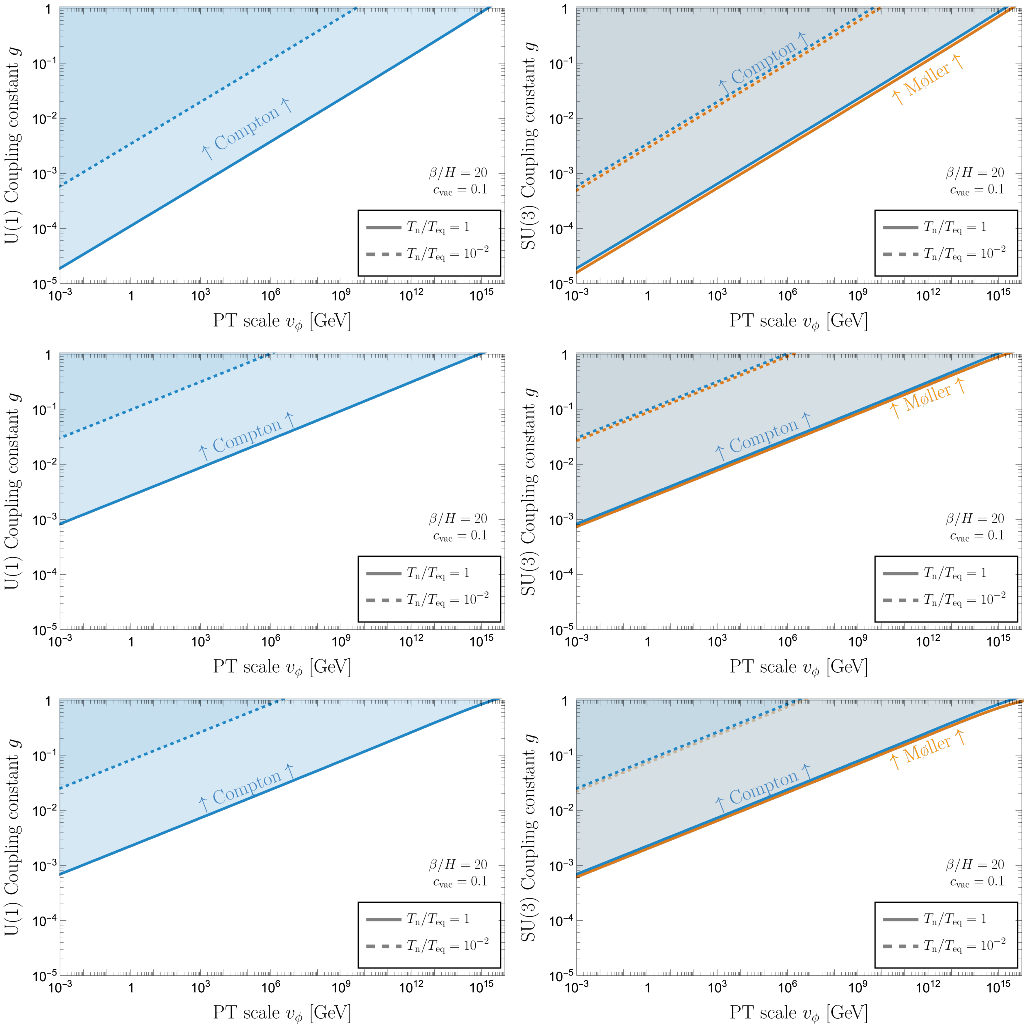

Figure II.3: *Region of shell dissipation, see sec. II.1.2, for shell particles produced from LO interaction (**top**), Bremsstrahlung radiation, either reflected (**middle**) or transmitted (**bottom**), assuming abelian (**left**) or non-abelian (**right**) gauge interaction. The shell particles of interest do not free-stream in the colored regions.*

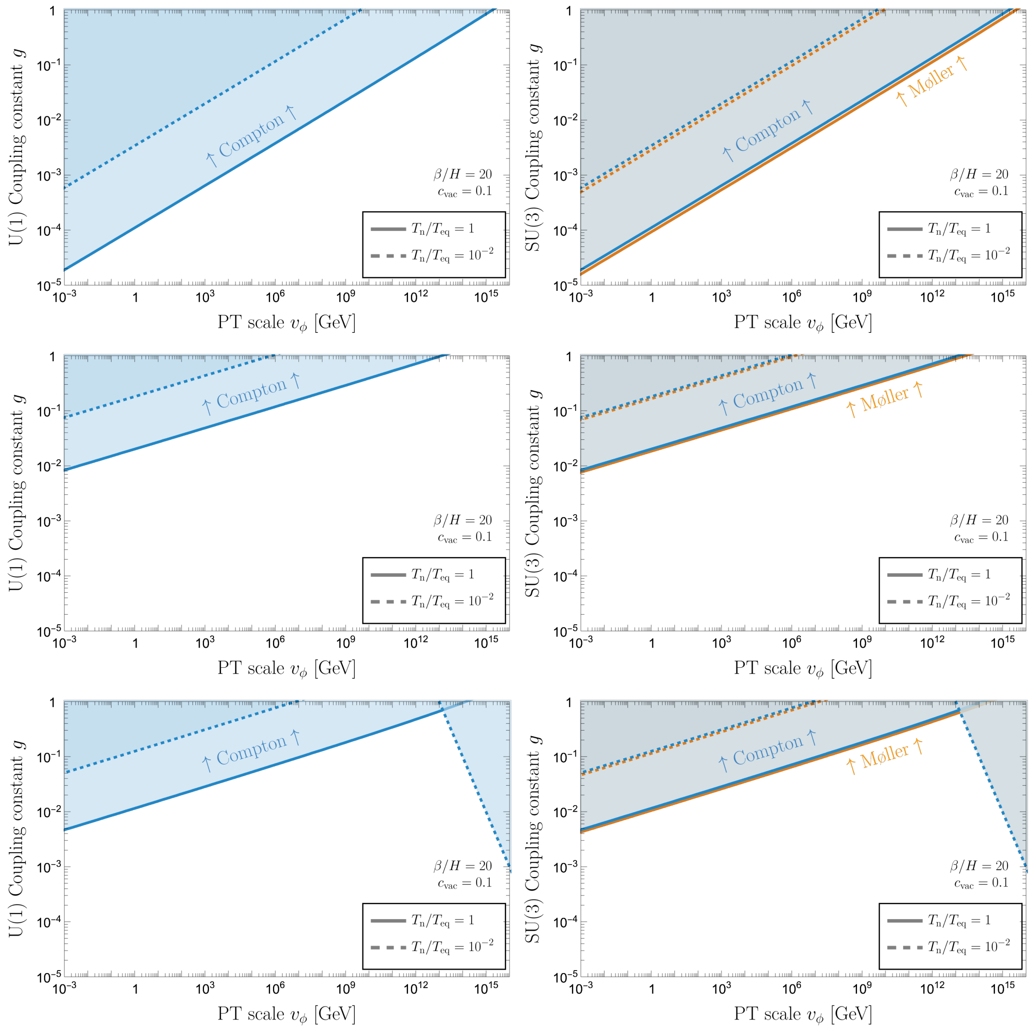

Figure II.4: *Region where bath particles don't reach the wall, see sec. II.2, for shell particles produced from LO interaction (**top**), Bremsstrahlung radiation, either reflected (**middle**) or transmitted (**bottom**), assuming abelian (**left**) or non-abelian (**right**) gauge interaction. The shell particles of interest do not free-stream in the colored regions.*

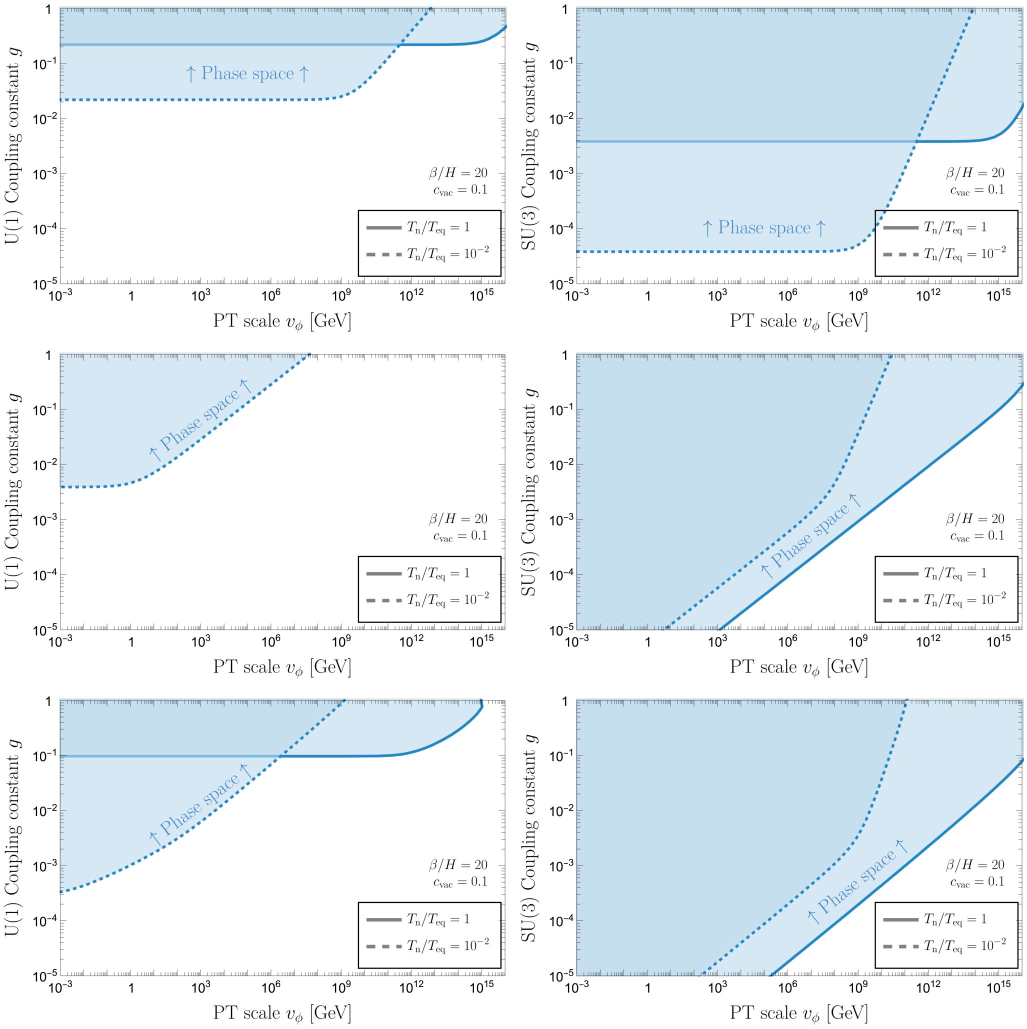

Figure II.5: *Region of broken perturbativity due to large phase space distribution function, see sec. II.3, for shell particles produced from LO interaction (**top**), Bremsstrahlung radiation, either reflected (**middle**) or transmitted (**bottom**), assuming abelian (**left**) or non-abelian (**right**) gauge interaction. The shell particles of interest do not free-stream in the colored regions.*

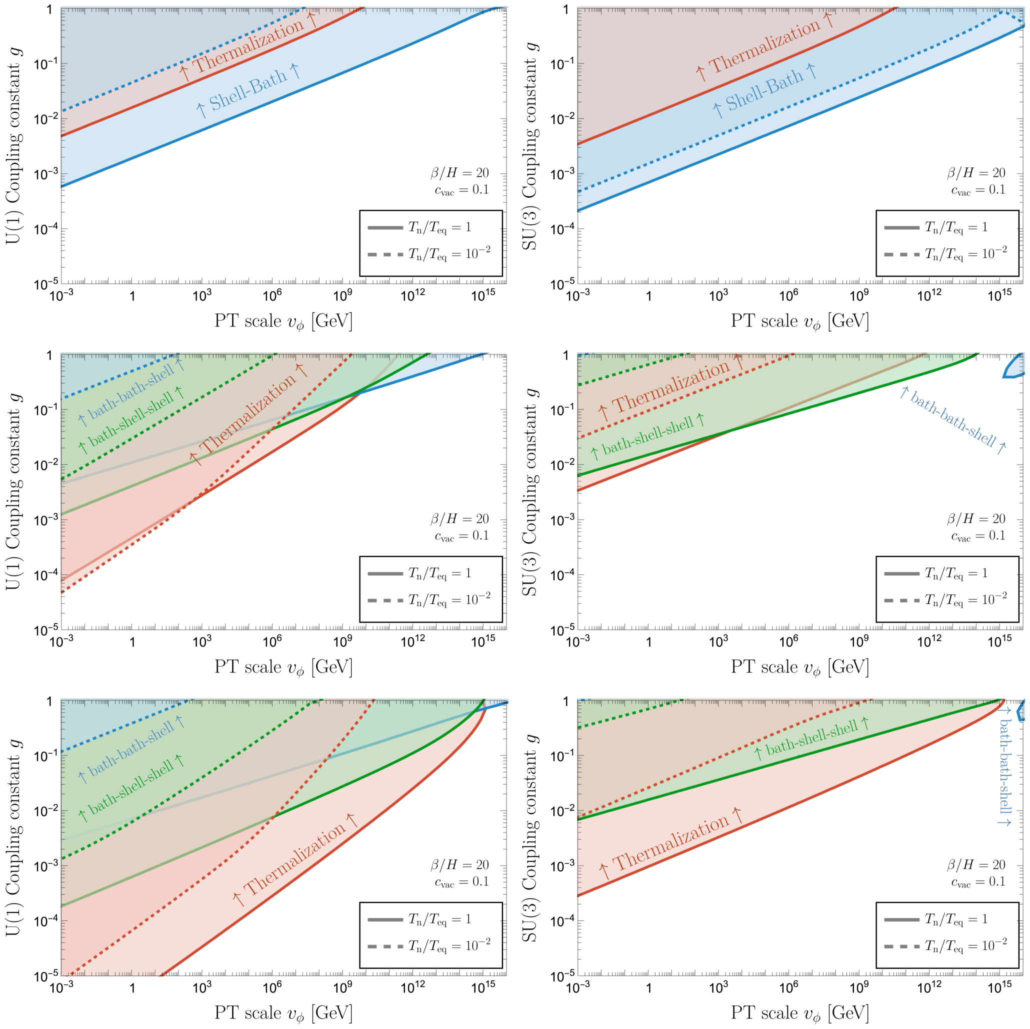

Figure II.6: *Region of number changing interactions, see sec. II.4, for shell particles produced from LO interaction (**top**), Bremsstrahlung radiation, either reflected (**middle**) or transmitted (**bottom**), assuming abelian (**left**) or non-abelian (**right**) gauge interaction. The shell particles of interest do not free-stream in the colored regions.*

III – Bubbletron and implications for heavy dark matter

Bubble walls that expand with ultra-relativistic velocities store a lot of energy, locally much higher than both the bath temperature and the scale of the PT. Wall interactions with the bath then necessarily accelerate particles to high energies and accumulate them into shells, as first worked out in specific cases in [55, 89, 98, 99]. Collisions of shells from different bubbles constitute a ultra-high-energy collider in the early universe, which we dub bubbletron. [1]

In this section we perform a quantitative study of bubbletrons. We calculate the resulting production of heavy particles in Sec. III.1. In Sec. III.2 we apply the bubbletron to the production of heavy DM and correlate them with the GW from the PT in Sec. III.3.

III.1 Production of heavy particles

We have summarized the key parameters (number density, energy, thickness) of shells from different models we have listed in Tab. I.1.

To give a quantitative idea of the center-of-mass energies achievable from their collisions, let us consider as an example the case of gauge bosons, with mass m_V, radiated and reflected by the walls (see Fig. III.1). If shells free stream until they collide, one has the typical center-of mass collision energy squared (see Fig. III.2)

$$s_{\text{coll}} \simeq 4\,\gamma_{\text{coll}}^2\,E_V^2 \simeq 0.4\,\gamma_{\text{coll}}^2\,m_V^2\,, \tag{III.1}$$

where E_V is the typical energy of a reflected shell particle in the wall frame and we have assumed heads-on collisions for simplicity. In the second equality we have used $E_V^2 \simeq 0.1 m_V^2$, which we computed from the distribution $dP_V \propto \frac{dk_\perp^2}{k_\perp^2}\frac{dE_V}{E_V}(\frac{m_V^2}{m_V^2+k_\perp^2})^2$ [89], with $k_\perp$ the component of V momentum parallel to the wall. Interestingly, collision energies can lie above the scales of both grand unification [9] and inflation [123],

$$\sqrt{s_{\text{coll}}} \simeq 1.7\cdot 10^{17}\ \text{GeV}\,g\,\frac{\gamma_{\text{coll}}}{\gamma_{\text{run}}}\frac{T_{\text{n}}}{T_{\text{eq}}}\frac{1}{(c_{\text{vac}}g_{\text{Ri}})^{1/4}}\frac{20}{\beta/H}\,. \tag{III.2}$$

Let us further consider for simplicity a gauged $U(1)$ with coupling g spontaneously broken by a scalar ϕ with charge 1. The condition that shells free stream until collision

---

[1] Bubbletrons are not to be confused with the idea of testing new particles (lighter than Hubble) via their imprint on primordial non-gaussianities, which was named 'cosmological collider' [122] by a possible analogy with laboratory colliders, but where actually no acceleration mechanism is in place.

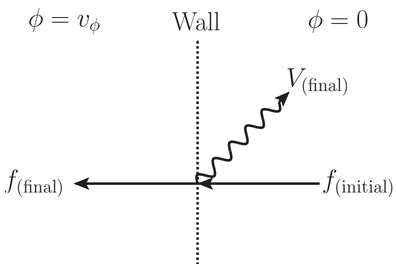

Figure III.1: The shell source considered for reflected gauge bosons. Charged particles entering the bubble can radiate a gauge boson which is reflected by the wall back into the false vacuum phase. These gauge bosons form shells propagating in front of the bubble walls.

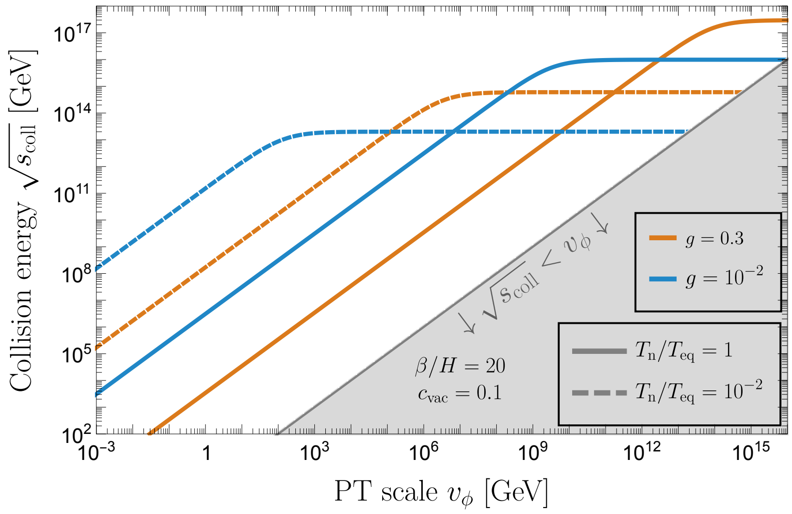

Figure III.2: Center-of-mass scattering energies of two gauge bosons radiated and reflected at the walls of different bubbles.

is realised for small g, large v_ϕ, or large v_ϕ/T_n, see chapter II and [124]. In that case one obtains collisions at energies much larger than the scale of the PT, and thus potentially than the temperature ever reached by the universe after inflation, opening up the possibility to test such high energies with cosmology.

We assume that a collision of particles i and j from two different shells produces one much heavier particle Y with cross section σ_{ij}. Since the total number of particles is conserved, we can describe the compression of particles into the shell by

$$\mathcal{N}_{a\to c} N_a = N_c \tag{III.3}$$

$$\int_{\text{bubble}} \mathrm{d}^3 r\, \mathcal{N}_{a\to c} n_a(r) = \int_{\text{shell}} \mathrm{d}^3 x\, n_c(x)\,, \tag{III.4}$$

where N_a particles produce N_c particles with a probability of $\mathcal{N}_{a\to c}$, see Tab. I.1.

The produced number density is given by

$$\int_{\text{bubble}} \mathrm{d}^3 r\, n_{\text{DM}} = \frac{2}{2} \int_{\text{shell}} \mathrm{d}^3 x \int_{\text{shell}} \mathrm{d}^3 y\, n_i(x) n_j(y) \sigma_{ij}(x,y) \cdot \frac{1}{A_{\text{shell}}}\,, \tag{III.5}$$

with $A_{\text{shell}} = 4/piR_c^2$ the surface area of the shell. The last factor accounts for the averaged production of particles only in this thin spherical shell.

Under the assumption that the cross section $\sigma_{ij}(x,y)$ does not depend on the integration variables, which is only true if it does not depend on the scattering energy $s = s(\gamma_{wp}(r(x)))$, the two integrals factorize, and we have

$$Y_{\text{DM}} \cdot s_{\text{tot}} \simeq \frac{1}{V_{\text{bubble}}} \Big(\int_{\text{shell}} \mathrm{d}^3x \, n_i(x) \Big) \Big(\int_{\text{shell}} \mathrm{d}^3y \, n_j(y) \Big) \sigma_{ij} \cdot \frac{1}{A_{\text{shell}}} \tag{III.6}$$

$$= \Big(\frac{1}{V_{\text{bubble}}} \int_{\text{bubble}} \mathrm{d}^3r \, \mathcal{N}_{a\to c} n_a(r) \Big)^2 \sigma_{ij} \cdot \frac{V_{\text{bubble}}}{A_{\text{shell}}} \tag{III.7}$$

$$= \frac{\sigma_{ij} R_c}{3} (\mathcal{N}_{a\to c} n_a)^2 \,, \tag{III.8}$$

where we used that the number density of dark matter and n_a are homogeneous.

We find that the produced number density is independent of the number of shells per Hubble volume.

The discussion above applies to any bubbletron, including those where different populations are colliding. For concreteness, we now specify it to the case of a gauged $U(1)$, with $i = j = V$, for which [89]

$$\mathcal{N}_{b\to V} \simeq \frac{g_{\text{emit}}}{g_{\text{Ri}}} \frac{g^2}{16\pi^2} \log_V^2, \quad \log_V^2 = \log \frac{m_V^2}{\mu^2} \Big(\log \frac{m_V^2}{\mu^2} - 2 \Big), \tag{III.9}$$

where g_{Ri} is the number of relativistic degrees of freedom in the bath and g_{emit} is the subset charged under $U(1)$, which can thus emit a V. Here μ is an IR cut-off which, dealing with an abelian theory, we take as the thermal mass $\mu^2 \simeq \frac{g_{\text{emit}}}{10} g^2 T_n^2$. In principle one should also include the screening length due to the high density of particles in the shell (see e.g. [55]), but the V's are $U(1)$ singlets and so do not contribute at this order, and the density of fermions or scalars in the shell is suppressed, with respect to n_V, by extra powers of g^2 or $1/\gamma_{\text{coll}}$. We assume further that a heavier fermion Y with charge q_Y under the $U(1)$ exists in the spectrum. We compute the $Y\bar{Y}$ production cross section as

$$\sigma_{VV\to Y\bar{Y}} = \frac{q_Y^4 g^4}{4\pi s} f_{Y\bar{Y}} \xrightarrow[s \gg M_Y^2]{} \frac{q_Y^4 g^4}{4\pi s} \Big(\log \frac{s}{M_Y^2} - 1 \Big) \,, \tag{III.10}$$

where in figures and numerical results we use the full expression $f_{Y\bar{Y}}(y \equiv \frac{4m_Y^2}{s}) = (-\sqrt{1-y}(1+y) + (2 + (2-y)y)\tanh^{-1}(\sqrt{1-y}))$. Using Eq. (I.27), $m_V = g v_\phi$, $n_b = g_{\text{Ri}} \zeta(3) T_n^3/\pi^2$ and $s_{\text{RH}} = g_{\text{RH}} 2\pi^2 T_{\text{RH}}^3/45$, with $T_{\text{RH}} = (30 c_{\text{vac}}/(g_{\text{RH}}\pi^2))^{\frac{1}{4}} v_\phi$ the reheating temperature and g_{RH} the number of relativistic degrees of freedom after the PT, we find

$$Y_{Y+\bar{Y}}^{U(1)} \simeq 3.1 \cdot 10^{-20} g^2 \Big(\frac{T_n}{T_{\text{eq}}} \Big)^4 \Big(\frac{\gamma_{\text{run}}}{\gamma_{\text{coll}}} \Big)^2 \frac{v_\phi}{\text{TeV}} \frac{\beta/H}{20} \frac{g_{\text{emit}}^2}{g_{\text{Ri}}}$$
$$\Big(\frac{q_Y^2 g^2/4\pi}{0.1} \Big)^2 \Big(\frac{c_{\text{vac}}}{0.1} \Big)^{3/4} \Big(\frac{100}{g_{\text{RH}}} \Big)^{1/4} \frac{f_{Y\bar{Y}} \log_V^4}{100} \,. \tag{III.11}$$

We show the Yield of the Y particle in Fig. III.3.

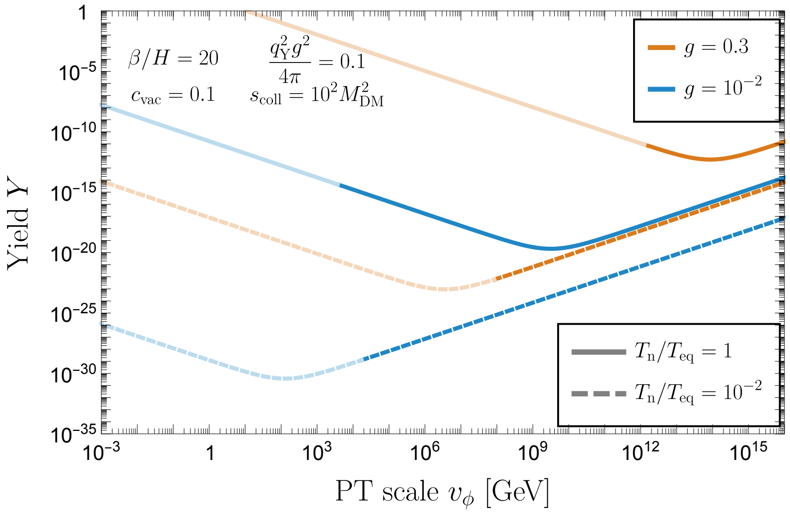

Figure III.3: Yield of secondary particles Y produced from collision of radiated reflected $U(1)$ gauge bosons V. Lines become lighter when free-streaming conditions (see chapter II) are not respected, and thus our derivation of the yield should be changed.

We stress that Eqs. (III.11), and the more general one (III.8), apply only in regions of parameter space where the free-streaming conditions (see Sec. II) are satisfied. We display this in Fig. III.4 by interrupting the lines of $Y_Y^{U(1)}$ as soon as the free-streaming conditions are violated. Our calculations have potentially wide applications, whcih we begin to explore here for the production of heavy dark matter.

III.2 A bubbletron application: heavy dark matter

We now specify our discussion to the case where Y is stable on cosmological scales, and therefore a potential DM candidate. We first motivate the need of a non-standard (WIMP) model for a heavy DM candidate in Sec. III.2.1, and then report the implications for the maximal dark matter mass in Sec. III.2.2.

III.2.1 Unitarity limit on thermal dark matter mass

For dark matter produced via a thermal mechanism one can derive an upper bound on the allowed dark matter mass. Here we recapitulate the original paper by Griest and Kamionkowski [16]. The limitations and conditions of this bound which, since its original proposal in 1990, has motivated many models and scenarios to evade its conditions and therefore the mass limit.

We start with the second Kolomogorov axiom that probabilities are bound by unitarity, $P_{\rm ine}^{(J)} \lesssim 1$. This applies also to the expansion of any inelastic scattering cross section in terms of partial waves, such that we have

$$\sigma_{\rm ine}^{(J)} \lesssim \frac{\pi(2J+1)}{p_i^2}\,. \tag{III.12}$$

Expressing the momentum in terms of particle mass and relative velocity, $p_i^2 = E_i^2 - m_i^2 = \gamma^2 m^2 - m^2 = \frac{v^2}{1-v^2}m^2 \simeq m^2 v^2 = m^2 \frac{v_{\rm rel}^2}{4}$, this gives an upper limit on the cross section of the form

$$\sigma_{\rm ine}^{(J)} \lesssim \frac{\pi(2J+1)}{m_{\rm DM}^2 v_{\rm rel}^2/4} = \frac{4\pi(2J+1)}{m_{\rm DM}^2 v_{\rm rel}^2}\,. \tag{III.13}$$

In the standard freeze-out scenario the predicted DM abundance is

$$\Omega_{\rm DM} H_0^2 = 2^{n_{\rm Dirac}} \frac{\pi}{9\sqrt{10}} \frac{g_{*S}(T_0)\sqrt{g_*(x_F)}}{g_{*S}(x_F)} \frac{T_0^3}{M_{\rm Pl}^3} \frac{1+n/2}{\sigma_0{}^2} x_F^{1+n/2}\,, \tag{III.14}$$

where

$$\langle \sigma v \rangle_{\rm f.o.} \equiv \sigma_0 x_F^{-n/2} \tag{III.15}$$

and[3]

$$n_{\rm Dirac} = \begin{cases} 0 & \text{particle} = \text{antiparticle} \\ 1 & \text{particle} \neq \text{antiparticle} \end{cases} \tag{III.16}$$

Rearranging equations (III.13) and (III.14) for $\langle \sigma v_{\rm rel} \rangle$ one arrives at

$$2^{n_{\rm Dirac}} \frac{\pi}{9\sqrt{10}} \frac{g_{*S}(T_0)\sqrt{g_*(x_F)}}{g_{*S}(x_F)} \frac{T_0^3}{M_{\rm Pl}^3} \frac{1+n/2}{\Omega_{\rm DM} H_0^2} x_F \lesssim \frac{4\pi(2J+1)}{m_{\rm DM}^2} \sqrt{\frac{x_F}{\tau}}\,, \tag{III.17}$$

where $\tau = 6$ or $\tau = \pi$ is an $\mathcal{O}(1)$ factor due to taking the thermal average.

Assuming $g_*(x_F) = g_{*S}(x_F)$ one gets an upper limit on the mass of the DM particle,

$$m_{\rm DM} \lesssim \sqrt{\frac{2J+1}{2^{n_{\rm DM}}(1+n/2)}} \cdot 136\text{TeV} \cdot \left(\frac{\Omega_{\rm DM} h^2}{0.12}\right)^{1/2} \left(\frac{25}{x_F}\right)^{1/4} \left(\frac{\pi}{\tau}\right)^{1/4} \left(\frac{g_*(x_F)}{86.25}\right)^{1/4}\,, \tag{III.18}$$

which depends on the dominant partial wave index J.

For $J = 0$, $n = 0$, $n_{\rm Dirac} = 0$, $\Omega_{\rm DM} h^2 = 1$, $x_F = 28$, $\tau = 6$, $g_*(x_F) = 107$, we find

$$m_{\rm DM} \lesssim 360\ \text{TeV}\,. \tag{III.19}$$

This upper limit on the mass of DM was originally achieved by the assumption of a flat universe, since then the relic abundance $\Omega_{\rm DM}$ is bounded by unitarity. Using the measured value for $\Omega_\chi h^2 \simeq 0.12$ [5] the limit becomes smaller by a factor of roughly 3.

Evading this bound is of course strongly motivated by any New Physics Models with UV scales above the unitarity bound. There have been many models proposed in the literature to achieve this, either by modifying the thermal history of the universe and thereby diluting the dark matter Yield, or by producing DM non-thermally. We are now going to explore a new mechanism to produce DM out-of-equilibrium, via bubbletrons.

---

[3] Illustrative argument: If the particle is its own antiparticle, then there is a higher chance that two random DM particles colliding actually annihilate eachother, therefore the final relic density is lower compared to the case when the particle is not its own antiparticle.

III.2.2 Maximal mass of heavy dark matter

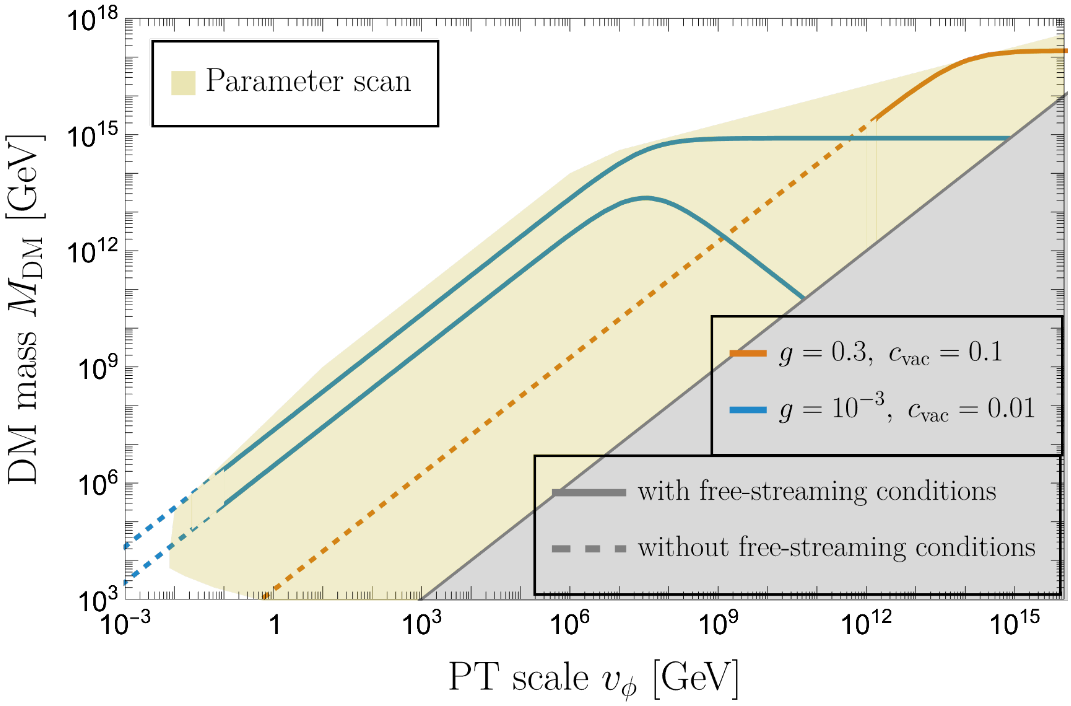

Figure III.4: *Mass of dark matter produced by a bubbletron of reflected* $U(1)$ *gauge bosons. Lines:* $M_{\rm DM}$ *in two representative scenarios, both with* $\beta/H = 20$ *and* $T_n = T_{\rm eq}$*. Lines turn dashed when they stop satisfying the condition of shells free streaming. The champagne shaded area is the envelope of all the solid lines we obtain upon varying* g, $T_n/T_{\rm eq}$, β/H, $c_{\rm vac}$, q_Y*. See text for more details.*

We now specify our discussion of Sec. III.1 to the case where Y is stable on cosmological scales, and therefore a potential DM candidate. We assume zero initial abundance of $Y, \bar{Y}$ and impose that their yield from shell collisions reproduces the observed DM one, i.e. $Y^{U(1)}_{Y+\bar{Y}} = Y^{\rm DM}_{\rm Planck} \simeq 0.43$ eV$/M_{\rm DM}$ [125] with $M_Y = M_{\rm DM}$. This allows us to plot lines of DM abundance on an $M_{\rm DM} - v_\phi$ plane, for any value of the other parameters g, T_n, etc. We do so varying the parameters as $1 \geq T_n/T_{\rm eq} \geq 10^{-4}$, $1 \geq g \geq 10^{-5}$, $10^4 \geq \beta/H \geq 10$, $1 \geq c_{\rm vac} \geq 10^{-3}$, $10^{-4} < g^2 q_Y^2/4\pi < 0.1$, with the perturbativity condition $P_{b\to V} < 1$. We then discard all lines of DM abundance that do not satisfy the free streaming conditions visualized in the figures in chapter II. The envelope of the remaining lines gives the maximal DM mass as a function of v_ϕ, which we visualize in Fig. III.4. For easiness of the reader, we also visualize the lines corresponding to two benchmark values of the parameters. One sees that in general there are two solutions that reproduce $Y^{\rm DM}_{\rm Planck}$, one for $M^2_{\rm DM} \to s_{\rm coll}/4$ and one for smaller $M_{\rm DM}$. At large g the latter line falls in the region $M_{\rm DM} < v_\phi$. At large v_ϕ, $\gamma_{\rm coll} = \gamma_{\rm run}$, which decreases because bubbles have less room to expand and $M_{\rm DM}$ saturates to a constant. We stop the plots at $v_\phi = 10^{16}$ GeV in order to avoid the 'ping-pong' regime (see e.g. [55]) where gauge bosons are reflected multiple times. At small values of v_ϕ the free-streaming conditions impose small values of g.

III.3 Gravitational wave signal

We have described the computation of the gravitational wave signal in Sec. I.5. Here we display, in Fig. III.5, the GW spectrum for three different benchmark points. The one for $v_\phi = 0.1$ GeV can provide a good fit [126, 127] of pulsar timing array data [128–131].

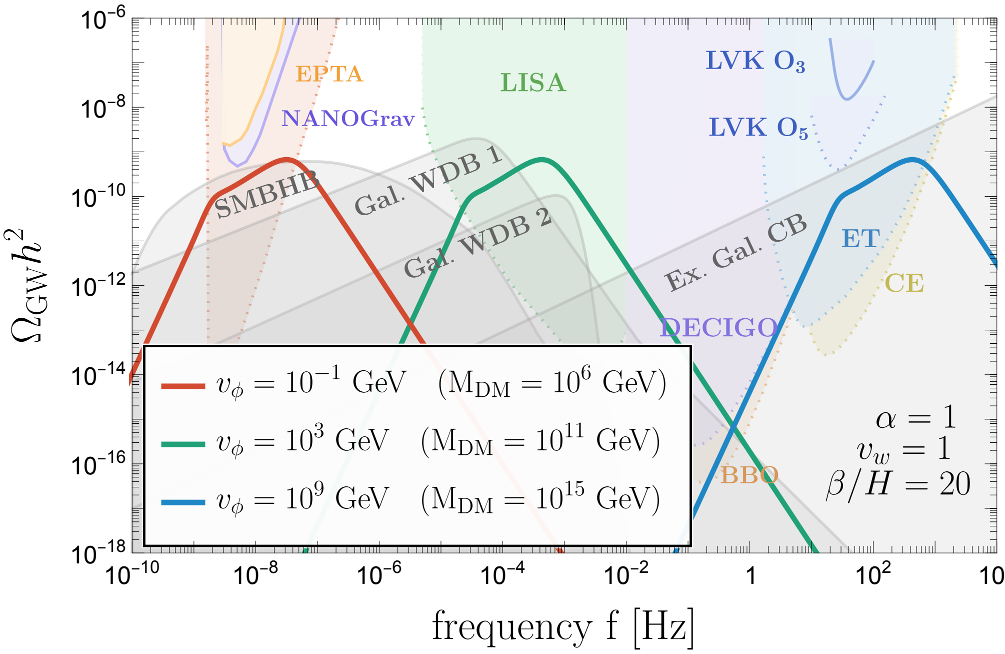

Figure III.5: *Lines: GW signal from a* $U(1)$ *gauge phase transition. The associated bubbletron can produce dark matter with mass* $M_{\rm DM}$ *up to the values written in the figure for each* v_ϕ*, for* $\beta/H = 20$ *and* $\alpha = (T_{\rm n}/T_{\rm eq})^4 = 1$*. Shaded in gray: expected foregrounds [128, 136–140]. Shaded in color: current [128–130] and projected limits [111, 131–135].*

IV – Baryogenesis from supercooled confinement

In this chapter we propose a novel mechanism for baryogenesis from a FOPT, which works for scales of the PT down to TeV, which allows for new ways of testing the picture with respect to previous literature, e.g. through collider searches and with LISA. In section IV.1 we explain and motivate the need for baryogenesis. In section IV.2 we define the BSM model and in section IV.3 we compute the Yield. In section IV.4 we determine the available parameter space both of the BSM model and the cosmological phase transition. In section IV.5 we collect constraints due to experiments performing measurements below the TeV-scale. Finally, in section IV.6 we present our results and conclude.

IV.1 Introduction to baryogenesis

We now come to the other open problem in physics we deal with in this thesis. On Earth we are clearly surrounded by more matter than antimatter. To cosmologically measure the matter-to-antimatter ratio there are two ways, see e.g. [141]. One is using the abundance of light elements during Big Bang nucleosynthesis (BBN) [142], the other is using the peaks of the CMB [5]. They give consistent results for the asymmetry,

$$\eta = \frac{n_b - n_{\bar{b}}}{s} \simeq 8.6 \cdot 10^{-11} \,. \tag{IV.1}$$

In order to provide an explanation for baryogenesis, models must satisfy in general three conditions, the so-called Sakharov conditions [143, 144].

- Baryon number violation: without any processes violating baryon number it is not possible to go from an initially symmetric state to an asymmetric state. One could start from an already existing asymmetry, which is however unsatisfying, since it would only impose the asymmetry, not explain it. Additionally, if one accepts the paradigm of inflation, which is the leading solution to some open cosmological problems like the flatness and the horizon problem, then any possible initial asymmetry would have been diluted away.
- C and CP violation: If C would be conserved, the reactions producing baryons would be balanced by the reactions producing anti-baryons. For CP the same argument holds with left-handed baryons and right-handed anti-baryons, and vice-versa.

- Out-of-equilibrium production: In thermal equilibrium the reverse reaction would be equally efficient, washing out any possible baryon asymmetry generated.

The necessary condition to have CP-violation in the Standard Model can be summarized as [145]

$$\text{CP violation} \qquad \Leftrightarrow \qquad \text{Im}\left\{\det\left\{M_u M_u^\dagger; M_d M_d^\dagger\right\}\right\} \neq 0\,, \tag{IV.2}$$

where M_u and M_d are the up and down quark matrices. The imaginary part in Eq. (IV.2) can be written in an elegatn way as

$$\text{Im}\left[V_{ij}V_{ik}V_{lk}^*V_{lj}^*\right] = \mathcal{J}\sum_{m,n=1}^{3}\epsilon_{ilm}\epsilon_{jkn}\,, \tag{IV.3}$$

where V_{ij} are the elements of the CKM matrix. The numerical value of the Jarlskog determinant $\mathcal{J}$ in the SM determined by experiments [146] is given by

$$\mathcal{J} \simeq 3 \cdot 10^{-5}\,. \tag{IV.4}$$

This implies that there is CP-violation in the SM, it is however too small to explain the observed asymmetry. In addition, the cosmological evolution of the SM lacks processes which are enough out-of-equilibrium, therefore failing in satisfying another Sakharov condition [65, 66, 144, 147]. This is therefore a huge motivation for physics beyond the SM.

We notice immediately that the bubbletron is a mechanism of out-of-equilibrium particle production, thereby providing the necessary ingredients for successful baryogenesis. With this as a starting point, we only need to construct a model which violates B, C, and CP.

IV.2 Model

In this section we build a model giving us a mechanism of baryogenesis. Our model is a generalization of the one proposed in [72], which, to our knowledge, was the first paper to realize baryogenesis simply from the mass-gain mechanism at PTs with relativistic bubble walls (i.e. the mechanism that leads to the LO pressure that we discussed in Sec. I.4.3)[1]. Ref [72] focused on weakly coupled PTs, we consider instead confining PTs and show that this allows to open the parameter space towards lower v_ϕ, and therefore make the mechanism testable e.g. with colliders and LISA.

We consider a new confining sector which, among its BSM hadrons, includes to generations of scalar particles Δ_i which have interactions with the SM that violate C and CP, and which are assumed to dominantly decay to elementary particles, including the SM. This for example could be because of selection rules of the strong sector which we do not specify here, or because of accidental reasons linked to the spectrum of composite states.

---

[1] See [71] and again [72] for two other mechanisms realizing baryogenesis at fast bubble walls, but relying on the production of heavy particles.

The Lagrangian describing the interactions of this state with the elementary sector is given by

$$\mathcal{L} \supset y_{di} \Delta_i \overline{d^c_R} d'_R + y_{ui} \Delta_i \overline{N_R} u^c_R + \text{h.c.}\,, \tag{IV.5}$$

where we have two generations $i = 1, 2$ of Δ_i, which transform under the SM as

$$\Delta_i \sim (3, 1)_{2/3}\,, \tag{IV.6}$$

and a gauge elementary singlet fermion N_R. The primed superscript notes that the two right-handed down-type quarks must be of different generations, that is

$$y_{di} \overline{d^c_R} d'_R \sim y_{li} \epsilon_{lmn} \overline{d^c_{m,R}} d_{n,R}\,. \tag{IV.7}$$

We have chosen the same particles, quantum numbers and interactions con- sidered in Ref. [72], such that our only difference with their mechanism is in the nature of the PT (strongly vs weakly coupled) and the comparison of the two pictures is straightforward. The mass term is given by

$$\mathcal{L} \supset \begin{pmatrix} \Delta_1^* & \Delta_2^* \end{pmatrix} \begin{pmatrix} m_{11} & m_{12} \\ m_{21} & m_{22} \end{pmatrix} \begin{pmatrix} \Delta_1 \\ \Delta_2 \end{pmatrix}\,. \tag{IV.8}$$

The unrotated mass matrix is a general matrix with complex entries, but since it is Hermitian the eigenvalues are real. After performing the rotation

$$\begin{pmatrix} \Delta_1 \\ \Delta_2 \end{pmatrix} \to U(2) \times \begin{pmatrix} \Delta_1 \\ \Delta_2 \end{pmatrix} \tag{IV.9}$$

we can eliminate the off-diagonal entries in the mass matrix.

That means that the Yukawa matrices are arbitrary complex matrices, although one can eliminate some degrees of freedom through field redefinitions. Requiring however invariance under $U(2)$ forbids the existence of the CP-violating flavor mixing terms in the Lagrangian (IV.5). We therefore expect and find the CP-violation to be proportional to the difference in the masses of the two Δ_i. Therefore we need them to have different masses, but both of the order

$$m_\Delta \simeq 4\pi\, v_\phi\,. \tag{IV.10}$$

If we only have one y_{di} and y_{ui} for each Δ_i, and one N_R, then we have $2 \cdot 4 - 2(\Delta) - 1(N_R) = 4(\text{real}) + 1(\text{phase})$ parameters. This is sufficient to produce baryogenesis, as similarly to the Standard Model we have one physical phase.

IV.3 Yield

We assume that the associated PT in the early universe is strongly first-order and supercooled, such that it proceeds via the picture of 'string fragmentation' proposed in [55]. We here recall the key feature of the dynamics of supercooled confinement which is relevant for the rest of the discussion, and refer the reader to [55] for more details. In supercooled confinement shells of hadrons and of techniquanta (the UV quanta charged under the confining sector, which constitute the hadrons in the IR) are produced at the walls. Importantly, after the PT, their evolution simply ends up into a redistribution of their high energies into masses of the hadrons, such that the value of the final hadron abundance is robust against possible additional effects like those described in Chapter II. We now present the abundance of hadrons, and of the Δ_i in particular, which is the key input we need for working out the rest of the mechanism.

In our model the scalar Δ_i do not exist before the PT, where the degrees of freedom are instead the techniquanta that constitute it and which are at equilibrium, which implies that a $B-L$ asymmetry can be produced by Δ decays only inside the bubbles. Through their interactions, the techniquanta are in equilibrium with the thermal bath before the phase transition and their number density to entropy ratio is given by

$$Y_{\rm TC} \equiv \frac{n_{\rm TC}^{\rm eq}}{s} = \frac{45\zeta(3) g_{\rm TC}}{2\pi^4 g_*}\,, \tag{IV.11}$$

where $g_{\rm TC}$ are the degrees of freedom of Δ, s is the total entropy, and g_* are the effective degrees of freedom. Upon the phase transition, provided that $\gamma > M_\Delta/T_{\rm n}$ such that Δ can be produced inside the bubble, Y_Δ is maintained across the wall, while $n_\Delta^{\rm eq}$ receives a large Boltzmann suppression. The scalars Δ are then out-of-equilibrium inside the bubble and can thus produce a net $B-L$ via their CP violating decays.

This produces the following baryonic yield

$$\frac{Y_B}{Y_B^{\rm obs}} = \epsilon_\Delta \, K_{\rm Sph} \, \frac{Y_{\rm TC}}{Y_B^{\rm obs}} \left(\frac{T_{\rm n}}{T_{\rm RH}}\right)^3 \gamma \, g_{\rm TC} {\rm Br}({\rm had} \to \Delta)\,, \tag{IV.12}$$

where ϵ_Δ is the average baryon number produced in Δ or Δ^* decays, $K_{\rm Sph} = 28/79$ is a sphaleron reprocessing factor, the $(T_{\rm n}/T_{\rm RH})^3$ comes from the entropy production from reheating following the phase transition, $g_{\rm TC} \gg 1$ denotes the degrees of freedom of the quanta of the confining sector and ${\rm Br}({\rm had} \to \Delta)$ is the branching ratio of the hadrons of the confining sector into Δ, which is model-dependent but (much) smaller than 1.

Comparing Eq. (IV.12) with the corresponding Eq. (6) of [72], it follows that due to supercooled confinement there is an enhancement of the yield given by $\gamma g_{\rm TC} {\rm Br}({\rm had} \to \Delta)$, arising from the deep inelastic scatterings (DIS) of the techniquanta of the confining sector [55], which increase the number of hadrons, and via their decay into Δ, effectively increase the final yield.

IV.4 Parameter space for baryogenesis

We now explore in more detail the constraints that our model has to satisfy in order to successfully address baryogenesis.

IV.4.1 Relativistic walls

In the confined sector the friction preasure stopping the bubble walls from running away is due to non-perturbative effects [55]. We find that for our scenario of baryogenesis to work we need ultra-relativistic walls, which requires large supercooling, $T_{\rm n} \ll v_\phi$.

IV.4.2 B and CP violation

Since we require our model to provide the observed baryon number asymmetry, we have to check whether it contains CP violating sources, and explore the relation between the amount of CP violation and the field content of the model. A necessary condition for CP violation is that the above couplings should be complex. Some, but not all the phases, even in a minimal scenario, can be removed through field rephasings $f \to e^{i\alpha_f} f$. To be more concrete let us examine some specific scenarios:

- In the minimal scenario there is only one copy of N_R, one up type quark and one down type quark flavor combination coupling to $\Delta_{1,2}$, providing 4 couplings. One can remove 3 phases by rephasing the Δ_i and N but one phase survives since in general $\mathrm{Arg}(y_{d2}) - \mathrm{Arg}(y_{d1}) \neq \mathrm{Arg}(y_{u2}) - \mathrm{Arg}(y_{u1})$. Thus in this setup there are 4 couplings and 1 (physical) phase.

- One can turn on all the allowed SM quark Yukawa couplings, keeping a single copy of N_R. This setup features 12 couplings, 6 involving down type quarks and 6 involving the up type quarks. We have already used all the freedom of the new fields to absorb the 3 phases as described above, however one can absorb 4 more phases by performing $U(1)$ transformations on the quark fields, with different phases for each flavor in general. Therefore in this setup there are 12 couplings and 5 phases. However it has to be pointed out that rephasing the quarks doesn't leave the charged current of the SM invariant, hence the CKM matrix is not in its canonical form but will have 5 physical phases, instead of the 1 in the canonical form. Therefore the net effect of quark rephasing is to trade the CP violation in the Yukawa couplings of Δ for CP violation in the CKM.

- For 3 copies on N_R, we find 24 couplings (6 from down and 18 from up type quarks). With respect to the previous setup we have the freedom to remove 2 more phases by redefining $N_{2,3}$, therefore we end up with 24 independent couplings and 15 phases.

The couplings of the Lagrangian Eq. (IV.5) lead to the following tree level decay rates for the scalars Δ_i,

$$\Gamma(\Delta_i \to \overline{d_R}\,\overline{d_R}) \simeq \frac{|y_{di}|^2}{8\pi} M_{\Delta_i}\,, \Gamma(\Delta_i \to N u_R) \qquad \simeq \frac{|y_{ui}|^2}{16\pi} M_{\Delta_i}\,, \tag{IV.13}$$

where we have summed over the final state colours for the first decay, but we have left the summation over flavors implicit.

Interference between tree and loop level diagrams leads to CP violation in the decays. The imaginary part of the loop controls the rate asymmetry between Δ_1 and Δ_1^* decays and can be extracted via Cutkosky rules [148]. Focusing on the decays of Δ_1 only, one then finds for the rate asymmetry

$$\epsilon_\Delta = \frac{1}{2\pi} \frac{\mathrm{Im}(y_{d1}^* y_{u1} y_{u2}^* y_{d2})}{|y_{ui}|^2 + 2|y_{di}|^2} \frac{M_{\Delta_1}^2}{M_{\Delta_2}^2 - M_{\Delta_1}^2} \sim \frac{\mathrm{Im}[y^2]}{6\pi} \Big(\frac{M_{\Delta_1}}{M_{\Delta_2}}\Big)^2\,, \tag{IV.14}$$

where we assume that there is no major hierarchy among the Yukawa couplings y and we take generic $\mathcal{O}(1)$ phases. Substituting the above expression in Eq. (IV.12) we obtain the baryonic yield

$$\frac{Y_B}{Y_B^{\rm obs}} = 7\times 10^7\, \frac{g_\Delta\, {\rm Im}[y^2]}{g_*}\Big(\frac{T_{\rm n}}{T_{\rm RH}}\Big)^3\Big(\frac{M_{\Delta_1}}{M_{\Delta_2}}\Big)^2\gamma\, g_{\rm TC}{\rm Br}({\rm had}\to\Delta)\,. \tag{IV.15}$$

IV.4.3 Washout processes

In our scenario the most constraining washout processes are those occurring after the reheating, when thermal equilibrium has been restored. Diquark interactions violating $B-L$ can result in washout if $T_{\rm RH}$ is too high. Off-shell $2\to 2$ scattering processes mediated by Δ have a rate that can be estimated as

$$\Gamma_{\rm WO}\simeq \frac{y^4\, T_{\rm RH}^5}{8\pi M_\Delta^4}\,. \tag{IV.16}$$

This rate is harmless for our scenario provided that it is below the Hubble rate H, namely

$$\frac{M_\Delta}{T_{\rm RH}}\leq \left(\frac{y^4 M_{\rm Pl}}{8\pi g_*^{1/2}T_{\rm RH}}\right)^{1/4}\,. \tag{IV.17}$$

Moreover also inverse decays into on-shell Δ can lead to $B-L$ washout. The Boltzmann suppressed rate is given by

$$\Gamma_{\rm ID}\simeq \frac{3\,y^2}{16\pi}M_\Delta\Big(\frac{M_\Delta}{T_{\rm RH}}\Big)^{3/2}{\rm Exp}\Big[-\frac{M_\Delta}{T_{\rm RH}}\Big]\,. \tag{IV.18}$$

IV.5 Experimental constraints (on the Δ masses)

IV.5.1 Collider searches

Since we have shown that one can easily accommodate baryogenesis from supercooled confinement with the scalar Δ around or below the electroweak scale, the properties of these particles can be probed thanks to their signatures in high-energy colliders.

A first lower bound on the mass of Δ comes from the measurement of the decay width of the Z boson performed at LEP [149]. Since Δ interacts weakly due to its $U(1)_Y$ charge, it can contribute to the Z boson width, provided that $M_\Delta < M_Z/2$. One obtains the following expression for the decay width for Z annihilation into a $\Delta\Delta^*$ pair

$$\Gamma(Z\to\Delta\Delta^*) = \frac{3}{16\pi}\left(\frac{2g\sin^2\theta_W}{3\cos\theta_W}\right)M_Z\left(1-\frac{4M_\Delta^2}{M_Z^2}\right)^{3/2}\,. \tag{IV.19}$$

Since this expression is about one order of magnitude larger than the uncertainty on the Z boson width, $M_\Delta < 45$ GeV is thus excluded.

We note that Δ has the same quantum numbers of a right up-type squark in SUSY, therefore it will share its same production mechanisms at colliders. To our knowledge, the closest searches to our scenario that have been performed are those involving squark decays into diquarks, through R-parity violating (RPV) couplings.

Constraints on top squarks decaying through RPV couplings were first set by the ALEPH experiment at LEP [150], excluding at 95% CL masses below 75 GeV via four-jet searches. More stringent bounds come from further searches performed by CDF at Tevatron [151] and by ATLAS [152] and CMS [153] at the LHC. The combination of these searches rules out top squarks with RPV decay in the 45 GeV $< M_\Delta <$ 770 GeV interval. All these searches aim to detect four jets in the final state associated to the decay of pair produced heavy resonances. This is the typical signature that one would expect associated with Δ, as for the allowed values of its mass and coupling constants it would decay promptly in the detector.

However, as the diquarks and leptoquarks couplings of Δ are expected to be of the same size, some significant branching ratio of Δ scalar could reside in the uN_R channel, such that the signal would be smaller than the one assumed by CMS, and the four-jet limits would get weaker.

Translating these searches to precise bounds on the Δ parameter space is non-trivial and beyond the scope of our work, but for the purpose of our analysis we included the above-mentioned constraints in the parameter space in Fig. IV.2.

IV.5.2 Neutron electric dipole moment

As we have seen in the previous section, the new fields Δ_i and N_R contain new sources of CP violation and therefore give rise to new contributions to the neutron electric dipole moment (nEDM). The experimental bound set by the nEDM collaboration at the Paul Scherrer Institut is given by $|d_n| < 1.8 \times 10^{-26} e \cdot cm$ [154]. In this section we analyze the impact of this bound on our model and show that it does not place significant constraints on the parameter space.

One defines the EDM d of a fermion through the effective Lagrangian

$$\mathcal{L}_{\text{EDM}} = -\frac{i}{2} d\, \overline{\psi} \sigma_{\mu\nu} \gamma_5 \psi F^{\mu\nu}\,, \tag{IV.20}$$

where $F_{\mu\nu}$ is the field strength tensor of the photon.

The diagrams which may give a non vanishing contribution to the CP odd nEDM must have an imaginary component. In general the amplitude of any loop diagram can be recast as a sum of operators O_i weighted by their coefficients C_i, which can be written as $C = y\,L$. In this notation y stands for the product of the couplings of all the vertices and L is a function coming from the loop integration [155]. In principle both y and L are allowed to be complex but diagrams with the heavy Δ and N_R running in the loop cannot have all the intermediate states go on-shell. Therefore the optical theorem implies that $\text{Im}(L) = 0$ and only y can be complex.

Moreover, any combination of couplings entering the nEDM should be invariant under rephasing of the fields, thus we need at least four couplings involving the new states, since $Y = y^*_{d1} y_{u1} y^*_{u2} y_{d2}$ is the simplest combination of the new Yukawas with at least one physical phase. As a consequence one needs to go at least to 2-loop to find a possible non-zero contribution.

The relevant topologies of our model are depicted in Fig. IV.1, they are the so-called Barr-Zee [156] like diagrams. They all give in principle non-zero contributions to the nEDM but for each of them one can always take the contribution of with complex conjugate Yukawa couplings and with the photon attached to the same type of field. One can decompose the sum of each set of conjugate diagrams as

$$\sum_{j=1}^{\#\text{conj.}} \mathcal{A}_j = Y F(M_{\Delta_1}, M_{\Delta_2}) + Y^* F(M_{\Delta_2}, M_{\Delta_1}) \,, \tag{IV.21}$$

where Y is the product of the Yukawa couplings and $F(i,j)$ contains the momenta and masses coming from the loop integration. In general, $F(i,j)$ is not a symmetric function of the scalar masses, but the asymmetry scales like $F(M_{\Delta_2}, M_{\Delta_1}) = F(M_{\Delta_1}, M_{\Delta_2})(1 + \mathcal{O}(k^2/M^2_{\Delta_{1,2}}))$, with k the external photon momentum, therefore it vanishes in the $k^2 = 0$ limit for which the EDM is measured. An explicit proof of this statement is given later in this section. Therefore the sum of the conjugate diagrams ends up being real and thus 2-loop diagrams do not produce a non-vanishing nEDM. There may be contributions to the nEDM at the three loop level, but we believe them to be negligibly small. Therefore, the constraint set by nEDM on the mass Δ turns out to be much less stringent than those coming from colliders.

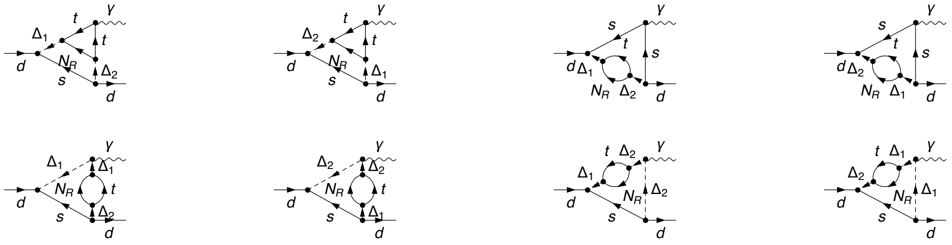

Figure IV.1: *All BSM diagrams contributing to the neutron electric dipole moment with* 4 *different Yukawa couplings, allowing at least in principle a non-zero CP violating contribution, from the Lagrangian in Eq.* (IV.5).

We present an argument why the nEDM due to the 2-loop diagrams in Fig. IV.1 vanishes. We confirm this by having computed the nEDM at 2-loop using Feynman parameters, and we confirm (via numeric integration) that it vanishes exactly.

The starting point is given by the structure of the electromagnetic nucleon vertex in the presence of CP-violation, which is given by

$$i\mathcal{M}^\mu = \overline{u_N}(q)\Big[\gamma^\mu F_E(k^2) + \frac{i\sigma^{\mu\nu}k_\nu}{2m_N} F_M(k^2) + \frac{i\sigma^{\mu\nu}k_\nu}{2m_N}\gamma_5 F_D(k^2)\Big] u_N(p). \tag{IV.22}$$

Here $k = (p - q)$ is the momentum of the photon, m_N is the nucleon mass and the EDM of the nucleon is defined as $d_n = F_D(0)/(2m_N)$. Using the Gordon-decomposition of the vector-axial current, the CP violating ($\cancel{CP}$) part of the above expression reads

$$i\mathcal{M}^\mu_{\cancel{CP}} = d_n \overline{u_N}(q)\gamma_5 u_N(p)(p+q)^\mu \tag{IV.23}$$

Thus we need to concentrate on the $(p + q) \cdot \epsilon$ terms in the computation of the EDM, where ϵ is the photon polarization.

In order to find whether there is a cancellation among the diagrams, we can factor out the inner loop, as it is symmetric under $\Delta_{1,2}$ exchange. Let's focus thus on the outer loop and denote by Y the product of all the Yukawa couplings entering the diagram (a). The relevant amplitude reads

$$i\mathcal{M} = Y\int \frac{d^4\ell}{(2\pi)^4}\overline{u}(q)P_L\frac{i}{\not p-\not\ell-m}P_R u(p)\frac{i}{\ell^2-M_1^2}\frac{i}{(\ell-k)^2-M_1^2}\Big(\frac{i(2\ell-k)\cdot\epsilon(k)}{(\ell-k)^2-M_2^2}\Big) \tag{IV.24}$$

$$= Y\overline{u}(q)\gamma^\alpha P_R u(p)\int\frac{d^4\ell}{(2\pi)^4}\frac{(p^\alpha-\ell^\alpha)\ell\cdot\epsilon(k)}{(\ell^2-M_1^2)((\ell-k)^2-M_1^2)((\ell-k)^2-M_2^2)((p-\ell)^2-m^2)}\,, \tag{IV.25}$$

where m is the mass of the internal quark and $M_{1,2}$ the masses of $\Delta_{1,2}$. Since the Δ_i live at much higher scales than those probed by the EDM we can assume $M_{1,2}^2 \gg k^2, p^2, m^2$. The integrand is dominated by $\ell^2 \sim M_{1,2}^2$, thus one can expand the propagators as

$$\frac{1}{(\ell-k)^2-M_1^2} \simeq \frac{1}{\ell^2-M_1^2}\Big[1+2\frac{\ell\cdot k}{\ell^2-M_1^2}+4\frac{(\ell\cdot k)^2}{(\ell^2-M_1^2)^2}\Big]\,, \tag{IV.26}$$

with analogous expressions for the other propagators. One obtains

$$i\mathcal{M} = Y\overline{u}(q)\gamma^\alpha P_R u(p)\int\frac{d^4\ell}{(2\pi)^4}$$

$$\frac{(p^\alpha-\ell^\alpha)\ell\cdot\epsilon\Big[1+2\frac{\ell\cdot k}{\ell^2-M_1^2}+4\frac{(\ell\cdot k)^2}{(\ell^2-M_1^2)^2}\Big]\Big[1+2\frac{\ell\cdot k}{\ell^2-M_2^2}+4\frac{(\ell\cdot k)^2}{(\ell^2-M_2^2)^2}\Big]}{\ell^2(l^2-M_1^2)^2(\ell^2-M_2^2)}\Big[1+2\frac{\ell\cdot p}{\ell^2}+4\frac{(\ell\cdot p)^2}{\ell^4}\Big] \tag{IV.27}$$

The denominator is now an even function of the loop momentum ℓ, thus we need to focus on terms with an even number of ℓ at numerator. At $\mathcal{O}(\ell^2)$ there are two kinds of terms which might contribute to the nEDM,

- $p^\alpha\,\ell^\mu\,\ell^\beta\,p_\beta\,\epsilon_\mu \sim \ell^2\,p^\alpha\,(p\cdot\epsilon)$,
- $p^\alpha\,\ell^\mu\,\ell^\beta k_\beta\,\epsilon_\mu \sim \ell^2\,p^\alpha\,(k\cdot\epsilon) = 0$,

and as the non-zero one appears also in the diagram with $\Delta_1 \leftrightarrow \Delta_2$ the sum of both contributions to the nEDM would cancel. Let us consider now $\mathcal{O}(\ell^4)$ terms. There are three types of terms which might contribute,

- $\ell^\alpha\,\ell^\mu\,\ell^\beta\,\ell^\gamma\,k_\beta\,k_\gamma\,\epsilon_\mu \sim (\ell^2)^2\Big[\epsilon_\alpha\,k^2+2\,k_\alpha(k\cdot\epsilon)\Big] = 0$,
- $\ell^\alpha\,\ell^\mu\,\ell^\beta\,\ell^\gamma\,p_\beta\,p_\gamma\,\epsilon_\mu \sim (\ell^2)^2\Big[\epsilon_\alpha\,p^2+2\,p_\alpha(p\cdot\epsilon)\Big]$,
- $\ell^\alpha\,\ell^\mu\,\ell^\beta\,\ell^\gamma\,k_\beta\,p_\gamma\,\epsilon_\mu \sim (\ell^2)^2\Big[\epsilon_\alpha(k\cdot p)+p_\alpha(k\cdot\epsilon)+k_\alpha(p\cdot\epsilon)\Big] \sim (\ell^2)^2\,k_\alpha(p\cdot\epsilon)$.

The second term appears also in the diagram with $\Delta_1 \leftrightarrow \Delta_2$ with coefficient Y^* and therefore cancels. The third doesn't provide a non-zero nEDM. However, the surviving contribution stems from an integral with a $1/(\ell^2-M_1^2)^2(\ell^2-M_2^2)^2$ factor and is canceled by the couple of conjugate diagrams with $\Delta_{1,2}$ exchanged. We have therefore argued that our model allows new physics contributions to the nEDM to occur only starting at the three loop level, which is a statement we have carefully checked by a full 2-loop computation without expanding any propagator.

IV.5.3 Flavor constraints

Flavor changing neutral current (FCNC) observables are expected to set powerful constraints on BSM models, due to the non trivial flavor structure that they imply in order to comply with experimental data. In our scenario, $\Delta F = 2$ processes are prohibited at tree level due to the antisymmetric couplings of Δ with the diquarks, which can be parametrized as $y_{ij} = \epsilon_{ijk} y_k$. These bounds were firstly discussed by the authors of [157] and one can identify our state Δ with the diquark denoted as $VIII$ there. It has to be pointed out that the most general flavor structure, with all the flavor off-diagonal couplings switched on, is not needed to account for baryogenesis, as a single non-zero complex coupling is sufficient to provide a physical CP violating phase. In this setup flavor bounds would be evaded completely.

If one wants to stick to the general scenario, bounds coming from the mixing of neutral the K and $B_{d,s}$ mesons have to be taken into account.

The scalars Δ_i generate a four-fermion effective Hamiltonian given by

$$H_{\rm eff}^{\rm NP}(\Delta F = 2) = \frac{1}{32\pi^2}\left(\frac{\lambda_i \lambda_j^*}{M_\Delta^2}\right) G\left(\frac{m_k^2}{M_\Delta^2}\right)(\overline{q_i}\,\gamma^\mu P_R q_j)\,(\overline{q_i}\gamma_\mu P_R\, q_j)\,, \tag{IV.28}$$

where i and j are the external quark flavor indices, $k \neq i \neq j$ is the flavor index of the internal quark, color indices are contracted within the brackets and the loop function G is given by

$$G(x) = \frac{1 - x^2 + 2\,x\,\log x}{(1-x)^3}\,. \tag{IV.29}$$

Bounds on representative $D = 6$ effective operators contributing to $\Delta F = 2$ transitions have been obtained by the UTfit collaboration [158], from a combination of CP conserving and CP violating observables. We can apply these bounds to our model, and we summarize the results in Table IV.1.

Other constraints which we include are those associated to the $\Delta F = 1$ processes $b \to s\gamma$, $b \to d\gamma$, R_b and $B^\pm \to \phi\pi^\pm$. We refer to [157] for more details as the constraints reported there can be easily translated to our notation. One can note that even the most constraining observable, namely ϵ_k, is compatible with Δ diquark couplings of $\mathcal{O}(0.01)$ around the TeV scale, which, in the absence of major hierarchies in the Yukawa couplings, is the benchmark for our baryogenesis mechanism to work. Therefore, we don't expect flavor physics to exclude values of M_Δ left allowed by collider searches. In fact, even assuming a hierarchy of the type $y_{ui} \gg y_{di}$, in order to lower the bound on M_Δ from colliders, one would get at the same time weaker bounds from flavor.

IV.6 Results

We show the available parameter space in the $v_\phi - c_{\rm vac}$ plane in Fig. IV.2. We have chosen illustrative values for the Yukawa coupling y, allowing us to extend the parameter space by many orders of magnitude towards smaller values of v_ϕ with respect to the analogous model where the PT is instead weakly coupled, as can be seen by comparing with Figure 6 of [72]. This is because the most constraining bound on M_Δ in the scenario considered by the authors of [72] comes from the washout given by inverse decay of Δ, whose rate

Observable	Bound/(M_Δ/TeV)
ϵ_K	$\lvert\text{Im}(y_1 y_2^*)\rvert \leq 7.8 \times 10^{-4}$
Δm_K	$\lvert\text{Re}(y_1 y_2^*)\rvert \leq 1.4 \times 10^{-2}$
B_d mixing	$\lvert y_1 y_3^*\rvert \leq 1.7 \times 10^{-2}$
B_s mixing	$\lvert y_2 y_3^*\rvert \leq 5.8 \times 10^{-2}$
$b \to s\gamma$	$\lvert y_2 y_3^*\rvert \leq 2.5$
$b \to d\gamma$	$\lvert y_1 y_3^*\rvert \leq 1.2$
R_b	$\lvert y_{1,2}\rvert \leq 24$
$B^\pm \to \phi\pi^\pm$	$\lvert y_1 y_3^*\rvert \leq 3.6 \times 10^{-3}$

Table IV.1: *Bounds in units of M/TeV on antisymmetrically coupled diquarks, taken from [157].*

strongly depends on M_Δ because of the Boltzmann factor. In our scenario, due to the presence of a confining sector, we generally expect $M_\Delta \simeq 4\pi v_\phi$, hence the constraint becomes weaker.

It is interesting to understand how the parameter space is affected by the choice of the benchmark values of y and T_n/v_ϕ. One can see that decreasing y has the advantage of decreasing the role played by washout effects, but has the drawback of requiring larger values of $g_{TC}\text{Br}(\text{had} \to \Delta)$ to generate the observed BAU, as the average baryon asymmetry ϵ_Δ gets reduced as well. By modifying the choice of T_n/v_ϕ instead, one is varying the expansion regime of the bubble across the parameter space. A smaller value of T_n/v_ϕ makes the relativistic condition more easily satisfied, but implies a larger entropy dilution, therefore an excessive amount of supercooling would close the parameter space. Therefore the allowed parameter space shown in Fig. IV.2 is close to the maximal one compatible with our baryogenesis mechanism.

In Fig. IV.3 we display the gravitational wave spectrum $\Omega_\text{GW}h^2$ for two different benchmark points, by using the methods described in Sec. I.5. As shown also in Fig. IV.2, LISA and ET will be able to test almost all the theoretically possible parameter space.

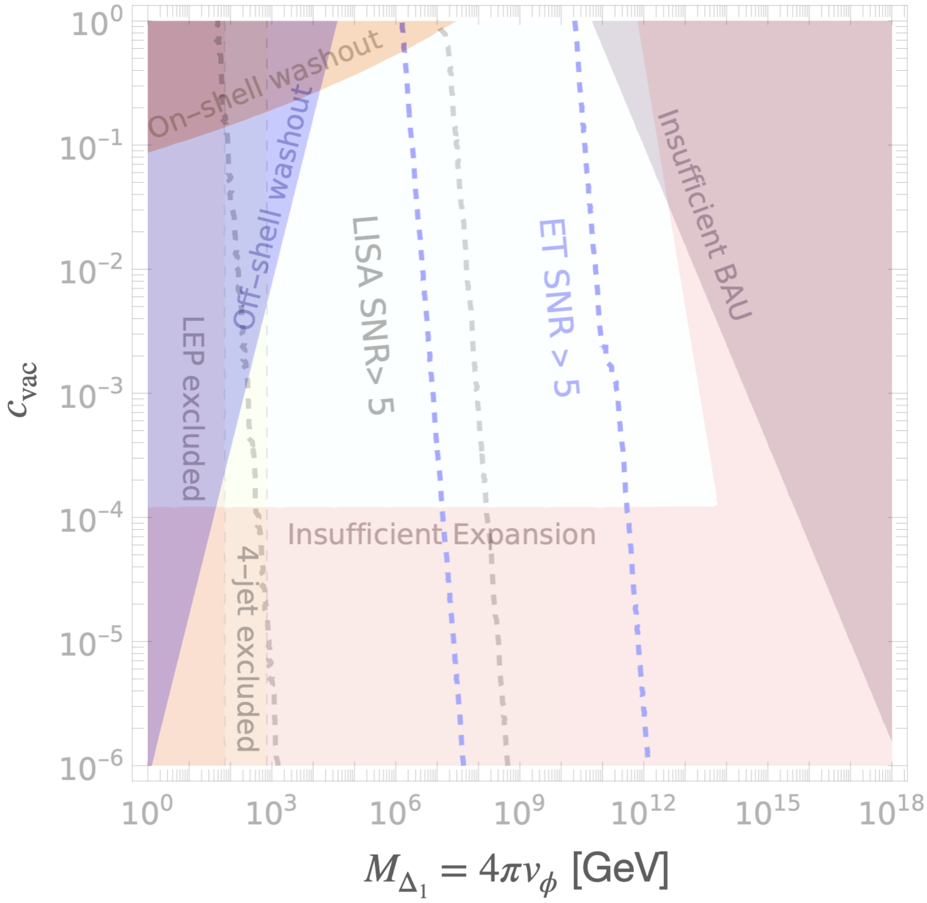

Figure IV.2: *Constraints on the parameter space for the mechanism of baryogenesis from supercooled confinement, for* $M_{\Delta 2}/M_{\Delta 1} = 1.5$*,* $y = 0.01$*,* $T_{\rm n}/v_\phi = 10^{-3}$*. The white area is not constrained and the condition to reproduce the observed baryon asymmetry is imposed on the entire plot, fixing one relation among the free parameters. A value of* y *smaller than unity is needed to avoid washout. Off-shell and on-shell washout regions come from Eq.* (IV.16) *and Eq.* (IV.17)*, while the bottom region is associated to* $\gamma > M_\Delta/T_{\rm n}$*. The pink region at the bottom corresponds to the ping-pong regime in [55], where the quanta of* Δ *are not sufficiently boosted to enter the bubbles, hence they get reflected by walls at each scattering. The excluded region on the right features values of* $g_{\rm TC}{\rm Br}\big(had \to \Delta\big) > 10$*, chosen as a benchmark upper limit, hence it cannot account for the whole baryon asymmetry of the Universe (Insufficient BAU). Constraints from colliders include LEP searches, excluding values of* $M_\Delta < 75$ *GeV and four-jet searches performed at Tevatron and at the LHC, excluding* Δ *in the* 50 *GeV* $< M_\Delta <$ 770 *GeV range. Using the expected bulk properties of the phase transition, with* $\alpha = 100$*,* $\beta/H = 20$*, we show the parameter space testable by the Einstein Telescope and by LISA, which is the region delimited by the blue and grey dashed lines respectively. The astrophysical foregrounds have been taken into account.*

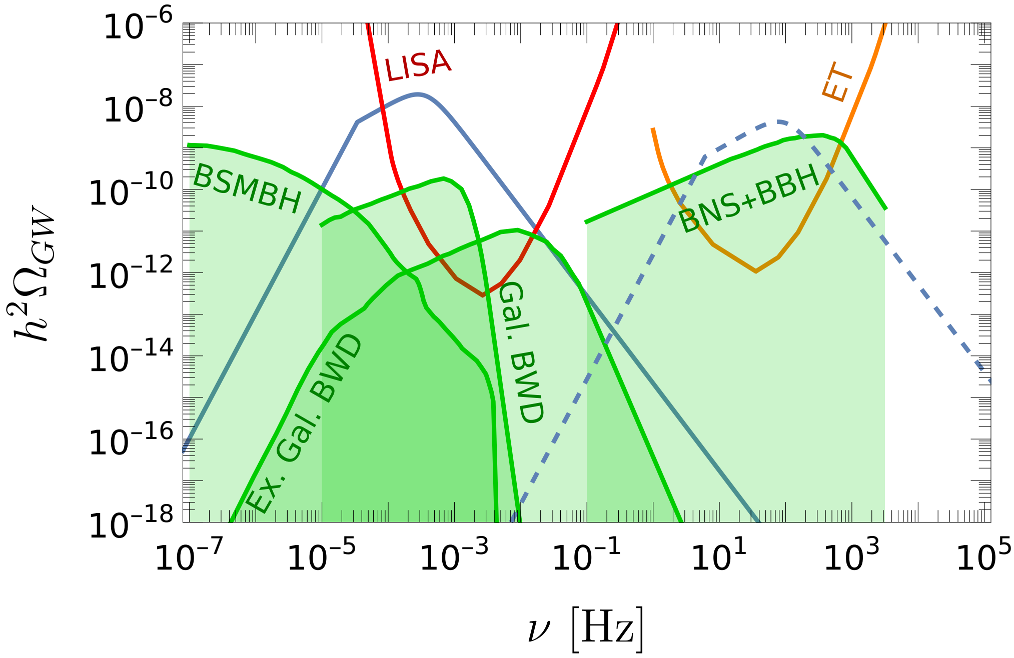

Figure IV.3: *Example of GW spectra for two benchmark points of the parameter space. The dashed (solid) blue line shows the predicted gravitational wave spectrum for the PT in the runaway (terminal velocity) regime, with* $\{c_{\text{vac}}, f\} = \{10^{-2}, 10^4 \text{ GeV}\}$ *in the terminal velocity and* $\{c_{\text{vac}}, f\} = \{10^{-1}, 10^9 \text{ GeV}\}$ *in the runaway. We have assumed* $T_{\text{n}}/v_\phi = 10^{-3}$, $\alpha = 100$ *and* $\beta/H = 20$*. The spectra are compared with power law integrated sensitivity curves, with signal-to-noise ratio SNR=5 for LISA the and the Einstein Telescope (ET). Estimated astrophysical foregrounds from binary super-massive black holes [136], galactic white-dwarf binaries [140], extragalactic white-dwarf binaries [159], binary black holes and neutron stars [128] are also shown.*

Conclusion and Outlook

The nature of dark matter (DM) and the origin of the baryon asymmetry of the universe (BAU) are two of the outstanding mysteries of (astro)particle physics and cosmology. First order phase transitions (FOPTs) in the early universe are predicted by many theories beyond the standard model (SM), they can be used to generate DM and, due to being an out-of-equilibrium process, can serve as a framework for baryogenesis mechanisms. They have attracted a lot of interest in recent years because they can generate gravitational waves (GWs) observable by foreseen experiments and, optimistically, potentially have already been observed in June 2023 by pulsar timing arrays (PTAs) [10–12]. In this thesis we have built new models connecting FOPTs with DM and with the BAU. These models allow to experimentally test these mysteries in novel ways, and connect them with recent and foreseen GW data. In addition, we have presented the first systematic study of the interactions of particle shells at the walls of FOPTs, determining the regions where they free-stream, and paving the way for future studies of their evolution which will have implications ranging from particle production to GWs predictions.

In chapter I of this thesis we summarized the state of the art on FOPTs and their associated GW signal. We described how bubbles, regions where the universe has tunneled to the true vacuum, nucleate. The radius of the bubble will then increase driven by pressure, and the wall, the boundary of the bubble, will expand with ultra-relativistic velocities. The expansion accelerates with growing size of the bubble, but may be stopped due to pressure coming from particles interacting at the wall. Nevertheless, the terminal velocity can become very large as can be seen from Eq. (I.26). Particles in the bath interacting with the wall are destined to accumulate in a thin, dense region at the wall, the shell. We have considered several models, all giving rise to shells, however with different thickness of the shell, average energy, and multiplicity. They also vary by whether the particles accumulate in front of the wall (outside the bubble in the symmetric phase) or behind the wall (inside the bubble in the broken phase). We have listed the properties of different models in Tab. I.1. At the end of this chapter we concluded with the calculation of the GW signal, detecable by GW telescopes and PTAs.

In chapter II we undertook the first general categorization of all interactions we thought of that could possibly modify the evolution of these particles from their point of interaction with the wall until collision with the particles from neighboring bubbles. These effects include both particles from the shell and from the bath potentially flipping momentum at collision with the ultra-relativistic wall, dissipation effects of the shell particles, Bose enhancement or effects from the breakdown of perturbativity leading to large phase space distribution functions, and number changing interactions of the particles in the shell with themselves and with the thermal bath. We computed their size, and therefore were able to determine the model-dependent region in parameter space for which one can safely neglect these effects and where particle shells free-stream.

Note that for computing these effects we have performed the first known to us computation of integrated scattering amplitudes for 3 → 2 processes, whose results we have presented in tables II.2,II.3,II.4,II.5. We show the regions of free-streaming in figures II.2,II.3,II.4,II.5,II.6. We find for all of these effects that they become important for smaller values of the scale of the PT, unless one goes to smaller values of the gauge coupling g. We also find that non-abelian theories give rise to effective interactions in larger regions of parameter space, obviously due to allowing additional self interaction between the gauge bosons.

In chapter III we proposed a novel mechanism to realize ultra-high energy particle collisions in the early universe, which relies on collision of shells created during a cosmological FOPT. Since these bubbles expand with ultra-relativistic walls, collisions between different bubbles happen with large scattering energies which can not only be used to generate dark matter but any heavy new state. We dubbed this novel mechanism the bubbletron. We investigated several scenarios and computed the key parameters to compute the Yield and energy of produced particles via the bubbletron mechanism. The general formula for the Yield of a bubbletron is given in Eq. (III.8). We then gave a practical realization of a bubbletron by identifying the heavy state with a DM candidate and computed the maximal possible DM mass. We show our findings in Fig. III.4, where we have considered shells produced by U(1) gauge bosons. We used an abelian theory because this allows us to assume free-streaming for a larger parameter space, and therefore extending the allowed region to lower values of the scale of the PT. We find that one can produce heavy DM with masses above 10^3 TeV for scales of the PT of around 10 MeV, and with masses above the GUT scale for scales of the PT above about 10^9 GeV. As can be seen in Fig. III.5, FOPTs of these scales lie in the observable range of future GW telescopes like LISA and ET. Intriguingly, this could link the GW signal recently observed at PTAs with DM up to the PeV scale.

More in general, our study realizes a new connection between primordial GW signals and physics at energy scales otherwise inaccessible not only in the laboratory but, so far, also in the early universe. In the example of heavy DM, these GW could be accompanied by high energy cosmic rays from decays of DM, if unstable.

In chapter IV we used a supercooled confining PT to create the heavy scalars of a confining sector, which due to their interactions being C, CP, and B violating can be used to realize baryogenesis. We found that, compared to analogous scenarios considered in previous literature, the confining nature of the PT opens up the allowed parameter space down to EW scales. This allows for testing our model with EW scale experiments, leading to non-astrophysical constraints, as well as to GW signals at LISA. We evaluated bounds from several observables, including searches at colliders, the electric dipole moment of the neutron, and from flavor-violating processes. We show the region allowing to have baryogenesis in Fig. IV.2. Again, as can be seen from Fig. IV.3 we find that due to the low value of the scale of the PT this signal could be observed by LISA and Einstein Telescope in the future.

We finally come to possible future directions. In this thesis we have laid the groundwork for categorizing and computing free-streaming effects affecting the evolution of particles from their point of interaction with the wall until the collision with particles from other bubbles. This is not only interesting and relevant for the described bubbletron, but also for the correct computation of the GW signal, since also the amplitude of GWs could be affected by interacting shells. In particular for the number changing interactions we could and should improve our calculation by fully computing the thermal average, without the assumption of factorization of thermal integrals. This would enable us to write down and solve Boltzmann equations, even if only numerically, for the evolution of number densities and average energies. We could then use these results to extend any computation we did in this paper to the region in parameter space we have so far excluded due to our ignorance about what happens beyond free-streaming. What we have computed in this thesis will be important for this endeavor as it will guide us towards the particular free-streaming process which is dominant and which we should focus on calculating with higher precision.

Concerning more specifically bubbletrons, future avenues of exploration include bubbletrons other than those induced by radiated reflected particles, or in the region where shells do not free-stream, and other applications for baryogenesis and possible trans-Planckian scatterings in the early universe. Finally concerning baryogenesis from first order PTs, having demonstrated that confinement allows extending the parameter space down to the EW scale, it could be interesting to study a model with sterile composite neutrinos, to determine whether this mechanism makes leptogenesis testable at future colliders.

Acknowledgements

I am forever indebted to Filippo Sala for his constant support, his passionate way of doing physics and his mentoring during the last three years. I have learned a lot, not purely related to physics, during the last three years, which without him and his amazing style of supervision would have been impossible. I am especially grateful for his patience with me, and pushing me with his seemingly endless energy. I also wish to thank Marco Cirelli for his tiredless assisting in the bureaucratic process related to this thesis, and for his contribution to the very joyful atmosphere during our times together. I am also glad to have worked with Filippo, Yann, Iason, Jacopo, and Silvia. Not only have you made the discussions during our collaborations fruitful and interesting, but also very enjoyable. I also want to deeply thank all the people at LPTHE and at UNIBO for the welcoming environment. You certainly made my time very special and I enjoyed spending my time with you. Finally I want to thank the members of the jury for accepting to be a part of the committee, and for taking the time to read this thesis.

A – Final phase space integration

In this appendix we describe the algorithm used to perform the final phase space integral of the 3 → 2 scattering amplitudes.

The most complicated expression of scalar products in the denominator is one that comes from interference terms. One 5-point amplitude, consisting of only 3-point or 4-point interactions, contains at most two denominators from propagators, which are different from each other. In an interference term this would be multiplied by two more denominators, all possibly different. Therefore, we should be able to compute terms with at least 4 different denominators, e.g.

$$|\mathcal{M}|^2 \supset \frac{1}{s_{13}^a s_{24}^b} \cdot \frac{1}{s_{23}^c s_{54}^d} \,. \tag{A.1}$$

One possible approach to recast that integral is the method of Feynman parameters. In loop-computations one usually completes the square to get rid of the linear terms, and then performs the loop integration. Here the approach would be to perform a $SO(3)$ rotation to get rid of any azimuthal angle in the denominator, such that the integral over the polar angle can be performed. After doing so one ends up with an integral over 3 Feynman parameters. However, these integrals are not textbook integrals and evaluating them efficiently or at all is not guaranteed.

In the following we will therefore describe an algorithm which is able to perform the final phase space integration for all possible amplitudes.

A.1 Partial fraction decomposition of scalar products

We start from the following expression,

$$|\mathcal{M}|^2 = \sum_n \mathcal{C}_n \; \frac{\prod s_{ij}^k}{s_{13}^a s_{14}^b s_{23}^c s_{24}^d s_{53}^e s_{54}^f} \,. \tag{A.2}$$

We can have either combination of s_{12}, s_{15}, s_{25}, s_{34} in the amplitude, but these do not depend on the final phase space integration. Therefore, we absorb them into the prefactors $\mathcal{C}_n$.

The next step is to reduce the numbers of different factors in the denominator. We achieve this by the method of partial fraction decomposition and exploiting energy momentum conservation. This can be achieved systematically the easiest way by multiplying with a non-trivial representation of the identity.

We derive this identity by writing energy momentum conservation in the following way,

$$p_k \cdot (p_1 + p_2 + p_5 - p_3 - p_4) = 0\,, \tag{A.3}$$

which represents five independent equations for $k = 1, 2, 3, 4, 5$. We find, for example for $k = 1$,

$$p_1 \cdot p_1 + p_1 \cdot p_2 + p_1 \cdot p_5 = p_1 \cdot p_3 + p_1 \cdot p_4\,, \tag{A.4}$$

or equivalently

$$s_{12} + s_{15} - 2m_1^2 - m_2^2 - m_5^2 - m_3^2 - m_4^2 = -s_{13} - s_{14}\,. \tag{A.5}$$

Performing this manipulation for all k we find several equations for the identity,

$$1 = \frac{s_{13} + s_{14}}{\mathcal{C}_1}\,, \tag{A.6}$$

$$1 = \frac{s_{23} + s_{24}}{\mathcal{C}_2}\,, \tag{A.7}$$

$$1 = \frac{s_{53} + s_{54}}{\mathcal{C}_5}\,, \tag{A.8}$$

$$1 = \frac{s_{13} + s_{23} + s_{53}}{\mathcal{C}_3}\,, \tag{A.9}$$

$$1 = \frac{s_{14} + s_{24} + s_{54}}{\mathcal{C}_4}\,, \tag{A.10}$$

where the constants $\mathcal{C}_k$ do not dependent on the final phase space integration.

More relevant identities, which can be derived in similar fashion, are

$$1 = \frac{s_{14} + s_{23} + s_{53}}{\mathcal{C}_{14}}\,, \tag{A.11}$$

$$1 = \frac{s_{13} + s_{24} + s_{54}}{\mathcal{C}_{13}}\,, \tag{A.12}$$

$$1 = \frac{s_{13} + s_{24} + s_{53}}{\mathcal{C}_{24}}\,, \tag{A.13}$$

$$1 = \frac{s_{14} + s_{23} + s_{54}}{\mathcal{C}_{23}}\,, \tag{A.14}$$

$$1 = \frac{s_{13} + s_{23} + s_{54}}{\mathcal{C}_{54}}\,, \tag{A.15}$$

$$1 = \frac{s_{14} + s_{24} + s_{53}}{\mathcal{C}_{53}}\,. \tag{A.16}$$

All $\mathcal{C}$'s are guaranteed to not introduce any additional singularities into the amplitude.

It is straightforward to see that by strategic multiplication with these identities one can step by step reduce the powers of particular denominators up to elimination of some (but not all) of them.

After the full reduction has been completed, we end up with with terms of the structure

$$\mathcal{I}_1 \supset \frac{1}{s_{13}^a}\,, \qquad \mathcal{I}_2 \supset \frac{1}{s_{13}^a s_{24}^b}\,, \qquad \mathcal{I}_3 \supset \frac{s_{13}^m}{s_{53}^a}\,, \tag{A.17}$$

where any 3 can also be a 4 and vice versa.

Note that any terms in the numerator depending on the final phase space integration are present already from the amplitude. There are no additional ones created due to the reduction algorithm.

A.2 Parameterization of the integration region

It is most convenient to evaluate the two-particle final phase space integral in the center-of-mass frame, where after eliminating the delta-distribution ensuring energy momentum conservation we are left with an integral over two angles,

$$R_2((p_3+p_4)^2) = \frac{\mathrm{d}^3p_3}{(2\pi)^3 2E_3}\frac{\mathrm{d}^3p_4}{(2\pi)^3 2E_4}\delta^{(4)}(p_1+p_2+p_5-p_3-p_4) = \frac{\sqrt{\lambda((p_3+p_4)^2, m_3^2, m_4^2)}}{32\pi^2(p_3+p_4)^2}\int \mathrm{d}\Omega \ , \tag{A.18}$$

where $\lambda(x,y,z) = x^2+y^2+z^2-2xy-2yz-2zx$ is the Källén function and $\int \mathrm{d}\Omega$ is the standard integral over the S^2-sphere,

$$\int \mathrm{d}\Omega = \int_0^\pi \mathrm{d}\theta_{13}\sin(\theta_{13})\int_0^{2\pi}\mathrm{d}\varphi_{13} = \int_{-1}^{+1}\mathrm{d}z_{13}\int_0^{2\pi}\mathrm{d}\varphi_{13} \tag{A.19}$$

It is worthy to point out that the final phase space integral is invariant under the exchange of the two momenta of the final states, $p_3 \leftrightarrow p_4$. This is mostly useful for simplifying the amplitude in order to safe computational resources by not calculating the same integral twice, since $p_3 \leftrightarrow p_4$ implies $z_{13} \leftrightarrow -z_{13}$. The integral is also invariant under $O(3)$ rotations on the S^2-sphere, which we will exploit heavily in order to being able to compute some of the integrals.

We now state our choice for the parameterization of the five momenta,

$$p_{1,\mathrm{com}} = \begin{pmatrix} \sqrt{m_1^2+p_I^2} \\ 0 \\ 0 \\ p_I \end{pmatrix} , \ p_{2,\mathrm{com}} = \begin{pmatrix} \sqrt{m_2^2+p_J^2} \\ p_J\sin(\theta_{12}) \\ 0 \\ p_J\cos(\theta_{12}) \end{pmatrix} , \ p_{5,\mathrm{com}} = \begin{pmatrix} \sqrt{m_5^2+p_K^2} \\ -p_J\sin(\theta_{12}) \\ 0 \\ -p_I - p_J\cos(\theta_{12}) \end{pmatrix} , \tag{A.20}$$

$$p_{3,\mathrm{com}} = \begin{pmatrix} \sqrt{m_3^2+p_F^2} \\ p_F\sin(\theta_{13})\cos(\varphi_{13}) \\ p_F\sin(\theta_{13})\sin(\varphi_{13}) \\ p_F \end{pmatrix} , \ p_{4,\mathrm{com}} = \begin{pmatrix} \sqrt{m_4^2+p_F^2} \\ -p_F\sin(\theta_{13})\cos(\varphi_{13}) \\ -p_F\sin(\theta_{13})\sin(\varphi_{13}) \\ -p_F \end{pmatrix} . \tag{A.21}$$

The on-shell condition $p_{5,\mathrm{com}}^2 = m_5^2$ fixes $p_K = \sqrt{p_I^2 + 2p_Ip_J\cos(\theta_{12}) + p_J^2}$. This allows us to replace the angle θ_{12} by the length p_K, which can be interpreted as describing a triangle either by two lengths p_I, p_J and an angle θ_{12}, or by three lenghts p_I, p_J, p_K. This constrains these parameters to the region $p_I \geq 0$, $p_J \geq 0$, $p_K \geq 0$, $p_K \leq p_I + p_J$, $p_K \geq |p_I - p_J|$.

Conservation of energy also fixes p_F via the equation

$$\sqrt{m_1^2+p_I^2}+\sqrt{m_2^2+p_J^2}+\sqrt{m_5^2+p_K^2}=\sqrt{m_3^2+p_F^2}+\sqrt{m_4^2+p_F^2}\,. \tag{A.22}$$

After the integration the result depends only three variables p_I, p_J, p_K. However, we can exploit the Lorentz invariance of the amplitude, and re-express the result in terms of scalar products. This is because $p_1 \cdot p_2 = p_{1,\text{com}} \cdot p_{2,\text{com}}$, etc. defines a solvable system of three coupled algebraic equations which lets us perform the substitution

$$\{p_I, p_J, p_K\} \Rightarrow \{p_{1,\text{com}} \cdot p_{2,\text{com}}, p_{1,\text{com}} \cdot p_{5,\text{com}}, p_{2,\text{com}} \cdot p_{5,\text{com}}\} \Rightarrow \{p_1 \cdot p_2, p_1 \cdot p_5, p_2 \cdot p_5\}\,. \tag{A.23}$$

This trick avoids having to work out the explicit Lorentz transformation from the center-of-mass frame to your favorite frame, since one just computes the three scalar products in the preferred reference frame and subsitutes them into the result.

Note that because of $(p_3+p_4)^2=(p_1+p_2+p_5)^2$ the scalar product $p_3 \cdot p_4$ is not independent. This is consistent with the fact that integration over two integration variables should reduce the number of independent scalar products from five to three.

A.3 Basis integrals

Let us now proceed with the computation of the basis integrals of equation (A.17). For a more transparent notation we are going to replace complicated expressions which do not depend on the final phase space angles with simple variables c_l. Also the well known substitution of integration variable $\cos(\theta_{13}) = z_{13}$ is going to be performed without extra comments.

The analytic integrals have been verified by comparing the results to those of numeric integration.

A.3.1 $\mathcal{I}_1$

Consider the integral

$$\int \mathrm{d}\Omega\, \mathcal{I}_1 \supset \int \mathrm{d}\Omega\ \frac{1}{s_{13}^a} \tag{A.24}$$

$$= \int_{-1}^{+1} \mathrm{d}z_{13} \int_0^{2\pi} \mathrm{d}\varphi_{13}\ \frac{1}{(c_0 + c_1 \cdot z_{13})^a}\,. \tag{A.25}$$

The azimuthal integration evaluates trivially to 2π, and the integration over z_{13} is a textbook integral which evalutes either to a rational function or a logarithm, depending on the value of a.

Now consider an integral of similar structure, but different momentum,

$$\int \mathrm{d}\Omega\, \mathcal{I}_1 \supset \int \mathrm{d}\Omega\ \frac{1}{s_{23}^a} \tag{A.26}$$

$$= \int_0^{\pi} \mathrm{d}\theta_{13} \sin(\theta_{13}) \int_0^{2\pi} \mathrm{d}\varphi_{13}\ \frac{1}{[c_0 + c_2 \cdot \sin(\theta_{13})\cos(\varphi_{13}) + c_1 \cdot \cos(\theta_{13})]^a}\,. \tag{A.27}$$

This integral is now no longer be evaluated quickly. The solution is to exploit the invariance of the final phase space integral under $O(3)$-rotations, and rotate the vectors $p_{3,\text{com}}$, $p_{4,\text{com}}$ by an angle such that they are aligned with the direction of $p_{2,\text{com}}$. Note that because of the linearity of the integral one has to apply this rotation only to this term, not to all the others. However, scalar products in the same term are invariant under rotations, since they are part of the Lorentz group, and therefore we do not need to perform any transformations an scalar products independent of $p_{3,\text{com}}$ and $p_{4,\text{com}}$.

Therefore, the method of integrating structures of type $\mathcal{I}_1$ is performing an appropriate $O(3)$ rotation, and then evaluating the integral over a rational function.

A.3.2 $\mathcal{I}_2$

Consider the integral

$$\int \mathrm{d}\Omega\, \mathcal{I}_2 \supset \int \mathrm{d}\Omega\ \frac{1}{s_{23}^a s_{54}^b}\,. \tag{A.28}$$

One possible way to proceed would be to perform a partial fraction decomposition with respect to the variable z_{13}, and then apply different $O(3)$ rotations to the different terms.

However, an easier way is Feynman parameterization, which is also easier to implement as a generally applicable algorithm. For two denominators we have

$$\frac{1}{A^a B^b} = \frac{\Gamma(a+b)}{\Gamma(a)\Gamma(b)} \int_0^1 \mathrm{d}x\, \frac{x^{a-1}\bar{x}^{b-1}}{(xA+\bar{x}B)^{a+b}}\,, \quad \bar{x} = 1-x\,, \tag{A.29}$$

Then for above example we have

$$\begin{aligned} xA + \bar{x}B &= c_0' - 2(xE_2E_3 + \bar{x}E_5E_4) + 2(x\ \vec{p}_2\cdot\vec{p}_3 + \bar{x}\ \vec{p}_5\cdot\vec{p}_4) && \text{(A.30)}\\ &= c_0(x) + 2(x\vec{p}_2 - \bar{x}\vec{p}_5)\cdot\vec{p}_3 && \text{(A.31)} \end{aligned}$$

where $E_k = p^0_{k,\text{com}}$ are the energies in the center-of-mass frame, and for readability we omitted the index com indicating the evaluation in the center-of-mass frame. In the last step we used that $p_{3,\text{com}} = -p_{4,\text{com}}$.

In order to evaluate the integral over the azimuthal and polar angle we make again use of the invariance under $O(3)$-rotations and rotate in such a way that the vector $\vec{p}_3$ is parallel to the vector $x\vec{p}_2 + \bar{x}\vec{p}_5$. We can then write the scalar product as

$$2(x\vec{p}_2 - \bar{x}\vec{p}_5)\cdot\vec{p}_3 = 2|x\vec{p}_2 - \bar{x}\vec{p}_5||\vec{p}_3|\cos(\theta_{13})\,, \tag{A.32}$$

such that the integral over $\mathcal{I}_2$ reduces to

$$\begin{aligned} \int \mathrm{d}\Omega\, \mathcal{I}_2 \supset \int \mathrm{d}\Omega\ \frac{1}{s_{23}^a s_{54}^b} && \text{(A.33)}\\ = \frac{\Gamma(a+b)}{\Gamma(a)\Gamma(b)} \int_0^1 \mathrm{d}x \int_{-1}^{+1} \mathrm{d}z_{13} \int_0^{2\pi} \mathrm{d}\varphi_{13}\ \frac{x^{a-1}\bar{x}^{b-1}}{[c_0(x) + c_1(x)z_{13}]^{a+b}}\,. && \text{(A.34)} \end{aligned}$$

The integration over the azimuthal angle φ_{13} evaluates trivially to 2π. Since this expression only appears for at least denominators, i.e. $a \geq 1$, $b \geq 1$, we have $a + b \geq 2$.

Therefore, performing the integral over the polar angle z_{13} is never going to yield a logarithm. It even turns out that, while the length of a vector contains a square root of the Feynman parameter x, the integral onle depends on the length squared, and therefore we are left with an integral of the form

$$\int_0^1 \mathrm{d}x \ \frac{\sum_{i=0}^{k-1} a_i x^i}{\left(b_0 + b_1 \cdot x + b_2 \cdot x^2\right)^k} \,. \tag{A.35}$$

This is a well known class of textbook integrals, and can be easily computed, for example with the method of partial fraction decomposition, or Mathematica.

Therefore, the method of integrating structures of type $\mathcal{I}_2$ is a combination of applying Feynman parameters and performing an appropriate $O(3)$ rotation.

A.3.3 $\mathcal{I}_3$

Consider the integral

$$\int \mathrm{d}\Omega\, \mathcal{I}_3 \supset \int \mathrm{d}\Omega \ \frac{s_{23}^m}{s_{53}^a} \,. \tag{A.36}$$

From the expressions before we have already seen that it is most convenient to eliminate any azimuthal angle φ_{13} in the denominator. We achieve this as before by rotating $p_{3,\mathrm{com}}$ in a suitable way.

However, now the numerator is not independent of $p_{3,\mathrm{com}}$ and will be affected by the rotation. This is easily done by acting on the vector $\vec{p}_3$ with the standard rotation matrix $\mathcal{R}_3$. Since one can in general not choose the matrix $\mathcal{R}_3$ in such a way that any dependence on φ_{13} disappears, we still have φ_{13} in the numerator. Therefore, we have

$$\int \mathrm{d}\Omega\, \mathcal{I}_3 \supset \int_0^{\pi} \mathrm{d}\theta_{13} \sin(\theta_{13}) \int_0^{2\pi} \mathrm{d}\varphi_{13} \ \frac{\left[d_0 + d_2 \cdot \sin(\theta_{13}) \cos(\varphi_{13}) + d_1 \cdot \cos(\theta_{13})\right]^m}{\left[c_0 + c_1 \cdot \cos(\theta_{13})\right]^a} \tag{A.37}$$

We perform the integration over the azimuthal angle φ_{13} first. When we expand the numerator, we get a series with terms proportional to

$$\int_0^{2\pi} \mathrm{d}\varphi_{13} \ \left[\sin(\theta_{13}) \cos(\varphi_{13})\right]^k \,. \tag{A.38}$$

This is integral vanishes for all odd powers of k. This is in so far convenient that keeping only the even powers eliminates all occurences of $\sin(\theta_{13}) = \sqrt{1 - z_{13}^2}$, which is not straightforward to integrate in general. Therefore after performing the azimuthal integration we are left with the integration over the polar angle, which takes the form

$$\int_{-1}^{+1} \mathrm{d}z_{13} \ \frac{\sum_m a_m z_{13}^m}{\left[c_0 + c_1 \cdot z_{13}\right]^a} \,. \tag{A.39}$$

As in the previous subsection, this is a well known class of textbook integrals, and can be easily computed, for example with the method of partial fraction decomposition, or Mathematica.

Therefore, the method of integrating structures of type $\mathcal{I}_3$ is performing an appropriate $O(3)$ rotation and then proceeding with the integration over the angles as described above.

A.4 Summary

We have outlined an algorithm how to compute the final phase space integration over any amplitude describing a $3 \to 2$ process. The result is, although the integration was performed in a specific frame, still Lorentz invariant, and can therefore be expressed in terms of three independent scalar products $p_1 \cdot p_2$, $p_1 \cdot p_5$, and $p_2 \cdot p_5$.

B – Final state momentum configuration

In this appendix we achieve a better understanding of the momentum configuration of the two particles in the final state. We find that for both bath-shell-shell and bath-bath-shell there will be one particle behaving parameterically as a shell particle and the other one as a bath particle.

Consider the momentum configuration in the wall frame ($f = m_{c,h}, \ldots$)

$$p_{1,w} = \begin{pmatrix} f \\ 0 \\ 0 \\ f \end{pmatrix} , \quad p_{2,w} = \begin{pmatrix} \gamma T_\mathrm{n} \\ 0 \\ 0 \\ -\gamma T_\mathrm{n} \end{pmatrix} , \quad p_{5,w} = \begin{pmatrix} \gamma T_\mathrm{n} \\ 0 \\ 0 \\ -\gamma T_\mathrm{n} \end{pmatrix} , \tag{B.1}$$

$$p_{3,w} = \begin{pmatrix} E_3 \\ E_3 \sin(\theta_{3,w}) \\ 0 \\ E_3 \cos(\theta_{3,w}) \end{pmatrix} , \quad p_{4,w} = \begin{pmatrix} E_4 \\ E_4 \sin(\theta_{4,w}) \\ 0 \\ E_4 \cos(\theta_{4,w}) \end{pmatrix} , \tag{B.2}$$

corresponding to the scenario bath-bath-shell. Without loss of generality, this scattering happens in the $x - z$-plane. If we were to introduce some spread, the scattering is in general 3-dimensional and this discussion becomes less illuminating, but the message stays unaffected.

We can then use energy-momentum-conservation to read of the following equations

$$E_3 \sin(\theta_{3,w}) = E_4 \sin(\theta_{4,w}) \,, \tag{B.3}$$

$$f + 2\gamma T_\mathrm{n} = E_3 + E_4 \,, \tag{B.4}$$

$$f - 2\gamma T_\mathrm{n} = E_3 \cos(\theta_{3,w}) + E_4 \cos(\theta_{4,w}) \,. \tag{B.5}$$

Another important condition is the on-shell condition,

$$0 \lesssim (E_4)^2 - (E_4 \sin(\theta_{4,w}))^2 - (E_4 \cos(\theta_{4,w}))^2 \tag{B.6}$$

$$= (f + 2\gamma T_\mathrm{n} - E_3)^2 - (E_3 \sin(\theta_{3,w}))^2 - (f - 2\gamma T_\mathrm{n} - E_3 \cos(\theta_{3,w}))^2 \tag{B.7}$$

$$= 8 f \gamma T_\mathrm{n} - 2 f E_3 (1 - \cos(\theta_{3,w})) - 2\gamma T_\mathrm{n} E_3 (1 + \cos(\theta_{3,w})) \,. \tag{B.8}$$

Since the thermal mass can be neglected in these types of discussions, this equation fixes the energy as a function of the angle,

$$E_{3,w} \lesssim \frac{8f\gamma T_{\rm n}}{2f(1-\cos(\theta_{3,w})) + 2\gamma T_{\rm n}(1+\cos(\theta_{3,w}))} \tag{B.9}$$

$$= \begin{cases} 2f & \theta_{3,w} = 0 \\ \dfrac{4f\gamma T_{\rm n}}{f+\gamma T_{\rm n}} & \theta_{3,w} = \pi/2 \\ 2\gamma T_{\rm n} & \theta_{3,w} = \pi \end{cases} . \tag{B.10}$$

Remark the following,

$$E_3(\theta_{3,w} = \pi/2) \simeq 4\gamma T_{\rm n} \tag{B.11}$$

$$\overset{!}{=} f + 2\gamma T_{nuc} - E_4 \simeq 2\gamma T_{\rm n} - E_4 \,. \tag{B.12}$$

This is a condition which is impossible to satisfy, since $E_4 \geq 0$. We conclude that the scattering must be very collinear. Since the labeling $3 \leftrightarrow 4$ is arbitrary, we define without loss of generality that

$$E_{3,w} \simeq \mathcal{O}(f) \,, \tag{B.13}$$

$$\theta_{3,w} \simeq 0 \,. \tag{B.14}$$

Then energy-momentum-conservation gives

$$E_{4,w} \simeq \mathcal{O}(\gamma T_{\rm n}) \,, \tag{B.15}$$

$$\theta_{4,w} \simeq \pi \,. \tag{B.16}$$

This implies that each scattering does not change direction by much in the wall frame (so even less in the plasma frame!), and the outgoing particle is type ejected ($E_{3,w} \sim f$) and the ingoing is type bath ($E_{4,w} \sim \gamma T_{\rm n}$).

A similar conclusion is achieved for bath-shell-shell type interactions in the same way.

Bibliography

[1] Y. Fukuda et al. “Evidence for oscillation of atmospheric neutrinos”. In: *Phys. Rev. Lett.* 81 (1998), pp. 1562–1567. DOI: `10.1103/PhysRevLett.81.1562`. arXiv: `hep-ex/9807003`.

[2] S. Fukuda et al. “Determination of solar neutrino oscillation parameters using 1496 days of Super-Kamiokande I data”. In: *Phys. Lett. B* 539 (2002), pp. 179–187. DOI: `10.1016/S0370-2693(02)02090-7`. arXiv: `hep-ex/0205075`.

[3] Massimo Persic, Paolo Salucci, and Fulvio Stel. “The Universal rotation curve of spiral galaxies: 1. The Dark matter connection”. In: *Mon. Not. Roy. Astron. Soc.* 281 (1996), p. 27. DOI: `10.1093/mnras/278.1.27`. arXiv: `astro-ph/9506004`.

[4] Douglas Clowe et al. “A direct empirical proof of the existence of dark matter”. In: *Astrophys. J. Lett.* 648 (2006), pp. L109–L113. DOI: `10.1086/508162`. arXiv: `astro-ph/0608407`.

[5] Planck Collaboration et al. “Planck 2018 results. VI. Cosmological parameters”. In: *aap* 641, A6 (Sept. 2020), A6. DOI: `10.1051/0004-6361/201833910`. arXiv: `1807.06209 [astro-ph.CO]`.

[6] A. Arbey and F. Mahmoudi. “Dark matter and the early Universe: a review”. In: *Prog. Part. Nucl. Phys.* 119 (2021), p. 103865. DOI: `10.1016/j.ppnp.2021.103865`. arXiv: `2104.11488 [hep-ph]`.

[7] Dietrich Bodeker and Wilfried Buchmuller. “Baryogenesis from the weak scale to the grand unification scale”. In: *Rev. Mod. Phys.* 93.3 (2021), p. 035004. DOI: `10.1103/RevModPhys.93.035004`. arXiv: `2009.07294 [hep-ph]`.

[8] John F. Donoghue, Eugene Golowich, and Barry R. Holstein. *Dynamics of the Standard Model : Second edition*. Vol. 2. Oxford University Press, 2014. ISBN: 978-1-00-929103-3, 978-1-00-929100-2, 978-1-00-929101-9. DOI: `10.1017/9781009291033`.

[9] Djuna Croon, Tomás E. Gonzalo, Lukas Graf, Nejc Košnik, and Graham White. “GUT Physics in the era of the LHC”. In: *Front. in Phys.* 7 (2019), p. 76. DOI: `10.3389/fphy.2019.00076`. arXiv: `1903.04977 [hep-ph]`.

[10] Nihan S. Pol et al. “Astrophysics Milestones for Pulsar Timing Array Gravitational-wave Detection”. In: *Astrophys. J. Lett.* 911.2 (2021), p. L34. DOI: `10.3847/2041-8213/abf2c9`. arXiv: `2010.11950 [astro-ph.HE]`.

[11] Gabriella Agazie et al. “The NANOGrav 15 yr Data Set: Evidence for a Gravitational-wave Background”. In: *Astrophys. J. Lett.* 951.1 (2023), p. L8. DOI: `10.3847/2041-8213/acdac6`. arXiv: `2306.16213 [astro-ph.HE]`.

[12] J. Antoniadis et al. “The second data release from the European Pulsar Timing Array III. Search for gravitational wave signals”. In: (June 2023). arXiv: `2306.16214 [astro-ph.HE]`.

[13] K. Kajantie, M. Laine, K. Rummukainen, and Mikhail E. Shaposhnikov. “Is there a hot electroweak phase transition at $m_H \gtrsim m_W$?” In: *Phys. Rev. Lett.* 77 (1996), pp. 2887–2890. DOI: `10.1103/PhysRevLett.77.2887`. arXiv: `hep-ph/9605288`.

[14] Iason Baldes, Maximilian Dichtl, Yann Gouttenoire, and Filippo Sala. “*to appear:* Particle shells from fast bubble walls”. In: (Sept. 2023). arXiv: `2309.XXXXX [hep-ph]`.

[15] Iason Baldes, Maximilian Dichtl, Yann Gouttenoire, and Filippo Sala. “Bubbletrons”. In: (June 2023). arXiv: `2306.15555 [hep-ph]`.

[16] Kim Griest and Marc Kamionkowski. “Unitarity limits on the mass and radius of dark-matter particles”. In: *Phys. Rev. Lett.* 64 (6 1990), pp. 615–618. DOI: `10.1103/PhysRevLett.64.615`. URL: `https://link.aps.org/doi/10.1103/PhysRevLett.64.615`.

[17] Maximilian Dichtl, Jacopo Nava, Silvia Pascoli, and Filippo Sala. “*to appear:* Baryogenesis from supercooled confinement”. In: (2023). arXiv: `231Y.XXXXX [hep-ph]`.

[18] Y. Aoki, G. Endrodi, Z. Fodor, S. D. Katz, and K. K. Szabo. “The Order of the quantum chromodynamics transition predicted by the standard model of particle physics”. In: *Nature* 443 (2006), pp. 675–678. DOI: `10.1038/nature05120`. arXiv: `hep-lat/0611014`.

[19] Paolo Creminelli, Alberto Nicolis, and Riccardo Rattazzi. “Holography and the electroweak phase transition”. In: *JHEP* 03 (2002), p. 051. DOI: `10.1088/1126-6708/2002/03/051`. arXiv: `hep-th/0107141`.

[20] Germano Nardini, Mariano Quiros, and Andrea Wulzer. “A Confining Strong First-Order Electroweak Phase Transition”. In: *JHEP* 09 (2007), p. 077. DOI: `10.1088/1126-6708/2007/09/077`. arXiv: `0706.3388 [hep-ph]`.

[21] Thomas Konstandin and Geraldine Servant. “Cosmological Consequences of Nearly Conformal Dynamics at the TeV scale”. In: *JCAP* 1112 (2011), p. 009. DOI: `10.1088/1475-7516/2011/12/009`. arXiv: `1104.4791 [hep-ph]`.

[22] Nathaniel Craig, Noam Levi, Alberto Mariotti, and Diego Redigolo. “Ripples in Spacetime from Broken Supersymmetry”. In: *JHEP* 21 (2020), p. 184. DOI: `10.1007/JHEP02(2021)184`. arXiv: `2011.13949 [hep-ph]`.

[23] Luigi Delle Rose, Giuliano Panico, Michele Redi, and Andrea Tesi. “Gravitational Waves from Supercool Axions”. In: *JHEP* 04 (2020), p. 025. DOI: `10.1007/JHEP04(2020)025`. arXiv: `1912.06139 [hep-ph]`.

[24] Benedict Von Harling, Alex Pomarol, Oriol Pujolàs, and Fabrizio Rompineve. “Peccei-Quinn Phase Transition at LIGO”. In: *JHEP* 04 (2020), p. 195. DOI: `10.1007/JHEP04(2020)195`. arXiv: `1912.07587 [hep-ph]`.

[25] Admir Greljo, Toby Opferkuch, and Ben A. Stefanek. “Gravitational Imprints of Flavor Hierarchies”. In: *Phys. Rev. Lett.* 124.17 (2020), p. 171802. DOI: `10.1103/PhysRevLett.124.171802`. arXiv: `1910.02014 [hep-ph]`.

[26] Ryusuke Jinno and Masahiro Takimoto. “Probing a classically conformal B-L model with gravitational waves”. In: *Phys. Rev. D* 95.1 (2017), p. 015020. DOI: 10.1103/PhysRevD.95.015020. arXiv: 1604.05035 [hep-ph].

[27] S. W. Hawking, I. G. Moss, and J. M. Stewart. “Bubble Collisions in the Very Early Universe”. In: *Phys. Rev.* D26 (1982), p. 2681. DOI: 10.1103/PhysRevD.26.2681.

[28] Hideo Kodama, Misao Sasaki, and Katsuhiko Sato. “Abundance of Primordial Holes Produced by Cosmological First Order Phase Transition”. In: *Prog. Theor. Phys.* 68 (1982), p. 1979. DOI: 10.1143/PTP.68.1979.

[29] M. Yu. Khlopov, R. V. Konoplich, S. G. Rubin, and A. S. Sakharov. “Formation of Black Holes in First Order Phase Transitions”. In: (July 1998). arXiv: hep-ph/9807343.

[30] Marek Lewicki and Ville Vaskonen. “On bubble collisions in strongly supercooled phase transitions”. In: *Phys. Dark Univ.* 30 (2020), p. 100672. DOI: 10.1016/j.dark.2020.100672. arXiv: 1912.00997 [astro-ph.CO].

[31] Christian Gross, Giacomo Landini, Alessandro Strumia, and Daniele Teresi. “Dark Matter as dark dwarfs and other macroscopic objects: multiverse relics?” In: *JHEP* 09 (2021), p. 033. DOI: 10.1007/JHEP09(2021)033. arXiv: 2105.02840 [hep-ph].

[32] Jing Liu, Ligong Bian, Rong-Gen Cai, Zong-Kuan Guo, and Shao-Jiang Wang. “Primordial Black Hole Production during First-Order Phase Transitions”. In: *Phys. Rev. D* 105.2 (2022), p. L021303. DOI: 10.1103/PhysRevD.105.L021303. arXiv: 2106.05637 [astro-ph.CO].

[33] Tae Hyun Jung and Takemichi Okui. “Primordial Black Holes from Bubble Collisions during a First-Order Phase Transition”. In: (Oct. 2021). arXiv: 2110.04271 [hep-ph].

[34] Katsuya Hashino, Shinya Kanemura, and Tomo Takahashi. “Primordial Black Holes as a Probe of Strongly First-Order Electroweak Phase Transition”. In: (Nov. 2021). arXiv: 2111.13099 [hep-ph].

[35] Katsuya Hashino, Shinya Kanemura, Tomo Takahashi, and Masanori Tanaka. “Probing First-Order Electroweak Phase Transition via Primordial Black Holes in the Effective Field Theory”. In: (Nov. 2022). arXiv: 2211.16225 [hep-ph].

[36] Marek Lewicki, Piotr Toczek, and Ville Vaskonen. “Primordial black holes from strong first-order phase transitions”. In: (May 2023). arXiv: 2305.04924 [astro-ph.CO].

[37] Yann Gouttenoire and Tomer Volansky. “Primordial Black Holes from Supercooled Phase Transitions”. In: (May 2023). arXiv: 2305.04942 [hep-ph].

[38] Y. Aharonov and D. Bohm. “Significance of Electromagnetic Potentials in the Quantum Theory”. In: *Phys. Rev.* 115 (1959). Ed. by J. C. Taylor, pp. 485–491. DOI: 10.1103/PhysRev.115.485.

[39] Holger Bech Nielsen and P. Olesen. “Vortex Line Models for Dual Strings”. In: *Nucl. Phys. B* 61 (1973). Ed. by J. C. Taylor, pp. 45–61. DOI: 10.1016/0550-3213(73)90350-7.

[40] T. W. B. Kibble. “Topology of Cosmic Domains and Strings”. In: *J. Phys. A* 9 (1976), pp. 1387–1398. DOI: 10.1088/0305-4470/9/8/029.

[41] Yann Gouttenoire, Géraldine Servant, and Peera Simakachorn. "Beyond the Standard Models with Cosmic Strings". In: *JCAP* 07 (2020), p. 032. DOI: `10.1088/1475-7516/2020/07/032`. arXiv: `1912.02569 [hep-ph]`.

[42] Yann Gouttenoire, Géraldine Servant, and Peera Simakachorn. "BSM with Cosmic Strings: Heavy, up to EeV mass, Unstable Particles". In: *JCAP* 07 (2020), p. 016. DOI: `10.1088/1475-7516/2020/07/016`. arXiv: `1912.03245 [hep-ph]`.

[43] Craig J. Hogan. "Magnetohydrodynamic Effects of a First-Order Cosmological Phase Transition". In: *Phys. Rev. Lett.* 51 (1983), pp. 1488–1491. DOI: `10.1103/PhysRevLett.51.1488`.

[44] Jean M. Quashnock, Abraham Loeb, and David N. Spergel. "Magnetic Field Generation during the Cosmological QCD Phase Transition". In: *Astrophys. J. Lett.* 344 (1989), pp. L49–L51. DOI: `10.1086/185528`.

[45] T. Vachaspati. "Magnetic Fields from Cosmological Phase Transitions". In: *Phys. Lett. B* 265 (1991), pp. 258–261. DOI: `10.1016/0370-2693(91)90051-Q`.

[46] K. Enqvist and P. Olesen. "On Primordial Magnetic Fields of Electroweak Origin". In: *Phys. Lett. B* 319 (1993), pp. 178–185. DOI: `10.1016/0370-2693(93)90799-N`. arXiv: `hep-ph/9308270`.

[47] Guenter Sigl, Angela V. Olinto, and Karsten Jedamzik. "Primordial Magnetic Fields from Cosmological First Order Phase Transitions". In: *Phys. Rev. D* 55 (1997), pp. 4582–4590. DOI: `10.1103/PhysRevD.55.4582`. arXiv: `astro-ph/9610201`.

[48] Jarkko Ahonen and Kari Enqvist. "Magnetic Field Generation in First Order Phase Transition Bubble Collisions". In: *Phys. Rev. D* 57 (1998), pp. 664–673. DOI: `10.1103/PhysRevD.57.664`. arXiv: `hep-ph/9704334`.

[49] John Ellis, Marek Lewicki, and Ville Vaskonen. "Updated Predictions for Gravitational Waves Produced in a Strongly Supercooled Phase Transition". In: *JCAP* 11 (2020), p. 020. DOI: `10.1088/1475-7516/2020/11/020`. arXiv: `2007.15586 [astro-ph.CO]`.

[50] Adam Falkowski and Jose M. No. "Non-thermal Dark Matter Production from the Electroweak Phase Transition: Multi-TeV WIMPs and 'Baby-Zillas'". In: *JHEP* 02 (2013), p. 034. DOI: `10.1007/JHEP02(2013)034`. arXiv: `1211.5615 [hep-ph]`.

[51] Thomas Hambye, Alessandro Strumia, and Daniele Teresi. "Super-cool Dark Matter". In: *JHEP* 08 (2018), p. 188. DOI: `10.1007/JHEP08(2018)188`. arXiv: `1805.01473 [hep-ph]`.

[52] Iason Baldes and Camilo Garcia-Cely. "Strong gravitational radiation from a simple dark matter model". In: *JHEP* 05 (2019), p. 190. DOI: `10.1007/JHEP05(2019)190`. arXiv: `1809.01198 [hep-ph]`.

[53] Michael J. Baker, Joachim Kopp, and Andrew J. Long. "Filtered Dark Matter at a First Order Phase Transition". In: (Dec. 2019). arXiv: `1912.02830 [hep-ph]`.

[54] Dongjin Chway, Tae Hyun Jung, and Chang Sub Shin. "Dark matter filtering-out effect during a first-order phase transition". In: *Phys. Rev. D* 101.9 (2020), p. 095019. DOI: `10.1103/PhysRevD.101.095019`. arXiv: `1912.04238 [hep-ph]`.

[55] Iason Baldes, Yann Gouttenoire, and Filippo Sala. “String Fragmentation in Supercooled Confinement and Implications for Dark Matter”. In: *JHEP* 04 (2021), p. 278. DOI: 10.1007/JHEP04(2021)278. arXiv: 2007.08440 [hep-ph].

[56] Aleksandr Azatov, Miguel Vanvlasselaer, and Wen Yin. “Dark Matter production from relativistic bubble walls”. In: *JHEP* 03 (2021), p. 288. DOI: 10.1007/JHEP03(2021)288. arXiv: 2101.05721 [hep-ph].

[57] Iason Baldes, Yann Gouttenoire, Filippo Sala, and Géraldine Servant. “Supercool composite Dark Matter beyond 100 TeV”. In: *JHEP* 07 (2022), p. 084. DOI: 10.1007/JHEP07(2022)084. arXiv: 2110.13926 [hep-ph].

[58] Maciej Kierkla, Alexandros Karam, and Bogumila Swiezewska. “Conformal Model for Gravitational Waves and Dark Matter: a Status Update”. In: (Oct. 2022). arXiv: 2210.07075 [astro-ph.CO].

[59] Katherine Freese and Martin Wolfgang Winkler. “Dark matter and gravitational waves from a dark big bang”. In: *Phys. Rev. D* 107.8 (2023), p. 083522. DOI: 10.1103/PhysRevD.107.083522. arXiv: 2302.11579 [astro-ph.CO].

[60] V. A. Kuzmin, V. A. Rubakov, and M. E. Shaposhnikov. “On the Anomalous Electroweak Baryon Number Nonconservation in the Early Universe”. In: *Phys. Lett. B* 155 (1985), p. 36. DOI: 10.1016/0370-2693(85)91028-7.

[61] M. E. Shaposhnikov. “Possible Appearance of the Baryon Asymmetry of the Universe in an Electroweak Theory”. In: *JETP Lett.* 44 (1986), pp. 465–468.

[62] Andrew G. Cohen, David B. Kaplan, and Ann E. Nelson. “Weak Scale Baryogenesis”. In: *Phys. Lett. B* 245 (1990), pp. 561–564. DOI: 10.1016/0370-2693(90)90690-8.

[63] M. E. Shaposhnikov. “Standard Model Solution of the Baryogenesis Problem”. In: *Phys. Lett. B* 277 (1992). [Erratum: Phys.Lett.B 282, 483 (1992)], pp. 324–330. DOI: 10.1016/0370-2693(92)90753-Q.

[64] Glennys R. Farrar and M. E. Shaposhnikov. “Baryon Asymmetry of the Universe in the Minimal Standard Model”. In: *Phys. Rev. Lett.* 70 (1993). [Erratum: Phys.Rev.Lett. 71, 210 (1993)], pp. 2833–2836. DOI: 10.1103/PhysRevLett.70.2833. arXiv: hep-ph/9305274.

[65] Patrick Huet and Eric Sather. “Electroweak Baryogenesis and Standard Model CP Violation”. In: *Phys. Rev. D* 51 (1995), pp. 379–394. DOI: 10.1103/PhysRevD.51.379. arXiv: hep-ph/9404302.

[66] M. B. Gavela, P. Hernandez, J. Orloff, O. Pene, and C. Quimbay. “Standard Model CP Violation and Baryon Asymmetry. Part 2: Finite Temperature”. In: *Nucl. Phys. B* 430 (1994), pp. 382–426. DOI: 10.1016/0550-3213(94)00410-2. arXiv: hep-ph/9406289.

[67] David E. Morrissey and Michael J. Ramsey-Musolf. “Electroweak Baryogenesis”. In: *New J. Phys.* 14 (2012), p. 125003. DOI: 10.1088/1367-2630/14/12/125003. arXiv: 1206.2942 [hep-ph].

[68] Thomas Konstandin. “Quantum Transport and Electroweak Baryogenesis”. In: *Phys. Usp.* 56 (2013), pp. 747–771. DOI: `10.3367/UFNe.0183.201308a.0785`. arXiv: `1302.6713 [hep-ph]`.

[69] Géraldine Servant. “The serendipity of electroweak baryogenesis”. In: *Phil. Trans. Roy. Soc. Lond. A* 376.2114 (2018), p. 20170124. DOI: `10.1098/rsta.2017.0124`. arXiv: `1807.11507 [hep-ph]`.

[70] Andrey Katz and Antonio Riotto. “Baryogenesis and Gravitational Waves from Runaway Bubble Collisions”. In: *JCAP* 1611.11 (2016), p. 011. DOI: `10.1088/1475-7516/2016/11/011`. arXiv: `1608.00583 [hep-ph]`.

[71] Aleksandr Azatov, Miguel Vanvlasselaer, and Wen Yin. “Baryogenesis via Relativistic Bubble Walls”. In: *JHEP* 10 (2021), p. 043. DOI: `10.1007/JHEP10(2021)043`. arXiv: `2106.14913 [hep-ph]`.

[72] Iason Baldes, Simone Blasi, Alberto Mariotti, Alexander Sevrin, and Kevin Turbang. “Baryogenesis via relativistic bubble expansion”. In: *Phys. Rev. D* 104.11 (2021), p. 115029. DOI: `10.1103/PhysRevD.104.115029`. arXiv: `2106.15602 [hep-ph]`.

[73] Edward Witten. “Cosmic Separation of Phases”. In: *Phys. Rev.* D30 (1984), pp. 272–285. DOI: `10.1103/PhysRevD.30.272`.

[74] Arthur Kosowsky, Michael S. Turner, and Richard Watkins. “Gravitational Waves from First Order Cosmological Phase Transitions”. In: *Phys. Rev. Lett.* 69 (1992), pp. 2026–2029. DOI: `10.1103/PhysRevLett.69.2026`.

[75] Marc Kamionkowski, Arthur Kosowsky, and Michael S. Turner. “Gravitational radiation from first order phase transitions”. In: *Phys. Rev.* D49 (1994), pp. 2837–2851. DOI: `10.1103/PhysRevD.49.2837`. arXiv: `astro-ph/9310044 [astro-ph]`.

[76] Lisa Randall and Geraldine Servant. “Gravitational waves from warped spacetime”. In: *JHEP* 05 (2007), p. 054. DOI: `10.1088/1126-6708/2007/05/054`. arXiv: `hep-ph/0607158 [hep-ph]`.

[77] Stephan J. Huber and Thomas Konstandin. “Gravitational Wave Production by Collisions: More Bubbles”. In: *JCAP* 0809 (2008), p. 022. DOI: `10.1088/1475-7516/2008/09/022`. arXiv: `0806.1828 [hep-ph]`.

[78] Mark Hindmarsh, Stephan J. Huber, Kari Rummukainen, and David J. Weir. “Gravitational waves from the sound of a first order phase transition”. In: *Phys. Rev. Lett.* 112 (2014), p. 041301. DOI: `10.1103/PhysRevLett.112.041301`. arXiv: `1304.2433 [hep-ph]`.

[79] Ryusuke Jinno and Masahiro Takimoto. “Gravitational waves from bubble dynamics: Beyond the Envelope”. In: *JCAP* 1901 (2019), p. 060. DOI: `10.1088/1475-7516/2019/01/060`. arXiv: `1707.03111 [hep-ph]`.

[80] Thomas Konstandin. “Gravitational radiation from a bulk flow model”. In: *JCAP* 1803.03 (2018), p. 047. DOI: `10.1088/1475-7516/2018/03/047`. arXiv: `1712.06869 [astro-ph.CO]`.

[81] Daniel Cutting, Mark Hindmarsh, and David J. Weir. “Gravitational waves from vacuum first-order phase transitions: from the envelope to the lattice”. In: *Phys. Rev.* D97.12 (2018), p. 123513. DOI: `10.1103/PhysRevD.97.123513`. arXiv: `1802.05712 [astro-ph.CO]`.

[82] Marek Lewicki and Ville Vaskonen. “Gravitational wave spectra from strongly supercooled phase transitions”. In: (July 2020). arXiv: `2007.04967 [astro-ph.CO]`.

[83] Mark B. Hindmarsh, Marvin Lüben, Johannes Lumma, and Martin Pauly. “Phase transitions in the early universe”. In: *SciPost Phys. Lect. Notes* 24 (2021), p. 1. DOI: `10.21468/SciPostPhysLectNotes.24`. arXiv: `2008.09136 [astro-ph.CO]`.

[84] Yann Gouttenoire. “Beyond the Standard Model Cocktail”. In: (July 2022). arXiv: `2207.01633 [hep-ph]`.

[85] Walter D. Goldberger, Benjamí n Grinstein, and Witold Skiba. “Distinguishing the Higgs Boson from the Dilaton at the Large Hadron Collider”. In: *Physical Review Letters* 100.11 (2008). DOI: `10.1103/physrevlett.100.111802`. URL: `https://doi.org/10.1103%2Fphysrevlett.100.111802`.

[86] Sebastian Bruggisser, Benedict von Harling, Oleksii Matsedonskyi, and Geraldine Servant. *Electroweak Phase Transition and Baryogenesis in Composite Higgs Models*. 2018. arXiv: `1804.07314 [hep-ph]`.

[87] Sidney R. Coleman. “The Fate of the False Vacuum. 1. Semiclassical Theory”. In: *Phys. Rev. D* 15 (1977). [Erratum: Phys.Rev.D 16, 1248 (1977)], pp. 2929–2936. DOI: `10.1103/PhysRevD.16.1248`.

[88] Curtis G. Callan Jr. and Sidney R. Coleman. “The Fate of the False Vacuum. 2. First Quantum Corrections”. In: *Phys. Rev. D* 16 (1977), pp. 1762–1768. DOI: `10.1103/PhysRevD.16.1762`.

[89] Yann Gouttenoire, Ryusuke Jinno, and Filippo Sala. “Friction pressure on relativistic bubble walls”. In: *JHEP* 05 (2022), p. 004. DOI: `10.1007/JHEP05(2022)004`. arXiv: `2112.07686 [hep-ph]`.

[90] K. Enqvist, J. Ignatius, K. Kajantie, and K. Rummukainen. “Nucleation and bubble growth in a first order cosmological electroweak phase transition”. In: *Phys. Rev.* D45 (1992), pp. 3415–3428. DOI: `10.1103/PhysRevD.45.3415`.

[91] Thomas Konstandin and Jose M. No. “Hydrodynamic obstruction to bubble expansion”. In: *JCAP* 02 (2011), p. 008. DOI: `10.1088/1475-7516/2011/02/008`. arXiv: `1011.3735 [hep-ph]`.

[92] James M. Cline et al. “Baryogenesis and gravity waves from a UV-completed electroweak phase transition”. In: *Phys. Rev. D* 103.12 (2021), p. 123529. DOI: `10.1103/PhysRevD.103.123529`. arXiv: `2102.12490 [hep-ph]`.

[93] Benoit Laurent and James M. Cline. “First principles determination of bubble wall velocity”. In: *Phys. Rev. D* 106.2 (2022), p. 023501. DOI: `10.1103/PhysRevD.106.023501`. arXiv: `2204.13120 [hep-ph]`.

[94] Stefania De Curtis, Luigi Delle Rose, Andrea Guiggiani, Ángel Gil Muyor, and Giuliano Panico. “Collision integrals for cosmological phase transitions”. In: *JHEP* 05 (2023), p. 194. DOI: `10.1007/JHEP05(2023)194`. arXiv: `2303.05846 [hep-ph]`.

[95] Dietrich Bodeker and Guy D. Moore. “Can electroweak bubble walls run away?” In: *JCAP* 05 (2009), p. 009. DOI: 10.1088/1475-7516/2009/05/009. arXiv: 0903.4099 [hep-ph].

[96] Aleksandr Azatov and Miguel Vanvlasselaer. “Bubble wall velocity: heavy physics effects”. In: *JCAP* 01 (2021), p. 058. DOI: 10.1088/1475-7516/2021/01/058. arXiv: 2010.02590 [hep-ph].

[97] Dietrich Bodeker and Guy D. Moore. “Electroweak Bubble Wall Speed Limit”. In: *JCAP* 05 (2017), p. 025. DOI: 10.1088/1475-7516/2017/05/025. arXiv: 1703.08215 [hep-ph].

[98] Isabel Garcia Garcia, Giacomo Koszegi, and Rudin Petrossian-Byrne. “Reflections on Bubble Walls”. In: (Dec. 2022). arXiv: 2212.10572 [hep-ph].

[99] Iason Baldes, Yann Gouttenoire, and Filippo Sala. “Hot and heavy dark matter from a weak scale phase transition”. In: *SciPost Phys.* 14 (2023), p. 033. DOI: 10.21468/SciPostPhys.14.3.033. arXiv: 2207.05096 [hep-ph].

[100] Yann Gouttenoire and et al. “Wall decay during first-order phase transition”. In: *In progress* ().

[101] Ryusuke Jinno, Bibhushan Shakya, and Jorinde van de Vis. “Gravitational Waves from Feebly Interacting Particles in a First Order Phase Transition”. In: (Nov. 2022). arXiv: 2211.06405 [gr-qc].

[102] Aleksandr Azatov, Giulio Barni, Sabyasachi Chakraborty, Miguel Vanvlasselaer, and Wen Yin. “Ultra-relativistic bubbles from the simplest Higgs portal and their cosmological consequences”. In: *JHEP* 10 (2022), p. 017. DOI: 10.1007/JHEP10(2022)017. arXiv: 2207.02230 [hep-ph].

[103] Marek Lewicki and Ville Vaskonen. “Gravitational waves from colliding vacuum bubbles in gauge theories”. In: *Eur. Phys. J. C* 81.5 (2021). [Erratum: Eur.Phys.J.C 81, 1077 (2021)], p. 437. DOI: 10.1140/epjc/s10052-021-09232-3. arXiv: 2012.07826 [astro-ph.CO].

[104] Daniel Cutting, Elba Granados Escartin, Mark Hindmarsh, and David J. Weir. “Gravitational waves from vacuum first order phase transitions II: from thin to thick walls”. In: (May 2020). arXiv: 2005.13537 [astro-ph.CO].

[105] Ryusuke Jinno, Hyeonseok Seong, Masahiro Takimoto, and Choong Min Um. “Gravitational waves from first-order phase transitions: Ultra-supercooled transitions and the fate of relativistic shocks”. In: *JCAP* 10 (2019), p. 033. DOI: 10.1088/1475-7516/2019/10/033. arXiv: 1905.00899 [astro-ph.CO].

[106] Ruth Durrer and Chiara Caprini. “Primordial Magnetic Fields and Causality”. In: *JCAP* 11 (2003), p. 010. DOI: 10.1088/1475-7516/2003/11/010. arXiv: astro-ph/0305059.

[107] Chiara Caprini, Ruth Durrer, Thomas Konstandin, and Geraldine Servant. “General Properties of the Gravitational Wave Spectrum from Phase Transitions”. In: *Phys. Rev.* D79 (2009), p. 083519. DOI: 10.1103/PhysRevD.79.083519. arXiv: 0901.1661 [astro-ph.CO].

[108] Rong-Gen Cai, Shi Pi, and Misao Sasaki. "Universal Infrared Scaling of Gravitational Wave Background Spectra". In: *Phys. Rev. D* 102.8 (2020), p. 083528. DOI: `10.1103/PhysRevD.102.083528`. arXiv: `1909.13728 [astro-ph.CO]`.

[109] Anson Hook, Gustavo Marques-Tavares, and Davide Racco. "Causal Gravitational Waves as a Probe of Free Streaming Particles and the Expansion of the Universe". In: *JHEP* 02 (2021), p. 117. DOI: `10.1007/JHEP02(2021)117`. arXiv: `2010.03568 [hep-ph]`.

[110] Eric Thrane and Joseph D. Romano. "Sensitivity curves for searches for gravitational-wave backgrounds". In: *Phys. Rev.* D 88.12 (2013), p. 124032. DOI: `10.1103/PhysRevD.88.124032`. arXiv: `1310.5300 [astro-ph.IM]`.

[111] S. Hild et al. "Sensitivity Studies for Third-Generation Gravitational Wave Observatories". In: *Class. Quant. Grav.* 28 (2011), p. 094013. DOI: `10.1088/0264-9381/28/9/094013`. arXiv: `1012.0908 [gr-qc]`.

[112] Chiara Caprini et al. "Reconstructing the spectral shape of a stochastic gravitational wave background with LISA". In: (2019). arXiv: `1906.09244 [astro-ph.CO]`.

[113] H.Arthur Weldon. "Structure of the Gluon Propagator at Finite Temperature". In: *Annals of Physics* 271.1 (1999), pp. 141–156. DOI: `10.1006/aphy.1998.5873`. URL: `https://doi.org/10.1006%2Faphy.1998.5873`.

[114] A. K. Rebhan. "Non-Abelian Debye mass at next-to-leading order". In: *Physical Review D* 48.9 (1993), R3967–R3970. DOI: `10.1103/physrevd.48.r3967`. URL: `https://doi.org/10.1103%2Fphysrevd.48.r3967`.

[115] Tyler Gorda et al. "Soft photon propagation in a hot and dense medium to next-to-leading order". In: *Physical Review D* 107.3 (2023). DOI: `10.1103/physrevd.107.036012`. URL: `https://doi.org/10.1103%2Fphysrevd.107.036012`.

[116] Eric Braaten and Robert D. Pisarski. "Soft Amplitudes in Hot Gauge Theories: A General Analysis". In: *Nucl. Phys. B* 337 (1990), pp. 569–634. DOI: `10.1016/0550-3213(90)90508-B`.

[117] Adam Alloul, Neil D. Christensen, Céline Degrande, Claude Duhr, and Benjamin Fuks. "FeynRules 2.0 — A complete toolbox for tree-level phenomenology". In: *Computer Physics Communications* 185.8 (2014), pp. 2250–2300. DOI: `10.1016/j.cpc.2014.04.012`. URL: `https://doi.org/10.1016%2Fj.cpc.2014.04.012`.

[118] Thomas Hahn. "Generating Feynman diagrams and amplitudes with FeynArts 3". In: *Computer Physics Communications* 140.3 (2001), pp. 418–431. DOI: `10.1016/s0010-4655(01)00290-9`. URL: `https://doi.org/10.1016%2Fs0010-4655%2801%2900290-9`.

[119] Vladyslav Shtabovenko, Rolf Mertig, and Frederik Orellana. "FeynCalc 9.3: New features and improvements". In: *Computer Physics Communications* 256 (2020), p. 107478. DOI: `10.1016/j.cpc.2020.107478`. URL: `https://doi.org/10.1016%2Fj.cpc.2020.107478`.

[120] Vladyslav Shtabovenko, Rolf Mertig, and Frederik Orellana. "New developments in FeynCalc 9.0". In: *Computer Physics Communications* 207 (2016), pp. 432–444. DOI: `10.1016/j.cpc.2016.06.008`. URL: `https://doi.org/10.1016%2Fj.cpc.2016.06.008`.

[121] R. Mertig, M. Bohm, and Ansgar Denner. “FEYN CALC: Computer algebraic calculation of Feynman amplitudes”. In: *Comput. Phys. Commun.* 64 (1991), pp. 345–359. DOI: 10.1016/0010-4655(91)90130-D.

[122] Nima Arkani-Hamed and Juan Maldacena. “Cosmological Collider Physics”. In: (Mar. 2015). arXiv: 1503.08043 [hep-th].

[123] Y. Akrami et al. “Planck 2018 results. X. Constraints on inflation”. In: *Astron. Astrophys.* 641 (2020), A10. DOI: 10.1051/0004-6361/201833887. arXiv: 1807.06211 [astro-ph.CO].

[124] Iason Baldes, Maximilian Dichtl, Yann Gouttenoire, and Filippo Sala. “(To Appear)”. In: (). arXiv: 23mm.nnnnn.

[125] N. Aghanim et al. “Planck 2018 results. VI. Cosmological parameters”. In: *Astron. Astrophys.* 641 (2020). [Erratum: Astron.Astrophys. 652, C4 (2021)], A6. DOI: 10.1051/0004-6361/201833910. arXiv: 1807.06209 [astro-ph.CO].

[126] Zaven Arzoumanian et al. “Searching for Gravitational Waves from Cosmological Phase Transitions with the NANOGrav 12.5-Year Dataset”. In: *Phys. Rev. Lett.* 127.25 (2021), p. 251302. DOI: 10.1103/PhysRevLett.127.251302. arXiv: 2104.13930 [astro-ph.CO].

[127] Torsten Bringmann, Paul Frederik Depta, Thomas Konstandin, Kai Schmidt-Hoberg, and Carlo Tasillo. “Does NANOGrav observe a dark sector phase transition?” In: (June 2023). arXiv: 2306.09411 [astro-ph.CO].

[128] R. Abbott et al. “Upper limits on the isotropic gravitational-wave background from Advanced LIGO and Advanced Virgo’s third observing run”. In: *Phys. Rev. D* 104.2 (2021), p. 022004. DOI: 10.1103/PhysRevD.104.022004. arXiv: 2101.12130 [gr-qc].

[129] L. Lentati et al. “European Pulsar Timing Array Limits On An Isotropic Stochastic Gravitational-Wave Background”. In: *Mon. Not. Roy. Astron. Soc.* 453.3 (2015), pp. 2576–2598. DOI: 10.1093/mnras/stv1538. arXiv: 1504.03692 [astro-ph.CO].

[130] Z. Arzoumanian et al. “The NANOGrav 11-year Data Set: Pulsar-timing Constraints On The Stochastic Gravitational-wave Background”. In: *Astrophys. J.* 859.1 (2018), p. 47. DOI: 10.3847/1538-4357/aabd3b. arXiv: 1801.02617 [astro-ph.HE].

[131] Heather Audley et al. “Laser Interferometer Space Antenna”. In: (2017). arXiv: 1702.00786 [astro-ph.IM].

[132] Kent Yagi and Naoki Seto. “Detector Configuration of Decigo/Bbo and Identification of Cosmological Neutron-Star Binaries”. In: *Phys. Rev. D* 83 (2011). [Erratum: Phys.Rev.D 95, 109901 (2017)], p. 044011. DOI: 10.1103/PhysRevD.83.044011. arXiv: 1101.3940 [astro-ph.CO].

[133] M. Punturo et al. “The Einstein Telescope: A third-generation gravitational wave observatory”. In: *Class. Quant. Grav.* 27 (2010), p. 194002. DOI: 10.1088/0264-9381/27/19/194002.

[134] B. P. Abbott et al. “Prospects for observing and localizing gravitational-wave transients with Advanced LIGO, Advanced Virgo and KAGRA”. In: *Living Rev. Rel.* 21.1 (2018), p. 3. DOI: `10.1007/s41114-020-00026-9`. arXiv: `1304.0670 [gr-qc]`.

[135] Gemma Janssen et al. “Gravitational wave astronomy with the SKA”. In: *PoS* AASKA14 (2015). Ed. by Tyler L. Bourke et al., p. 037. DOI: `10.22323/1.215.0037`. arXiv: `1501.00127 [astro-ph.IM]`.

[136] Pablo A. Rosado. “Gravitational wave background from binary systems”. In: *Phys. Rev.* D 84 (2011), p. 084004. DOI: `10.1103/PhysRevD.84.084004`. arXiv: `1106.5795 [gr-qc]`.

[137] Astrid Lamberts et al. “Predicting the Lisa White Dwarf Binary Population in the Milky Way with Cosmological Simulations”. In: *Mon. Not. Roy. Astron. Soc.* 490.4 (2019), pp. 5888–5903. DOI: `10.1093/mnras/stz2834`. arXiv: `1907.00014 [astro-ph.HE]`.

[138] Guillaume Boileau, Alexander C. Jenkins, Mairi Sakellariadou, Renate Meyer, and Nelson Christensen. “Ability of Lisa to Detect a Gravitational-Wave Background of Cosmological Origin: the Cosmic String Case”. In: *Phys. Rev. D* 105.2 (2022), p. 023510. DOI: `10.1103/PhysRevD.105.023510`. arXiv: `2109.06552 [gr-qc]`.

[139] Guillaume Boileau, Nelson Christensen, Chloe Gowling, Mark Hindmarsh, and Renate Meyer. “Prospects for LISA to detect a gravitational-wave background from first order phase transitions”. In: *JCAP* 02 (2023), p. 056. DOI: `10.1088/1475-7516/2023/02/056`. arXiv: `2209.13277 [gr-qc]`.

[140] Travis Robson, Neil J. Cornish, and Chang Liu. “The Construction and Use of Lisa Sensitivity Curves”. In: *Class. Quant. Grav.* 36.10 (2019), p. 105011. DOI: `10.1088/1361-6382/ab1101`. arXiv: `1803.01944 [astro-ph.HE]`.

[141] Djuna Croon. “TASI lectures on Phase Transitions, Baryogenesis, and Gravitational Waves”. In: (June 2023). arXiv: `2307.00068 [hep-ph]`.

[142] Brian D. Fields, Keith A. Olive, Tsung-Han Yeh, and Charles Young. “Big-Bang Nucleosynthesis after Planck”. In: *JCAP* 03 (2020). [Erratum: JCAP 11, E02 (2020)], p. 010. DOI: `10.1088/1475-7516/2020/03/010`. arXiv: `1912.01132 [astro-ph.CO]`.

[143] A. D. Sakharov. “Violation of CP Invariance, C asymmetry, and baryon asymmetry of the universe”. In: *Pisma Zh. Eksp. Teor. Fiz.* 5 (1967), pp. 32–35. DOI: `10.1070/PU1991v034n05ABEH002497`.

[144] Csaba Balazs. “Baryogenesis: A small review of the big picture”. In: (Nov. 2014). arXiv: `1411.3398 [hep-ph]`.

[145] C. Jarlskog. “A Basis Independent Formulation of the Connection Between Quark Mass Matrices, CP Violation and Experiment”. In: *Z. Phys. C* 29 (1985), pp. 491–497. DOI: `10.1007/BF01565198`.

[146] Jihn E. Kim, Se-Jin Kim, Soonkeon Nam, and Myungbo Shim. “Jarlskog determinant and data on flavor matrices”. In: *Mod. Phys. Lett. A* 35.31 (2020), p. 2050261. DOI: `10.1142/S0217732320502612`. arXiv: `1907.12247 [hep-ph]`.

[147] M. B. Gavela, P. Hernandez, J. Orloff, and O. Pene. "Standard model CP violation and baryon asymmetry". In: *Mod. Phys. Lett. A* 9 (1994), pp. 795–810. DOI: `10.1142/S0217732394000629`. arXiv: `hep-ph/9312215`.

[148] R. E. Cutkosky. "Some Applications of the Generalized Unitarity Relation". In: *Phys. Rev. Lett.* 4 (12 1960), pp. 624–626. DOI: `10.1103/PhysRevLett.4.624`. URL: `https://link.aps.org/doi/10.1103/PhysRevLett.4.624`.

[149] S. Schael et al. "Precision electroweak measurements on the Z resonance". In: *Phys. Rept.* 427 (2006), pp. 257–454. DOI: `10.1016/j.physrep.2005.12.006`. arXiv: `hep-ex/0509008`.

[150] A. Heister et al. "Search for supersymmetric particles with R parity violating decays in e^+e^- collisions at $\sqrt{s}$ up to 209-GeV". In: *Eur. Phys. J. C* 31 (2003), pp. 1–16. DOI: `10.1140/epjc/s2003-01311-5`. arXiv: `hep-ex/0210014`.

[151] T. Aaltonen et al. "Search for Pair Production of Strongly Interacting Particles Decaying to Pairs of Jets in $p\bar{p}$ Collisions at $\sqrt{s} = 1.96$ TeV". In: *Phys. Rev. Lett.* 111.3 (2013), p. 031802. DOI: `10.1103/PhysRevLett.111.031802`. arXiv: `1303.2699 [hep-ex]`.

[152] Morad Aaboud et al. "A search for pair-produced resonances in four-jet final states at $\sqrt{s} = 13$ TeV with the ATLAS detector". In: *Eur. Phys. J. C* 78.3 (2018), p. 250. DOI: `10.1140/epjc/s10052-018-5693-4`. arXiv: `1710.07171 [hep-ex]`.

[153] "Search for resonant and nonresonant production of pairs of dijet resonances in proton-proton collisions at $\sqrt{s} = 13$ TeV". In: (June 2022). arXiv: `2206.09997 [hep-ex]`.

[154] C. Abel et al. "Measurement of the Permanent Electric Dipole Moment of the Neutron". In: *Phys. Rev. Lett.* 124.8 (2020), p. 081803. DOI: `10.1103/PhysRevLett.124.081803`. arXiv: `2001.11966 [hep-ex]`.

[155] Wafia Bensalem and Daniel Stolarski. "Flavor and CP violation from a QCD-like hidden sector". In: *JHEP* 02 (2022), p. 011. DOI: `10.1007/JHEP02(2022)011`. arXiv: `2111.05515 [hep-ph]`.

[156] Stephen M. Barr and A. Zee. "Electric Dipole Moment of the Electron and of the Neutron". In: *Phys. Rev. Lett.* 65 (1990). [Erratum: Phys.Rev.Lett. 65, 2920 (1990)], pp. 21–24. DOI: `10.1103/PhysRevLett.65.21`.

[157] Gian Francesco Giudice, Ben Gripaios, and Raman Sundrum. "Flavourful Production at Hadron Colliders". In: *JHEP* 08 (2011), p. 055. DOI: `10.1007/JHEP08(2011)055`. arXiv: `1105.3161 [hep-ph]`.

[158] Marcella Bona et al. "Unitarity Triangle global fits beyond the Standard Model: UTfit 2021 NP update". In: *PoS* EPS-HEP2021 (2022), p. 500. DOI: `10.22323/1.398.0500`.

[159] Alison J. Farmer and E. Sterl Phinney. "The gravitational wave background from cosmological compact binaries". In: *Mon. Not. Roy. Astron. Soc.* 346 (2003), p. 1197. DOI: `10.1111/j.1365-2966.2003.07176.x`. arXiv: `astro-ph/0304393 [astro-ph]`.